# Spatially-Resolved Dynamics of Charge-Density Waves in Niobium Triselenide

and

# X-Ray Fluorescence Imaging of Archaeological Artifacts

A Dissertation

Presented to the Faculty of the Graduate School

of Cornell University

in Partial Fulfillment of the Requirements for the Degree of

Doctor of Philosophy

by

Ethan C. Geil

August 2014

**Abstract**

Spatially-Resolved Dynamics of Charge-Density Waves in Niobium Triselenide

and

X-Ray Fluorescence Imaging of Archaeological Artifacts

Ethan C. Geil

Cornell University 2014

The first volume of this dissertation presents experimental measurements of the charge-density wave (CDW) system in niobium triselenide ($NbSe_3$). Novel measurement techniques, allowing unprecedented spatially- and temporally- resolved observations of CDW dynamics, are reported. Both transient and steady-state measurements are described and analyzed. These results illustrate the crucial role of plasticity in CDW dynamics.

Volume II reports on synchrotron-based X-ray fluorescence (XRF) imaging of archaeological artifacts. Two-dimensional fluorescence images reveal a wealth of information about these objects, including their compositions, trace element concentrations, and features which have been obscured by aging processes. Techniques for effectively and efficiently recording and analyzing fluorescence data are developed, and results are presented for several types of artifacts.

## Biographical Sketch

Ethan Geil received his Bachelor of Science in physics in 2006 from the California Institute of Technology.

## Acknowledgements

This work was conducted in part at the Cornell High Energy Synchrotron Source, which is supported by the NSF and NIH/NIGMS via NSF award DMR-1332208.

This work was conducted in part at the Cornell NanoScale Facility, a member of the National Nanotechnology Infrastructure Network, which is supported by the National Science Foundation (Grant ECCS-0335765).

This work was conducted in part at the Cornell Center for Materials Research, which is supported by the NSF via grant DMR-1120296, part of the NSF MRSEC Program.

Charge-density-wave research was supported by NSF grant DMR-0805240.

X-ray fluorescence work was supported in part by grants from the Samuel H. Kress foundation and the Mellon foundation.

# Volume I

Spatially-Resolved Dynamics of Charge-Density Waves in Niobium Triselenide

# Contents

# List of Figures

# Chapter 1

# Introduction to Charge-Density Waves in $NbSe_3$

## 1.1 Charge-Density Waves

At low temperatures, certain highly anisotropic conductors undergo a phase transition to a charge-density-wave (CDW) ground state, in which the spatial variation of the charge density is given by

$$n_c = n_0 + \delta n \sin(\mathbf{Q} \cdot \mathbf{r} + \phi), \tag{1.1}$$

where $\mathbf{Q}$ is the CDW wave vector, $\delta n$ is the CDW amplitude, and $\phi = \phi(\mathbf{r}, t)$ is the phase with respect to the atomic lattice. CDW systems exhibit a remarkable array of complex dynamical behaviors. This section introduces the basic notions of CDW physics; for comprehensive reviews, see Refs. [33, 37, 38, 66].

Rudolph Peierls first proposed a mechanism for the CDW transition [82]: In a one-dimensional metal, a periodic modulation of the lattice spacing (and correspondingly of the carrier density) with a wavelength $\lambda = \pi/k_F$ (where $k_F$ is the Fermi wavevector) opens a gap of width $2\Delta$ in the conduction band at the Fermi surface (Fig. 1.1). If the electronic energy

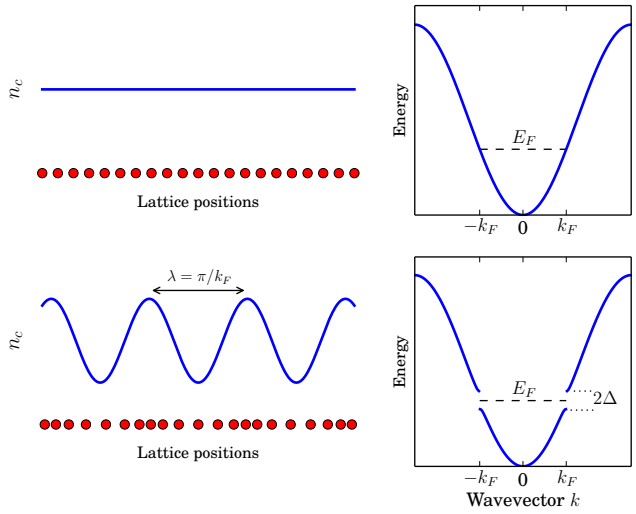


Figure 1.1: Peierls transition. A periodic distortion of the lattice with wavelength $\lambda = \pi/k_F$, accompanied by a corresponding modulation of the electron density, opens an energy gap of width $2\Delta$ at the Fermi surface.

gained by the formation of the gap outweighs the elastic energy of the lattice distortion, the transition is energetically favorable. At high temperatures, thermal excitation of electrons across the gap reduces the electronic energy gain, leading to a second-order phase transition to a metallic state. The mean-field theory is formally analagous to the BCS theory of superconductivity, which predicts a transition temperature of $2\Delta = 3.52T_{\mathrm{MF}}$ [37].

Fluctuations destroy the long-range CDW order for $T > 0$ in a strictly one-dimensional CDW system, so interactions in the transverse dimension are necessary for the existence of finite-temperature CDWs [38]. Real CDW conductors are, of course, three-dimensional, but are typically highly anisotropic (quasi-one- or two-dimensional), comprising loosely-coupled bundles of linear molecular chains, each of which carries a CDW. CDWs have been found in numerous materials (see Ref. [66] for a comprehensive list), but the present work is restricted to $NbSe_3$, whose properties are summarized later in this chapter.

If the wavelength of the CDW is incommensurate with the lattice spacing (as in $NbSe_3$), then in a perfect lattice, there is no preferred position of the phase $\phi$ with respect to the lattice, and it might be expected that the CDW should slide freely, carrying with it a

collective current. In fact, Fröhlich [27] proposed this as a mechanism for superconductivity. However, real CDW conductors contain impurities and other defects which pin the CDW to the lattice. In the ground state, the CDW adjusts its local phase to minimize its energy, e.g. by aligning a maximum of the electron density with a positive impurity. Sufficiently large electric fields can "depin" the CDW, but even in this case, interactions with normal carriers and phonons damp the motion.

The most widely used model of both CDW dynamics and static correlations is due to Fukuyama, Lee, and Rice (FLR) [28, 29, 44, 45]. It expresses the time evolution of the CDW phase $\phi(\mathbf{r}, t)$ in terms of elastic strain and interactions with impurities:

$$\gamma \frac{\partial \phi}{\partial t} = \mathbf{K} \cdot \frac{\partial^2 \phi}{\partial \mathbf{r}^2} + \left( \frac{e n_c}{Q} \right) E + n_1 \sum_{i=1}^{N_{\mathrm{imp}}} \delta(\mathbf{r} - \mathbf{r}_i) \sin(\mathbf{Q} \cdot \mathbf{r} + \phi) \tag{1.2}$$

where $\gamma$ is a damping constant, $\mathbf{K} = (K_x, K_y, K_z)$ are the elastic constants, $e$ is the elementary charge, $n_c$ is the condensate number density, $E$ is the external electric field in the $z$ direction (the direction along which the CDW can slide), and the last term accounts for interactions with impurities at randomly distributed positions $\mathbf{r}_i$. The ground state is determined by a competition between the elastic energy and the impurity interaction energy. FLR describe two limiting cases: If the impurity potential is large (strong pinning), the CDW matches its phase to each impurity. In the case of weak pinning, on the other hand, the CDW phase varies smoothy over volumes containing many impurities, resulting in phase-coherent domains with a characteristic length of $L_0 = ([(3V_0 e \delta n/(\pi v_F)]^2 n_i)^{-1/3}$, where $V_0$ is the potential of a single impurity, $n_i$ is the impurity concentration, $\delta n$ is the CDW amplitude, and $v_F$ is the Fermi velocity.

Electric fields larger than a threshold field $E_T$ overcome the pinning and cause the CDW to slide, carrying with it an electric current $I_c = (e n_c/Q)(\delta\phi/\delta t)$. (Reference is often made to an equivalent threshold *current*, given by $I_T = A E_T \sigma_n$, where $A$ is the cross-sectional area and $\sigma_n$ is the conductivity due to the normal, uncondensed carriers). In a typical experimen-

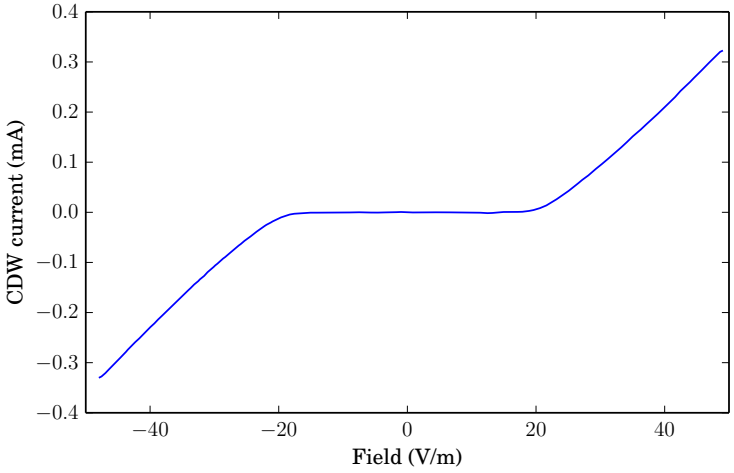


Figure 1.2: $I_c{-}V$ curve of a typical $NbSe_3$, sample. Below a threshold field of $E_T \approx 16.4\,\mathrm{V/m}$, the CDW remains pinned, and there is no collective current. Above the threshold, the CDW conductivity increases, approaching an Ohmic asymptote for high fields. The CDW current was determined by subtracting the normal current from the total current. $T = 80\,\mathrm{K}$.

tal configuration, contacts are applied near the ends of a crystal of a CDW conductor, and a voltage is applied across the contacts. The resulting current is measured (or vice-versa). Figure 1.2 shows the current-voltage $(I - V)$ characteristic of one such sample.

The simple FLR model successfully accounts many experimental properties of CDW behavior, and has been the basis of most subsequent theoretical work. Its most obvious shortcoming is that it neglects amplitude variations of the CDW. Thus, the FLR model is strictly *elastic*. However, for a CDW current to flow at all in a sample contacted by metallic leads (the typical configuration), normal carriers must be converted to condensed carriers (and vice-versa) at the contacts. Since the number of electrons per wavelength is fixed, this can take place only through the creation or annihilation of CDW wavelengths, a process termed *phase slip*. The energy barrier to simultaneously eliminating a wavefront across the entire cross-section is prohibitively high; instead, phase slip is thought to proceed via the nucleation and growth of dislocation loops [14].

In addition to slipping longitudinally, the CDW can also *shear* plastically: under sufficient stress, the phase of a chain or group of chains can advance by $2\pi$ with respect to its neighbors [40]. Plasticity is not confined to the region near the current contacts. Even in high-quality

Figure 1.3: Photograph of $NbSe_3$ crystals, which grow as long, thin ribbons

crystals, phase slip and shear can occur throughout the sample, and this is responsible for many interesting phenomena. The present work emphasizes the crucial role of plasticity in CDW dynamics.

## 1.2 $NbSe_3$ Structure and Properties

Synthesis of $NbSe_3$ (Fig. 1.3) was by first reported by Meerschaut and Rouxel in 1975 [59]. It was soon noticed that the resistivity-temperature characteristic exhibits two pronounced anomalies at $T_{p_1} \approx 145\,\mathrm{K}$ and $T_{p_2} \approx 59\,\mathrm{K}$ (Fig. 1.4), which are suppressed by sufficiently large electric fields. Monceau et al. [67] ascribed this behavior to the formation of two independent charge-density waves.

Nearly forty years later, $NbSe_3$ remains a model material for the study of CDW dynamics. Extremely high purity and nearly defect-free crystals can be obtained; it is relatively inert; it readily forms low-resistance electrical contacts; and the CDW depins easily [108]. These characteristics facilitate the transport measurements which are necessary for an experimental understanding of the dynamics of the condensate.

The following chart summarizes several important properties of $NbSe_3$.

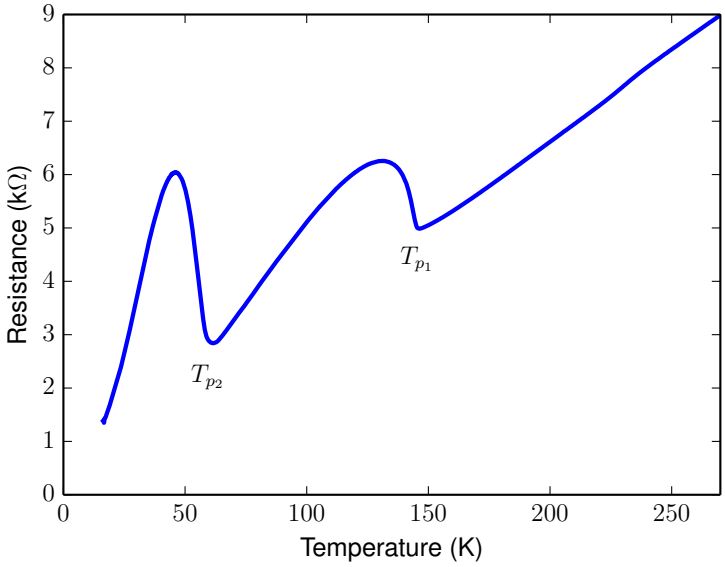


Figure 1.4: The low-field resistance vs. temperature of a $NbSe_3$ sample shows two large anomalies at 145 K and 59 K. The crystal cross-sectional area and length were 0.17 µm$^2$ and 730 µm.

- **Lattice parameters** (monoclinic lattice) [39]

  $a = 10.009\,\text{Å}$

  $b = 3.4805\,\text{Å}$

  $c = 15.629\,\text{Å}$

  $\beta = 109.47°$

- **CDW wave vectors** and in-chain wavelengths [26]

  $\mathbf{q_1} = 0.243b^* = (0, 0.698, 0)\,\text{nm}^{-1}$

  $\lambda_1 = 1.43\,\text{nm}$

  $\mathbf{q_2} = 0.5\mathbf{a}^* + 0.263\mathbf{b}^* + 0.5\mathbf{c}^* = (0.5, 0.76, 0.32)\,\text{nm}^{-1}$

  $\lambda_2 = 1.32\,\text{nm}$

- **CDW phase-phase static correlation lengths** (pure $NbSe_3$, 90 K) [21]

  $\mathbf{a}^*$ : 0.80(15) µm

  $\mathbf{b}^*$ : 4.0(10) µm

  $\mathbf{c}^*$ : 0.75(5) µm

- **Energy gap**, measured by tunneling [22, 91] and optical spectroscopy [83]

  $\Delta_1 \sim 50\,\text{meV} - 140\,\text{meV}$

  $\Delta_2 \sim 20\,\text{meV} - 68\,\text{meV}$

- **Peierls transition temperatures** [79]

  $T_{p_1} = 145\,\text{K}$

  $T_{p_1} = 59\,\text{K}$

  (Approximately; the precise values depend on the measurement [58])

- **Conductivity** at 300 K ($b$-axis) [58]

  $\rho_{300} = 5.4(1) \times 10^5\,\Omega^{-1}\ \text{m}^{-1}$

- **Mass density** at 300 K [58]

  $\rho_m = 6.39\,\text{g/cm}^3$

- **CDW $T_{p_1}$ elastic constants**

| | | |
|---|---|---|
| longitudinal: | $K_z = 2.6 \times 10^8\,\text{N/m}^2$ | [20] |
| transverse: | $K_x = 3 \times 10^7\,\text{N/m}^2$ | [75] |
| | $K_x = 1.8 \times 10^7\,\text{N/m}^2$ | [40] |

- **CDW $T_{p_1}$ shear strength** [75]

  $\sigma_{xz} \sim 9.5 \times 10^3\,\text{N/m}^2$

- **Conductivity Anisotropy** [77, 93]

  $\sigma_b/\sigma_c \sim 20$

  $\sigma_b/\sigma_a \sim 100$

Hodeau et al. [39] carried out precise X-ray diffraction measurements of the $NbSe_3$ lattice structure, which is diagrammed in Figs. 1.5 and 1.6. Each Nb atom lies at the shared apex of two triangular Se prisms; these are stacked into chains in the $b$ direction. Weak interchain Nb-Se bonds connect the chains in the $c$ direction, but only van der Waals forces bind adjacent chains in the $a$ direction. As Fig. 1.6 shows, there are three distinct types of chains. Scanning-tunneling microscopy (STM) measurements indicate that it is primarily the type-III chains that carry the $T_{p_1}$ CDW [17].

This highly anisotropic lattice structure is reflected in the morphology of $NbSe_3$ crystals. These grow in the form of long, flat ribbons, with the length direction along $b$, and the shortest dimension along $a$, and the width along $c$. The crystals are easily cleaved along the $bc$ or $ab$ planes. Sizes vary widely, but typical crystals used in the present work had dimensions on the order of 1 cm long by 10 µm wide by 0.5 µm thick.

The electrical resistivity, too, is anisotropic. The ratio of the $c$-axis resistivity to the $b$-axis resistivity is $\rho_c/\rho_b \approx 20$ [77], and the $a-b$ anisotropy is on the order of 100 [93]. Finally, the lattice structure leads to Fermi surface nesting and the opening of a gap along a portion of the Fermi surface [88, 89]. Since the gapping is incomplete, however, $NbSe_3$ remains metallic below both Peierls transition temperatures. The screening of the CDW deformations by uncondensed carriers plays an important role in the CDW dynamics [50].

The threshold field $E_T$ for CDW conduction depends on the thickness of the crystal ($a$ direction). For thin crystals ($\lesssim 1$ µm), $E_T$ varies as $1/t$, where $t$ is the thickness [58]. Almost all as-grown $NbSe_3$ crystals have thickness steps along one or both faces. This gives rise to multiple threshold fields, and to shear between the CDWs in regions of different thickness; thus, "ideal" behavior can be observed only in extremely rare perfect specimens. Thickness steps are typically visible under an optical microscope, but small-angle grain boundaries and

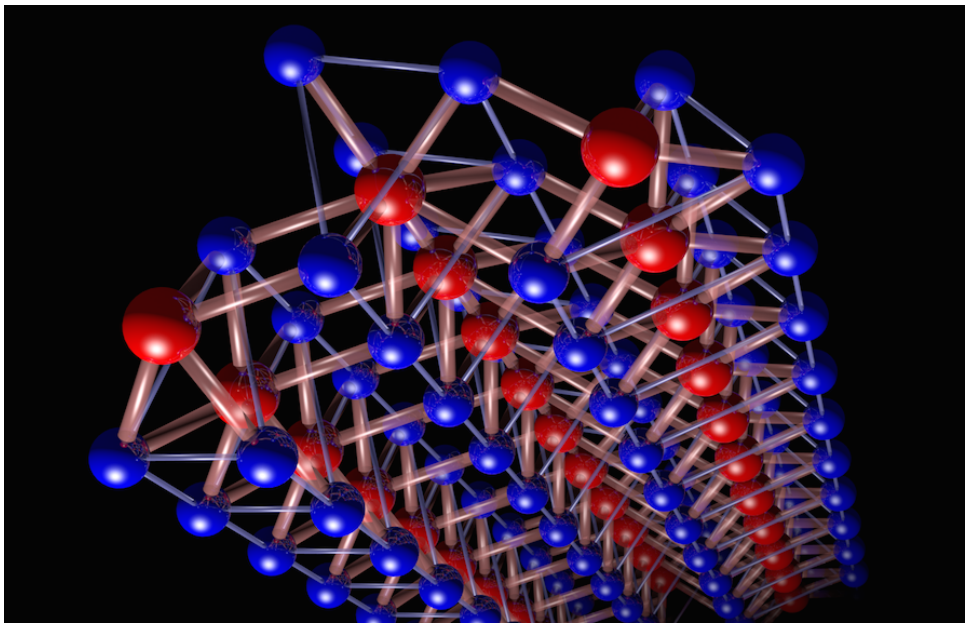

Figure 1.5: The $NbSe_3$ lattice structure comprises chains of triangular pyramids, with Nb (red) at the apices and Se (blue) at the corners, stacked along the $b$ axis. Structural parameters are those given by [39].

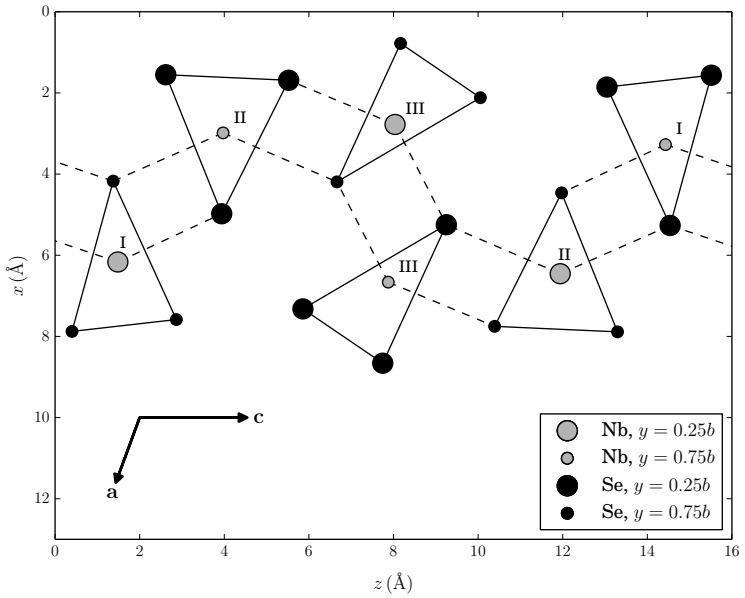


Figure 1.6: The $NbSe_3$ unit cell, projected onto a plane perpendicular to the $b$ axis. All atoms are located in either the $y = 0.25b$ (large circles) or $y = 0.75b$ (small circles) planes. The bases of the triangular Se prisms are drawn with solid lines, and the weak Nb-Se interchain bonds are shown as dashed lines. Only van der Waals forces bond adjacent chains together in the $a$ direction. There are three distinct types of chains, labeled I, II, and III. After Hodeau et al. [39].

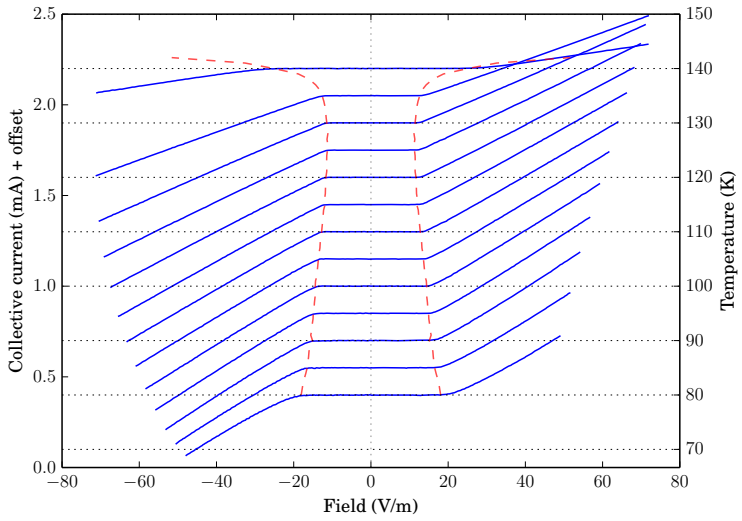


Figure 1.7: Curves of collective current $I_c$ vs. field $E$, plotted at 5 K increments from 80 K to 140 K. The curves are offset vertically for clarity; the origin of each curve is aligned with its temperature on the right-hand scale. The dashed curves mark the location of the threshold field $E_T$. Sample dimensions: 0.43 µm thick × 72 µm wide × 3 mm long.

other internal defects can also destroy the coherence of the CDW dynamics.

The pinning regime in $NbSe_3$ has been the subject of debate. Careful transport measurements in high quality samples are most readily explained in terms of weak pinning [58], but strong pinning may also occur, particularly near large lattice defects [87].

## 1.3 Temperature Dependence

Several important CDW characteristics vary significantly with temperature. Figure 1.7 plots $I - V$ curves for a $NbSe_3$ sample at temperatures from 80 K to 120 K, showing the temperature dependence of the threshold field $E_T$ and the high-field CDW conductivity $\sigma_\infty = \lim_{E\to\infty} j_c/E$.

The collective current density above threshold is well fit by the form

$$j_c(E) = \begin{cases} \sigma_\infty E_T \left( \sqrt{\sigma_1^2 + (E/E_T)^2} - \sigma_1 \right), & E > E_T \\ 0, & E \le E_T \end{cases} \tag{1.3}$$

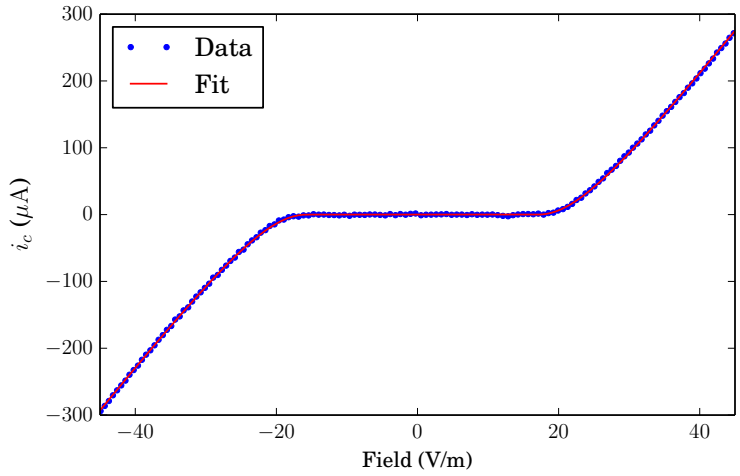


Figure 1.8: Fit of CDW current vs. bias field at $T = 80\,\mathrm{K}$. Measurements are shown as dots; the fit as a solid line.

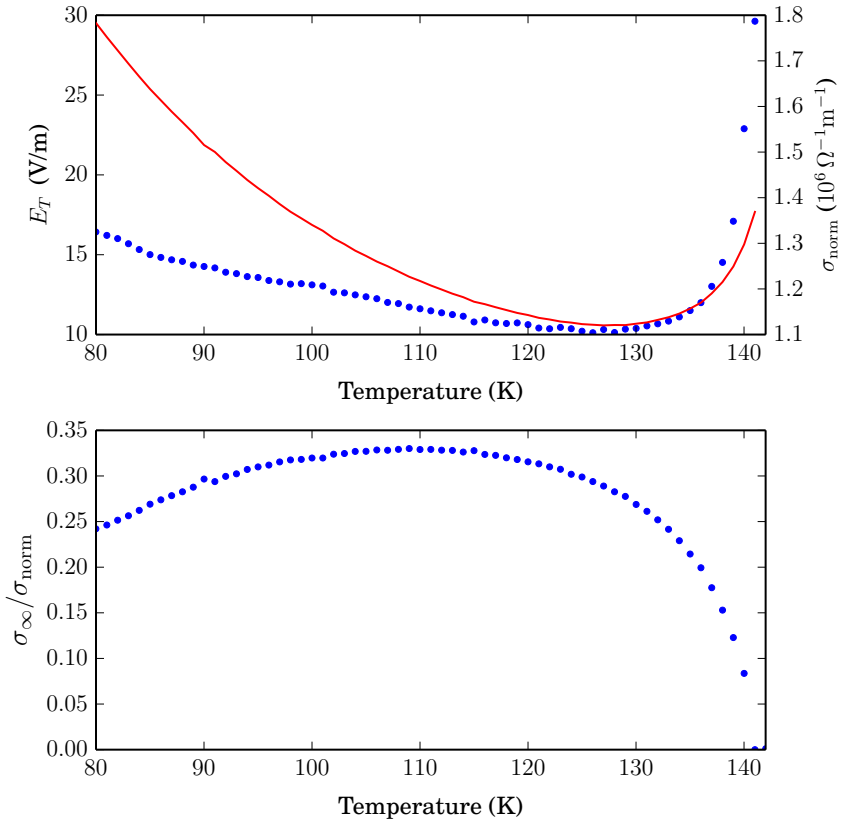


Figure 1.9: Top: threshold field for conduction $E_T$ vs. temperature (dots). For comparison, the normal conductivity over the same temperature range is also plotted (solid curve). Bottom: ratio of limiting high-field CDW conductivity $\sigma_\infty$ to normal conductivity $\sigma_{\mathrm{norm}}$, vs. temperature.

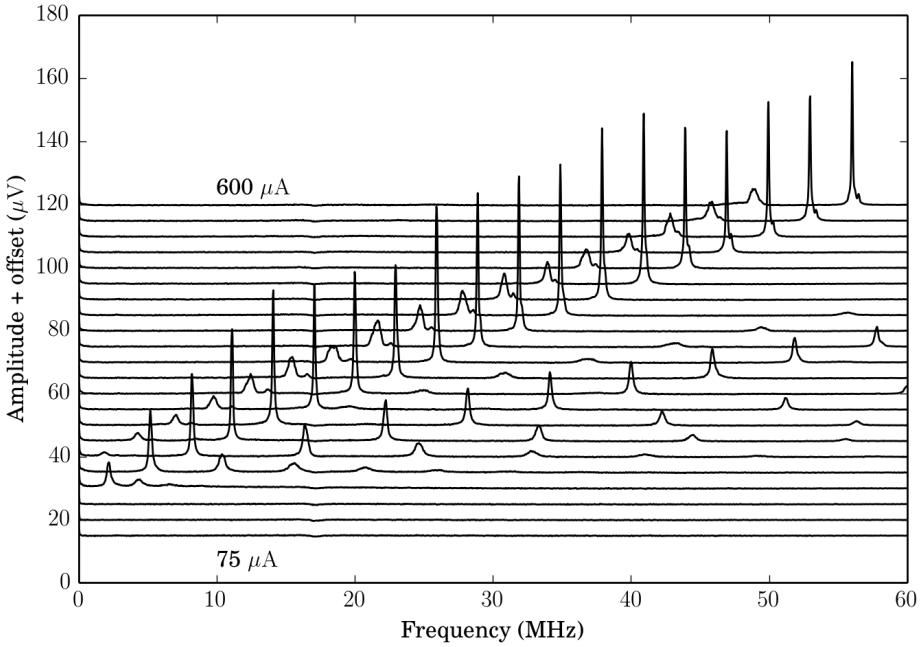


Figure 1.10: NBN spectra at DC bias current increments of 25 µA. This sample has a threshold of $I_T = 100\,\mu A$ and displays a sharp fundamental peak, and also a small shear domain at a lower frequency. The first four harmonics of the fundamental are visible. $T = 85\,K$.

where $E_T$ is the threshold field for CDW conduction, $\sigma_\infty$ is the limiting high-field CDW conductivity, and $\sigma_1$ is a dimensionless constant which describes the "rounding" at the depinning transition. Figure 1.8 shows a sample fit, and Fig. 1.9 plots the results of fitting Eq. 1.3 to $I - V$ curves taken over a range from 80 K to 140 K. The threshold field $E_T$ diverges as the Peierls transition temperature is approached from below, is at a minimum in the vicinity of 125 K, and increases again with decreasing temperature [58]. The limiting CDW conductivity $\sigma_\infty$ follows a similar pattern, reaching a maximum at approximately 110 K.

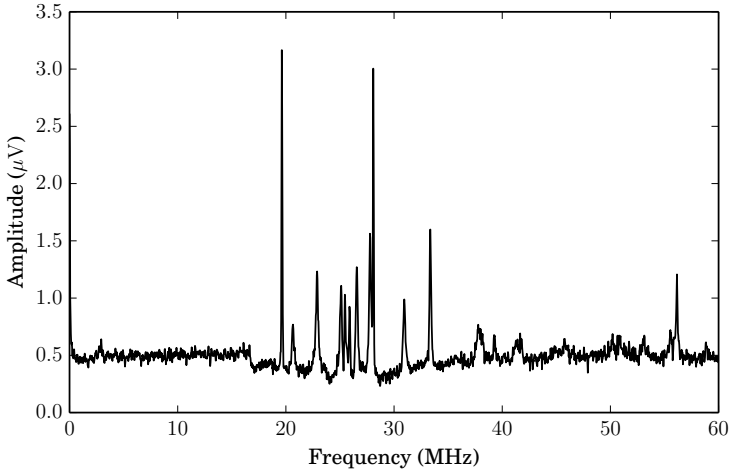


Figure 1.11: Spectrum of an incoherent sample. The CDW is broken up into many small domains with different sliding velocities, producing a broad distribution of spectral peaks. $T = 85\,\mathrm{K}$.

## 1.4 Voltage Oscillations

Because of its periodic spatial structure, a sliding CDW generates quasi-periodic voltage oscillations[1] at the "washboard" frequency

$$f_0 = \frac{1}{2\pi}\frac{d\phi}{dt} = \frac{v}{\lambda}$$

where $v$ is the sliding velocity, and $\lambda$ is the CDW wavelength; and at harmonics [24, 103]. The voltage oscillations are typically called narrow-band noise (NBN), despite the fact that they are not noise in the usual (random) sense. These provide the most direct experimental access to the spatiotemporal evolution of the CDW velocity. In previous experiments, the voltage oscillations were measured through the current contacts, and so represented an average over the entire sample length. The present work employed high-performance differential amplifiers to measure the NBN with spatial resolutions on the order of $50\,\mu\mathrm{m}$.

The NBN spectra of coherent CDW regions exhibit sharp, single peaks and harmonics.

[1]Since the CDW is shunted by the normal conductivity of the sample, the voltage oscillations produce oscillations of the sample *current*, which are often measured instead.

In regions where there is shear or phase slip, different portions of the CDW slide with different velocities, and so generate NBN at different frequencies. This broadens, or even splits, the spectral peaks. Figure 1.10 shows the NBN spectra for a relatively coherent sample. The NBN peak frequency increases nearly linearly with the current above the threshold. For comparison, Fig. 1.11 shows a single spectrum spectrum from a highly incoherent sample. There are many small peaks, corresponding to regions of the CDW with different sliding velocities. Measurements of the NBN spectra thus provide a sensitive test of sample coherence.

Sliding CDWs also generate incoherent broad-band noise (BBN) with an $f^{-\alpha}$ spectral distribution [24]. This noise is largest in samples with thickness steps, suggesting that velocity shear is a major source of BBN [53].

## 1.5 Mode Locking

Simultaneous application of a DC bias and a radio-frequency AC bias produces interference between the "natural" NBN washboard frequency and the driving frequency. For certain combinations of AC and DC biases, the CDW locks its sliding frequency to a rational multiple of the drive frequency [68, 102]. Matsukawa provided a quantitative explanation of this behavior within the framework of the FLR model [56]. The mode-locked regions have finite width; these appear as plateaus in the CDW current vs. DC bias characteristic. Figure 1.12 shows a plot of the differential resistance ($dV/dI$) vs. DC bias, with a simultaneously applied RF bias. (The differential resistance shows the mode-locking plateaus more clearly than a simple $I - V$ curve.)

Peaks in the differential resistance appear wherever the CDW's sliding velocity matches its washboard frequency to the driving frequency. If the CDW is completly mode-locked, the differential resistance reaches its below-threshold value. Partial locking (e.g. locking of some fraction of the cross-sectional area) produces smaller peaks.

For this reason, the completeness of mode-locking, particularly on the 1:1 peak, has

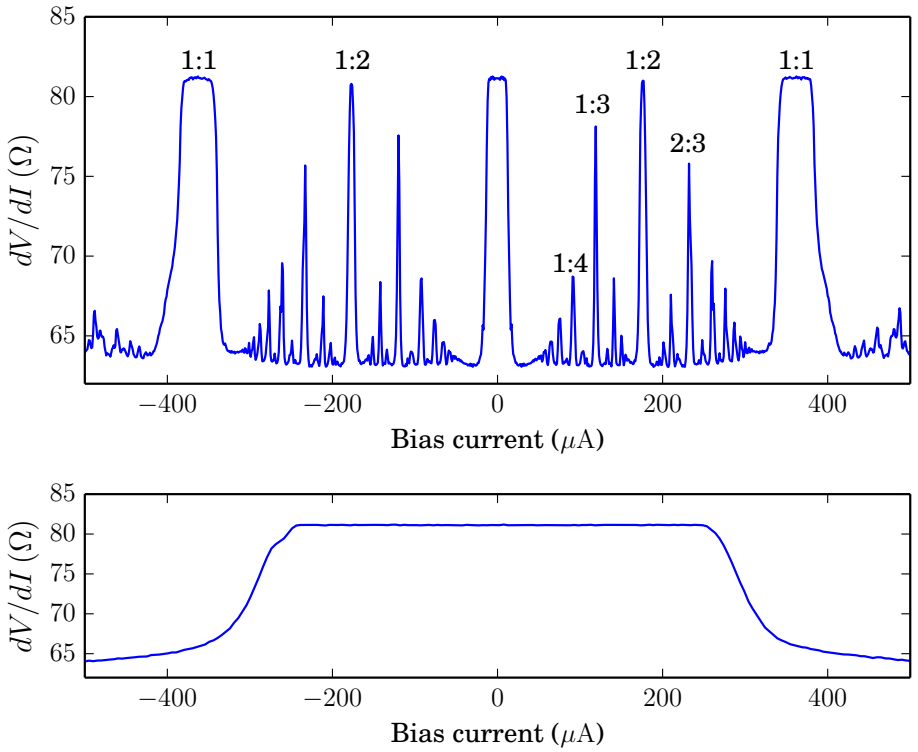


Figure 1.12: Upper panel: Mode locking of a CDW in response to a simultaneous DC bias and RF drive of 260 mV RMS at 15 MHz. The differential resistance $dV/dI$ was measured using a lock-in technique, while the DC bias was swept from −500 µA to 500 µA. The CDW locks at sliding velocities where its washboard frequency is a rational multiple of the AC drive frequency (peak labels). This sample shows complete locking at the 1:2 and 1:1 steps, and dozens of partially-locked subharmonics are visible. Lower panel: Same configuration as top, except with no RF drive. $T = 90$ K.

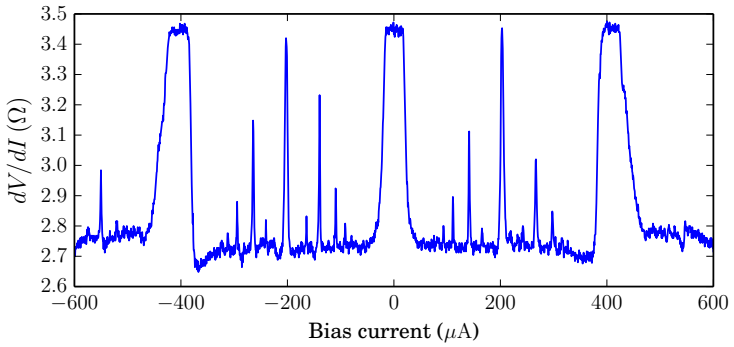


Figure 1.13: Mode-locking curve of the same sample as in Fig. 1.11 (which exhibits an incoherent DC NBN spectrum), showing complete mode locking at the 1:1 peaks and positive 1:2 peak. AC bias: 243 mV RMS at 10 MHz. $T = 120$ K.

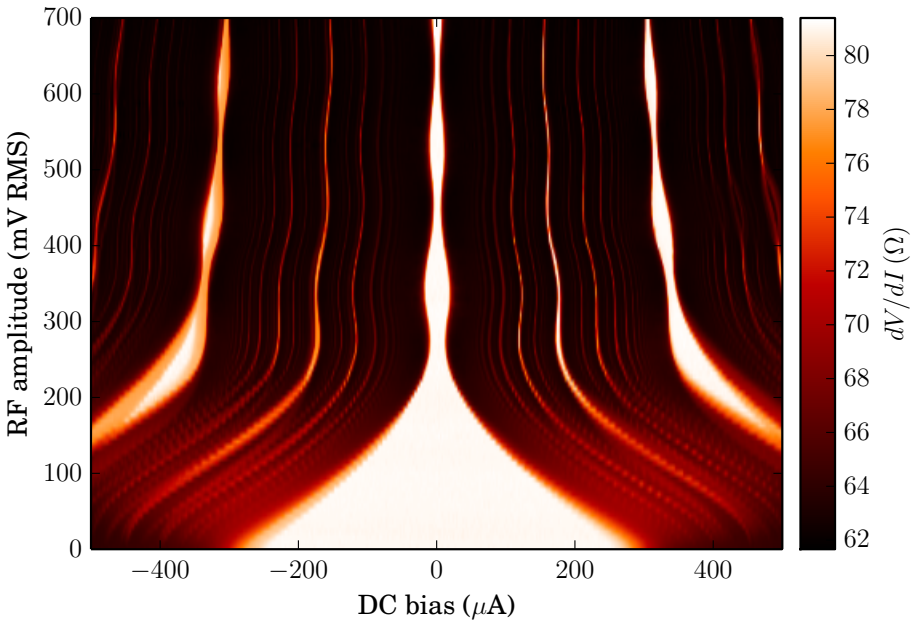


Figure 1.14: Differential resistance $dV/dI$ as a function of both DC bias and AC amplitude, for a 15 MHz RF drive. $T = 90\,\mathrm{K}$.

often been used as an indicator of sample quality and coherence [58, 94, 104]. This is usually valid—samples with large thickness steps or other defects will not lock—but the finite width of the mode-locked peaks can "pull" together regions which are not coherent under a DC bias alone. Figure 1.13 shows the mode locking behavior of the same sample whose spectrum is plotted in Fig. 1.11. The $dV/dI$ peaks are somewhat asymmetrical, but nevertheless exhibit complete locking at the 1:1 peak.

The widths of the mode-locking peaks vary in a sinc-like fashion with the amplitude of the AC drive. Figure 1.14 shows a two-dimensional plot of the differential resistance as a function of both the DC bias and the AC drive amplitude.

# Chapter 2

# Spatially-Resolved Transients

## 2.1 Introduction

The Fukuyama-Lee-Rice (FLR) model [28, 29, 44, 45, 96] provides an equation of motion for the CDW phase $\phi$:

$$\gamma\frac{\partial\phi}{\partial t} = \mathbf{K}\cdot\frac{\partial^2\phi}{\partial\mathbf{r}^2} + \left(\frac{en_c}{Q}\right)E + n_1\sum_{i=1}^{N_{\mathrm{imp}}}\delta(\mathbf{r}-\mathbf{r}_i)\sin(\mathbf{Q}\cdot\mathbf{r}+\phi) \tag{2.1}$$

where $\gamma$ is a damping constant, $\mathbf{K} = (K_x, K_y, K_z)$ are the elastic constants, $e$ is the elementary charge, $n_c$ is the condensate number density, $E$ is the external electric field in the in-chain (here taken as $z$) direction, and the final term accounts for interactions with impurities.

This model predict a purely elastic response. Sliding states of driven elastic systems are asymptotically unique and exhibit locally and globally periodic evolution in time [61]. It follows that measured current and voltage oscillations should be periodic as well, with infinitesimal spectral line widths.

However, plasticity plays at least two crucial roles in the dynamics of real CDW conductors: One, at current contacts, collective charge must be converted to single-particle charge, or vice-versa. In a typical experimental configuration, current is injected and re-

moved through side contacts. The CDW slides in the region between the contacts, but remains pinned beyond them, so wavefronts must be added or removed near the contacts. This process is driven by large-scale strain gradients, which have been observed in both voltage [2, 4, 46] and X-ray diffraction [20, 85, 86, 93] measurements. These strains result in longitudinal phase slip near the current contacts. Theories [14, 15, 16, 78] suggest that phase slip occurs via the formation and growth of dislocation loops.

Two, sample inhomogeneities can result in shear slip (we distinguish between longitudinal *phase* slip, $dj_c/dz$, and *shear* slip, $dj_c/dx, dj_c/dy$). For example, in thin samples, the threshold field for conduction $E_T$ is inversely proportional to the sample thickness [58]. Thus, thickness steps in the transverse direction lead to shear strain; this has been directly observed by X-ray diffraction [40, 48, 84]. Shear strain beyond an elastic limit causes shear slip [53, 58, 75].

These mechanisms destroy the periodicity of the CDW voltage and current oscillations. Narrowband "washboard"-frequency peaks are broadened and split; and large amplitude (orders of magnitude larger than thermal noise) low frequency $1/f^\alpha$ noise appears. Although the CDW motion can be nearly homogeneous under ideal conditions (a flawless sample, measured far from the current contacts, at high temperature), inhomogeneous motion results in a rich array of phenomena which can furnish insights into the fundamental physics of CDWs [58, 69, 75].

Shear and slip lead to complex spatiotemporal dynamics, both in the CDW's nominally steady sliding state, and especially in its transient response to changes in the DC bias field. Previous studies [2, 4, 47] have measured the transient response indirectly, via the low frequency ($\lesssim 1\,\mathrm{MHz}$) voltage fluctuations across pairs of contacts. This voltage is related to the collective current by $I_c = I - V/R_s$, where $I$ is the total current, $R_s$ is the single particle resistance, and $V/R_s$ is the single particle current; the CDW velocity can then be found as $v = I_c/(n_c A)$, where $v$ is the CDW sliding velocity, and $A$ is the cross-sectional area.

Using the voltage to determine $v$ in this way depends on the assumption that the single particle resistance $R_s$ is independent of voltage and time; this is a fairly good approximation

in the partially gapped $NbSe_3$ at high temperatures (except, perhaps, in regions of high strain [16]), but it is a poor approximation for $NbSe_3$ at low temperatures, and in fully gapped materials such as $TaS_3$ or $K_{0.3}MoO_3$. Other studies [23, 30, 31, 81, 98, 103] have measured the transient response of the current through the entire sample. These measurements have relatively high bandwidth, but provide no spatial information.

A much more direct way to probe the CDW motion is to measure the frequencies of the voltage oscillations that accompany collective current flow. The frequencies of these oscillations are proportional to the CDW sliding velocity: $v = f\lambda$, where $\lambda = 2\pi/Q$ is the CDW wavelength. Thus, measuring the voltage oscillations between closely spaced voltage contacts, over a wide bandwidth, can map out the CDW dynamics with high temporal and spatial resolution. However, since sliding frequencies range from tens of kilohertz near $E_T$, to hundreds of megahertz, these measurements are not trivial.

The high performance amplifiers employed in this work provide much more complete information about the spatiotemporal evolution of the CDW, than was previously available. It is possible to track the positions of individual peaks in frequency, corresponding to coherent CDW domains, across both time and position along the sample.

## 2.2 Experimental Methods

### 2.2.1 Sample Mounting

High purity $NbSe_3$ crystals were grown according to the procedures in Appendix A. Single-crystal samples were selected and laid atop arrays of 20 nm high gold traces on alumina substrates, and secured with a thin film of ethyl cellulose. Voltage contacts were all 2 µm wide; contacts of this width have been shown to be nonperturbing in $NbSe_3$ at temperatures up to 130 K [46]. Current contacts were at least 100 µm wide, which, along with the high thermal conductivity of the substrates, minimized sample heating. Several substrate patterns were used; each had pairs of voltage contacts at various distances along the length of the

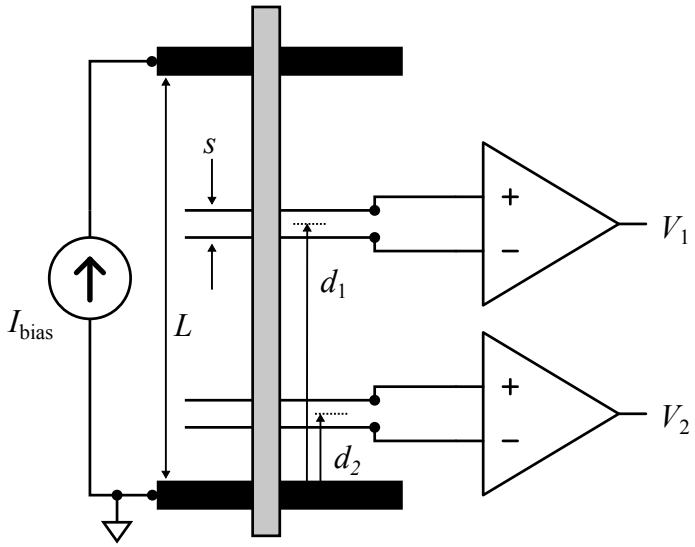


Figure 2.1: Experimental configuration. Alumina substrates are patterned with 20 nm thick Au traces. A crystal of $NbSe_3$ is laid atop the traces and secured by a polymer film. Voltage contacts are 2 µm wide; current contacts are at least 100 µm wide. Differential amplifiers placed near the sample amplify the voltage across adjacent contact pairs. The separation of each voltage contact pair is denoted by $s$, and the distance from the ground contact to the center of the pair by $d$.

sample. Two pairs (one for each differential amplifier) were connected at any given time. Figure 2.1 defines the dimensions which we hereafter use to specify contact locations.

More closely spaced voltage contact pairs give better spatial resolution, but, since the voltage is proportional to the separation $s$, worse signal-to-noise ratios. For the present work, 50 µm was a typical spacing.

The length and width of the samples was measured using an optical microscope, and the thickness was determined from their room-temperature resistance and the known $NbSe_3$ resistivity of $1.85 \times 10^{-6}\,\Omega\,\mathrm{m}$ [58].

The substrates were mounted on a solid copper block, which was placed in a gas-tight tube immersed in a liquid nitrogen bath. An electronically controlled heater affixed to the copper block stabilized the temperature to within 2 mK, over a range from 78 K to 150 K.

### 2.2.2 Amplifier Design

Previous studies of CDW voltage noise [2, 4, 30, 31, 47] have relied on room-temperature amplifiers. As mentioned above, this configuration severely limits the available measurement bandwidth: the relatively high sample contact resistances ($\sim$ 1 k$\Omega$) combine with wiring capacitances ($\sim$ 100 pF) to form a low-pass filter ($f_c \sim$ 1 MHz). Additionally, the high-impedance signal from the sample to the amplifier is susceptible to interference, and the thermal noise of a room-temperature amplifier can be significant.

Placing the amplifier in the cryostat overcomes these deficiencies: the short leads have small capacitances; the metal cryostat enclosure shields the circuit; and the low temperature minimizes thermal noise. We have developed an amplifier based on Ref. [5]. However, our version uses a symmetrical, fully differential cryogenic stage, combined with a room-temperature differential-to-single-ended amplifier (Fig. 2.2) Compared with the design in [5], this offers greatly improved common-mode rejection ratio (CMRR) and bandwidth. (The high CMRR, in particular is crucial for isolating the noise from a particular segment of the sample).

A differential pair of NESG3031 silicon-germanium heterojunction bipolar transistors (SiGe HBT) forms the input stage. These transistors benefit from a very high current gain $\beta$ at cryogenic temperatures, which allows the amplifier to simultaneously achieve low noise, low input bias current ($\sim$ 50 nA), and high input impedance.

A pair of transimpedance amplifiers formed around OPA836 low-noise, low-power SiGe op amps holds the collectors of Q1 and Q2 at approximately 0 V, reducing the Miller effect and allowing the amplifier to reach a -3 dB bandwidth of 60 MHz. [1] The cryogenic stage has a differential gain of approximately 30 V/V and a noise floor of $0.9\,\mathrm{nV\,Hz^{-1/2}}$ at 77 K.

The differential signals are conducted to room temperature through a pair of solid coaxial cables. Finally, an AD8129 differential receiver provides an additional gain of 10 and

[1] While it is possible to replace each op amp with a discrete cascode and emitter follower, as in Ref. [6], we find that the op amps offer greater stability and lower output impedance.

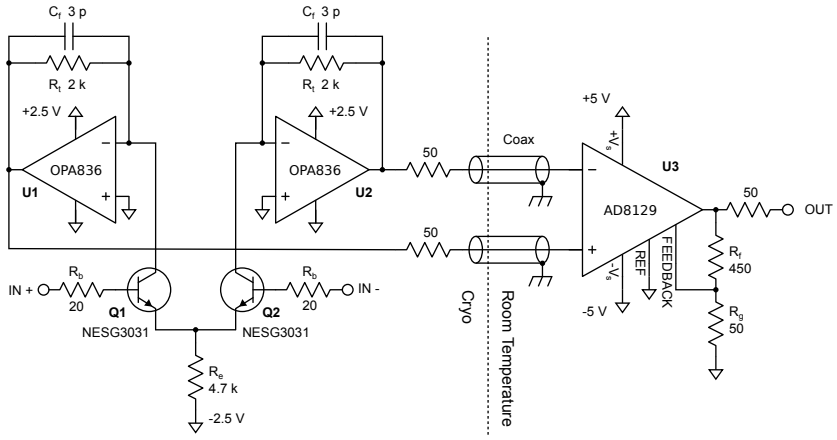


Figure 2.2: Low noise differential amplifier. Q1 and Q2 form a differential pair, while U2 and U3 are configured as transimpedance amplifiers, improving bandwidth and reducing output impedance. Re sets the collector current of Q1 and Q2. Rt sets the transimpedance. Cf and Rb improve stability and flatten the frequency response. The cryogenic stage is connected to room temperature by a pair of 40 cm rigid coaxial cables. U3 is set for a differential gain of 10. The amplifier has an overall gain of approximately 300 V/V; a -3 dB bandwidth of 60 MHz; a noise floor of $0.9\text{nV}/\sqrt{(\text{Hz})}$ at 77 K; and a CMRR of 90 dB at 1 MHz.

further improves the CMRR. Two identical complete amplifiers measure the voltage across two different segments of the sample. To further reduce noise, the amplifiers are powered by batteries. The entire system, including the cryogenic stage, the room temperature amplifier, and the power supply, are enclosed within a continuous metal shield. The amplifier circuit boards are located just below the sample stage and remain at approximately 77 K, independently of the sample temperature.

The voltage signals from the amplifiers are digitized and recorded by a digital oscilloscope with an analog bandwidth of 400 MHz and a sampling rate of up to $5 \times 10^9$ samples/s (5 GSPS). In order to resolve transients in both frequency and time, we compute the spectrogram of the voltage signal:

$$S(t, f) = \left| \int_{-\infty}^{\infty} w(\tau - t) V(\tau) e^{-2\pi i f \tau} \, d\tau \right|^2 \tag{2.2}$$

where $w(t)$ is a window function. Longer windows give better frequency resolution, but poorer time resolution, and vice-versa. The spectrograms which appear here were averaged over many repeated traces, in order to reduce noise and improve clarity, but in each case, several single-shot spectrograms were examined to verify that there was little or no trace-to-trace variation in the signal of interest.

## 2.3 Results

### 2.3.1 Transients far from contacts

Figure 2.3 shows the response of a sample with $L = 3\,\text{mm}$ to a periodic train of current pulses, measured at a voltage contact pair with $d = 1100\,\mu\text{m}$ and $s = 50\,\mu\text{m}$. The periodic pulse train was chosen carefully. It comprises a pair of negative pulses of $I = 3.2I_T$, followed by a pair of positive pulses of the same magnitude; thus, every other pulse reverses the CDW's direction of motion. The current is returned to zero for a period of $300\,\mu\text{s}$ after each pulse, which ensures that the magnitude of each current *step* is the same.

The spectrogram exhibits several notable features. First is the pulse-sign-memory effect, first described in [30]; but here, we are measuring the sliding velocity of the CDW, rather than the total sample current. The velocity shows an exponential-like increase to the steady state value when the previous pulse was in the same direction, but it "overshoots" when the preceding pulse was of the opposite sign.

Second, the dynamics are asymmetrical with respect to the CDW sliding direction. This is especially apparent in the transient response to a current reversal, but it also results in slightly different steady-state sliding velocities for opposite but equal-magnitude current biases.

Third, immediately after each current reversal, the washboard peak is broadened and split into multiple sub-peaks (particularly for the negative to positive transition). Over a time of $\sim 500\,\mu\text{s}$, the sub peaks merge into a single sharp peak. Successive pulses of the

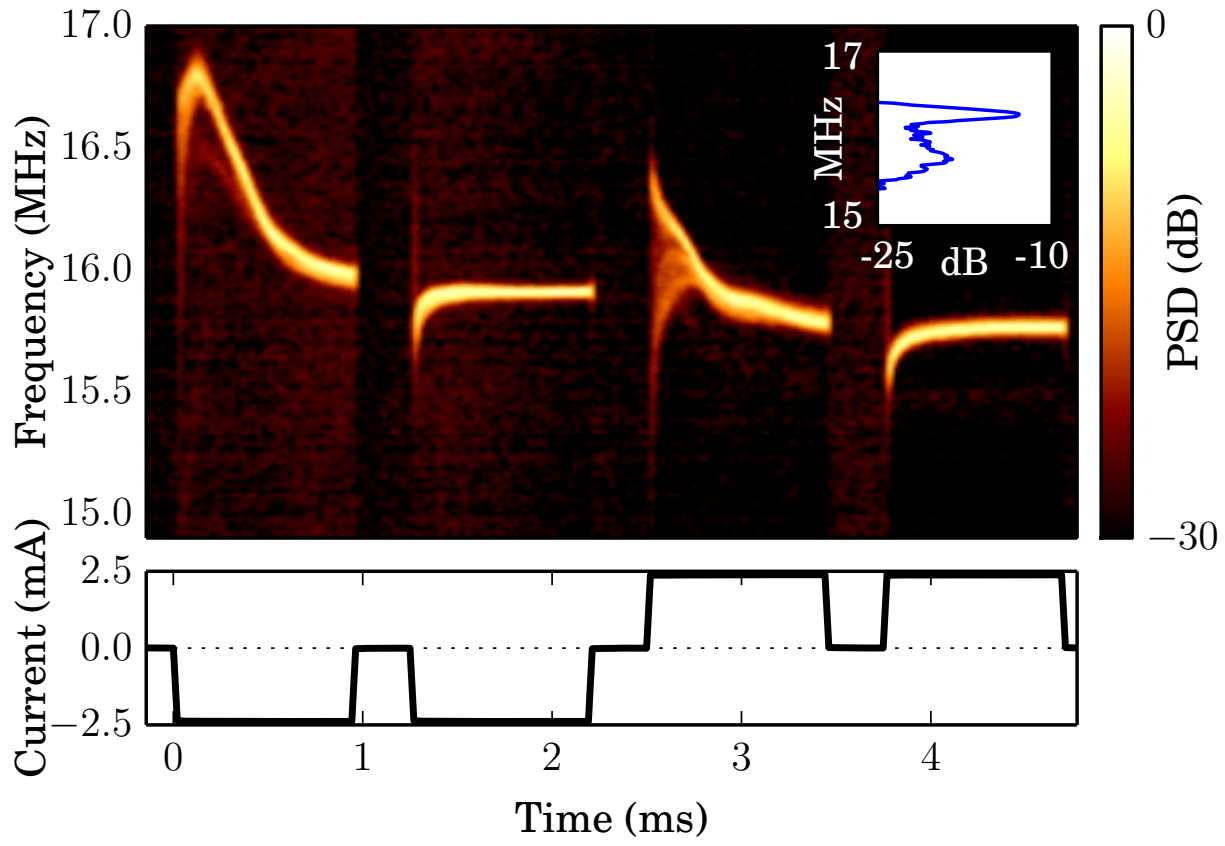


Figure 2.3: Spectrogram of voltage across a contact pair near the middle of the sample, in response to the periodic bias current profile shown in the lower panel. Immediately after each current reversal, the narrowband peaks are split, but they merge over a time $\sim 0.5\,\mathrm{ms}$. The dynamics also exhibit asymmetry with respect to the bias current direction. The inset shows the power spectral density $50\,\mu\mathrm{s}$ after the beginning of the third pulse. Sample 1, $T = 90\,\mathrm{K}$. Signal digitized at 100 MSPS; spectrogram window length 4096 samples.

same sign do not produce this splitting.

### 2.3.2 Transients near contacts

The dynamics of the CDW close to current contacts are more complex, due to the phase slip which must occur for collective current to flow. Figure 2.4 shows the frequencies measured at two nearby voltage pairs, both with $s = 50\,\mu\text{m}$ spacing, centered at $d_1 = 175\,\mu\text{m}$ (pair 1) and $d_2 = 75\,\mu\text{m}$ (pair 2) from the nearest current contact. The periodic bias pulse sequence was similar to that in Fig. 2.3. The (sample 2) was of high quality; it exhibited complete mode locking (measured at 10 MHz) and had no visible defects or thickness steps.

The transient following the negative-to-positive current reversal is of particular interest. The CDW region at pair 2 initially shows a coherent response, but 250 µs after the start of the pulse, the frequency of the peak drops sharply, and the broadband noise level increases; this can be seen more clearly in Fig. 2.5. At the same time, the CDW region at pair 1 exhibits a transient "bump," but remains coherent. The dynamics are markedly asymmetrical with respect to the current direction. The breakup of the peak at pair 2 occurs only for the positive pulses, in which the CDW is sliding *towards* the nearby current contact. Both pairs show a coherent response when the CDW is moving away from the current contact.

At higher temperatures, however, both segments remain coherent, and the dynamics are more symmetrical with respect to the current direction. Figure 2.6 shows the behavior at 100 K.

### 2.3.3 Nonlocal transients

The drift of dislocations may play an important role in CDW dynamics. We have attempted to detect the motion of transients in the following way: A DC bias current is applied to the sample for several seconds, to establish a steady state. A brief (1 µs), intense ($\sim 50 I_T$) differential current pulse is applied to a contact pair near the middle of the sample. This might reasonably be expected to generate a local excess of dislocations [16, 35, 85]. Since the

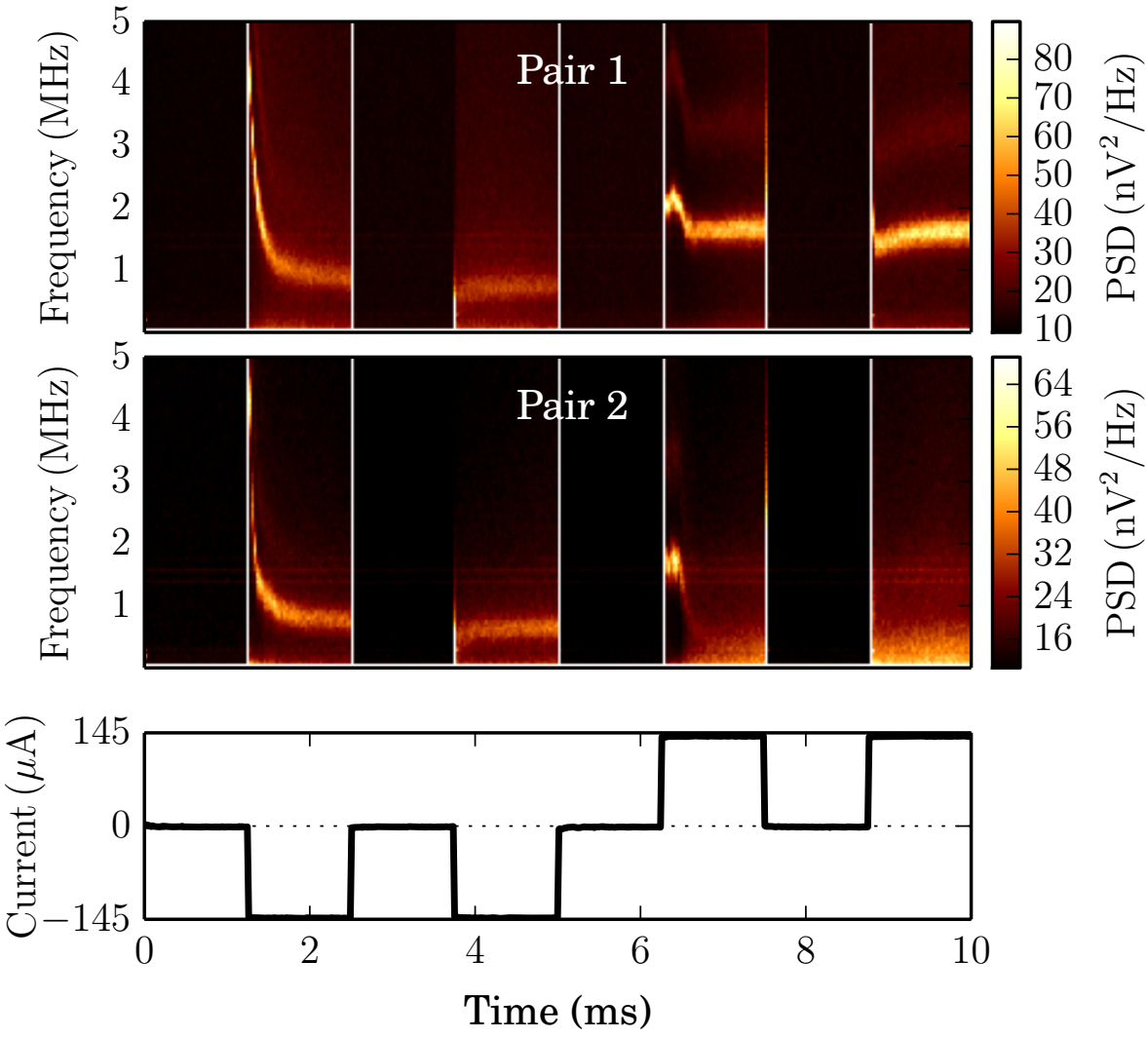


Figure 2.4: Spectrogram at $T = 85\,\mathrm{K}$ of voltage across two contact pairs in response to the bias current pulses shown in the lower panel. Both contact pairs have 50 µm separation; their center distances from the nominally negative current contact are 175 µm and 75 µm for pair 1 and pair 2, respectively. For the first positive current pulse (CDW sliding *away* from the nearby current contact), the spectral peak for pair 2 is initially sharp, but 250 µs later, it undergoes a sudden steep drop in frequency, accompanied by a large increase in broadband noise. The CDW at pair 1 remains coherent. Signals digitized at 250 MSPS; spectrogram window length 4096 samples.

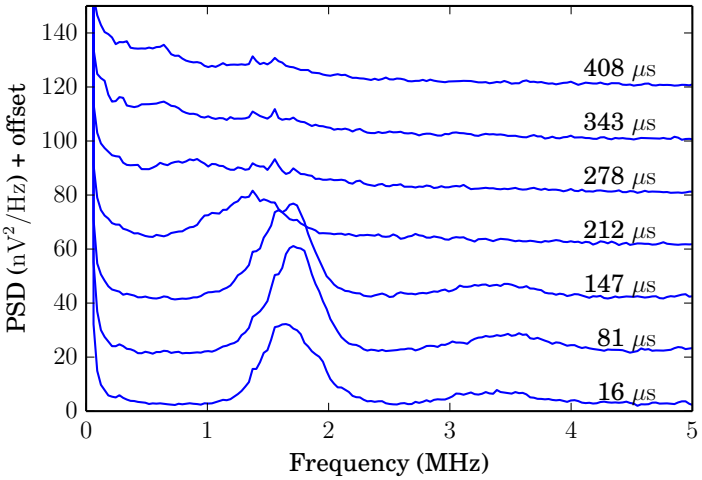


Figure 2.5: Evolution of the power spectral density for voltage pair 2 for the negative-to-positive transition (third pulse) in Fig. 2.4. For clarity, spectra at successive times are offset along the vertical axis. Each line is labeled with the time elapsed from the beginning of the pulse.

current pulse is differential, its immediate influence should be confined to the region near the pulse contact pair. The transient response at other nearby contact pairs is recorded. Figure 2.7 shows this configuration.

If dislocations are carried along with the CDW's motion, they should reach "downstream" contacts after a time $L/v = LQ/(2\pi f)$, where $v$ is the CDW sliding velocity and $f$ is the narrowband peak frequency. No unambiguous downstream delayed transients could be detected on this time scale, over a range in sliding frequency from 1 MHz to 60 MHz, and a range of contact spacings from 100 µm to 1000 µm, corresponding to hypothetical time delays from to 1 ms to 700 ms.

However, delayed transients on shorter time scales were observed (Fig. 2.8). These were most prominent when the CDW moved in the direction from the detection pair towards the stimulus pair—i.e., delayed transients were observed "upstream" of the stimulus pair. The velocity implied by the 50 µs delay in Fig. 2.8 over the 800 µm distance is 16 m/s; this is much greater than the CDW sliding velocity (and in the opposite direction, in this case), but much less than the phason velocity. The delay time did not vary with the bias current

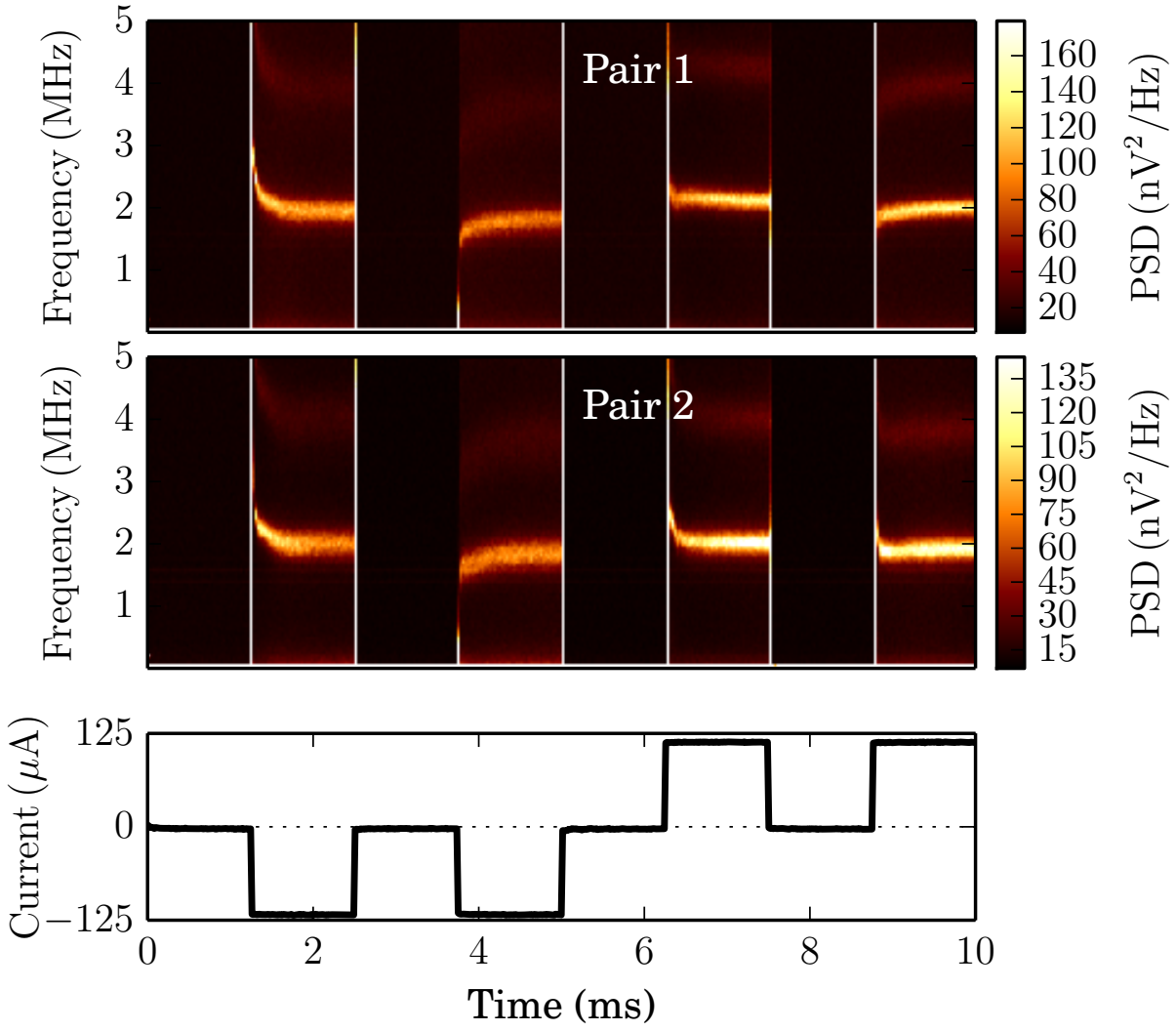


Figure 2.6: Spectrogram taken with the same sample and contacts as in Fig. 2.4, but at $T = 100\,\mathrm{K}$; the bias current has been reduced slightly to maintain approximately the same $E/E_T$ ratio. At this temperature, there is no apparent phase slip in the observed regions.

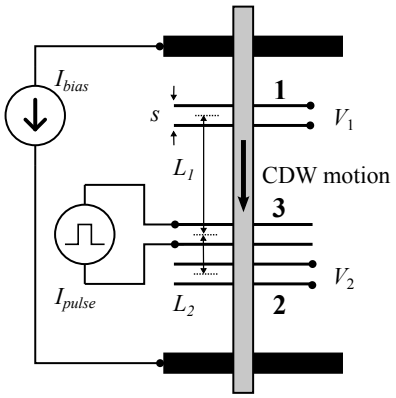


Figure 2.7: Contact configuration for nonlocal transient measurements. A brief current pulse is applied to pair 3, and the response is recorded at pairs 1 and 2. All pairs have separation $s = 50\,\mu\text{m}$ and are located at least $1000\,\mu\text{m}$ from the current contacts; the center-to-center distances of pairs 1 and 2 from pair 3 are $L_1 = 800\,\mu\text{m}$, and $L_2 = 100\,\mu\text{m}$, respectively.

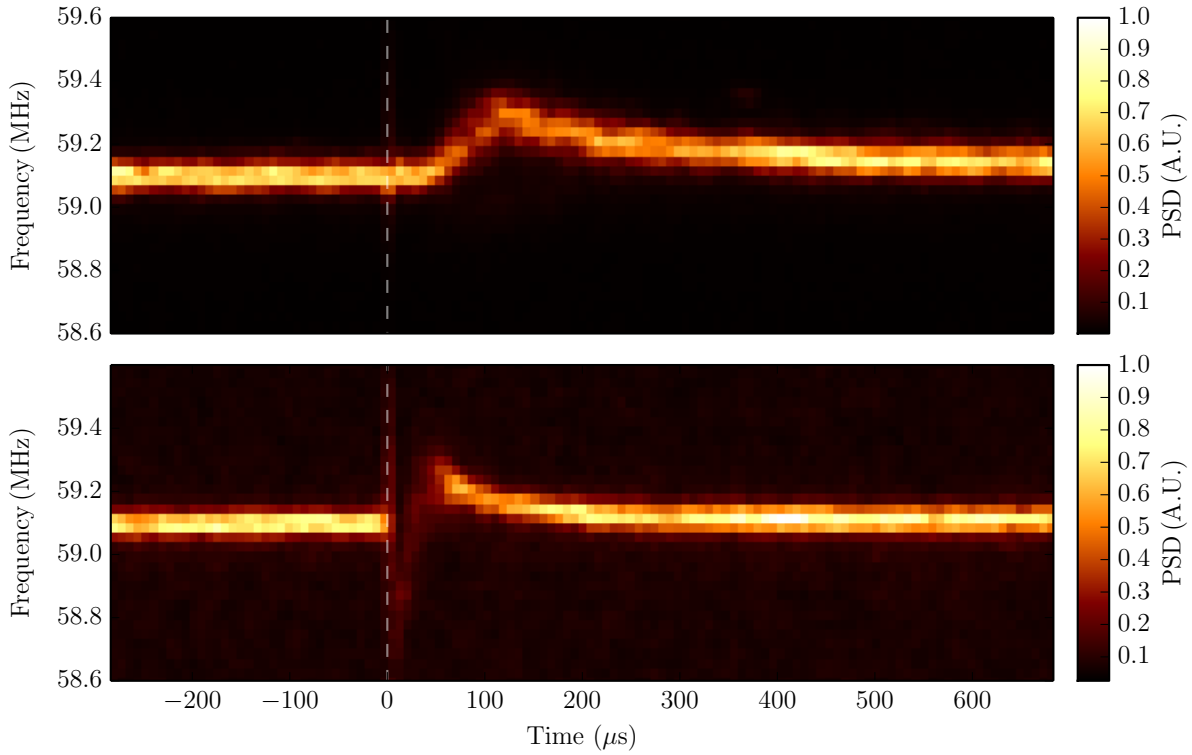


Figure 2.8: Delayed transient response to a $1\,\mu\text{s}$ pulse in the direction opposite the CDW motion, applied to contact pair 3 at $t = 0$ (marked by the dashed line). Top: contact pair 1, located $800\,\mu\text{m}$ upstream of pair 3. Bottom: contact pair 2, $100\,\mu\text{m}$ downstream of pair 3. Pair 2 shows an immediate transient in response to the pulse, but the response at pair 1 is delayed by approximately $50\,\mu\text{s}$. Sample 1, $T = 80\,\text{K}$.

over a NBN peak frequency range from 24 MHz to 59 MHz.

### 2.3.4 Relaxation below threshold

When the bias current is reduced below threshold, it might be expected that the CDW strains will relax via thermal creep. In order to examine the relaxation rate, a sample was subjected to a periodic train of current pulses of $1.5I_T$ for 50 ms, separated by variable time intervals of zero bias current. For "bipolar" measurements, the measurement pulse was immediately followed by a pulse of opposite sign, but equal magnitude and duration. Using the spectrogram technique described above, the peak frequency as a function of time was extracted. Transients due to parasitic inductance and capacitance of the external circuitry were on the order of 100 ns, several orders of magnitude shorter than the time scale of the CDW transients. Many traces were averaged for each relaxation interval, but these were interleaved in a random order to avoid potential systematic errors due to thermal drift and other processes.

This technique does not give direct access to the relaxation process, but the transient after the start of a current pulse depends strongly on the initial CDW configuration. In particular, elastic displacement produces a polarization transient [4]: if the CDW is initially strained in the direction opposite to that of its motion under the new bias current, the elastic restoring force produces a transient sliding velocity greater than that which would result from the external field alone, which we term an "overshoot."

Figure 2.9 demonstrates this behavior. For short relaxation times, there is a large polarization transient. For longer relaxation times, the transient becomes smaller, and even becomes negative at the near-end contact. Since this "undershoot" cannot be unbounded, it must saturate on a time scale longer than that measured during the experiment (several minutes).

Figure 2.10 shows the degree of overshoot $\Delta f = f(t = 0) - f(t = 50\,\text{ms})$ as a function of the relaxation time. At least two distinct regions of logarithmic relaxation are visible: an

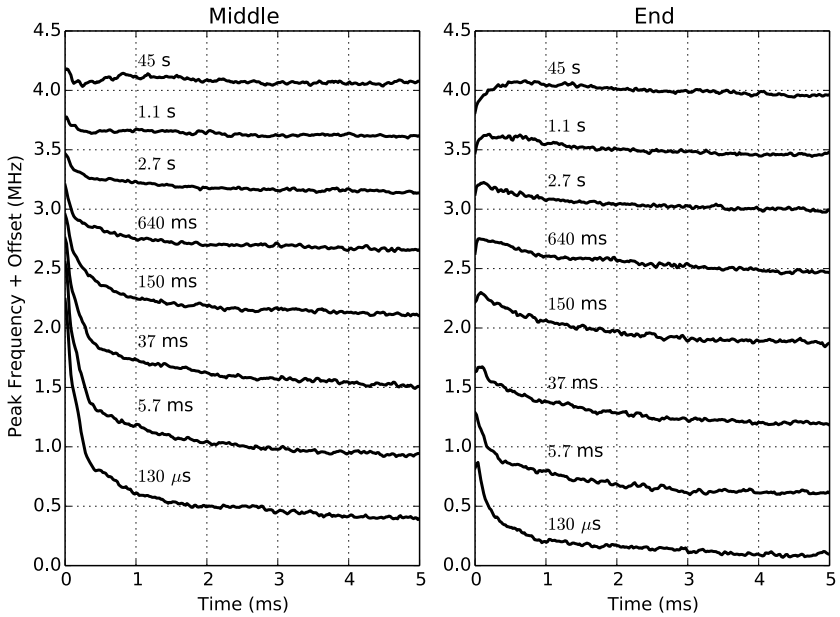


Figure 2.9: Transient frequencies in response to a current pulse of opposite sign to the preceding one, after variable relaxation intervals of zero bias current. Curves are labeled with the relaxation time in between pulses, and are offset for clarity. The "middle" contact pair is located 500 µm from either current contact, and the "end" pair is 75 µm from the positive end. Sample 2, $T = 90\,\mathrm{K}$.

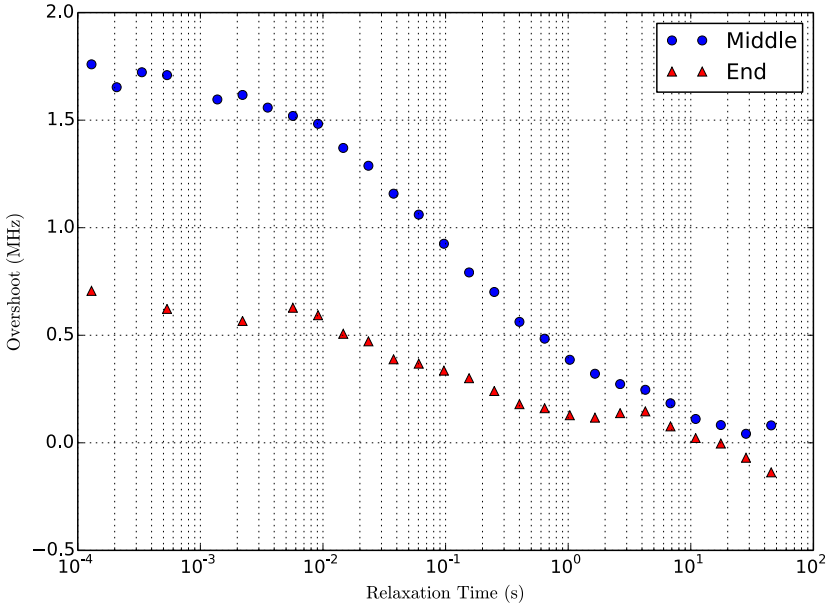


Figure 2.10: Transient overshoot $\Delta f = f(t = 0) - f(t = 50\,\mathrm{ms})$ in response to a current pulse of opposite sign to the preceding one, after variable relaxation intervals of zero bias current, using the same configuration as in Fig. 2.9, at $T = 90\,\mathrm{K}$

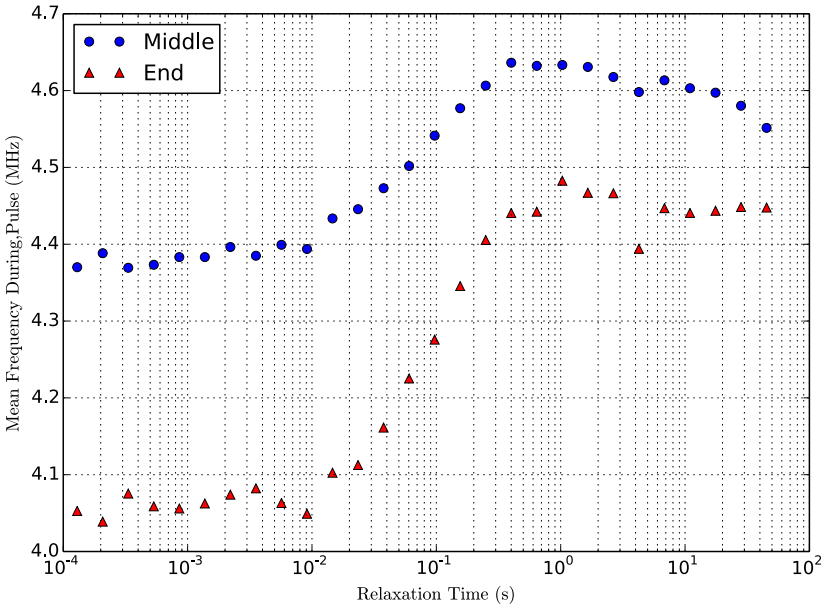


Figure 2.11: Mean sliding frequency during the measurement interval, in response to a current pulse of opposite sign to the preceding one, after variable relaxation intervals of zero bias current, using the same configuration as in Fig. 2.9.

initial slow decay, followed by a faster one after 10 ms. At the near-end pair, the transient becomes an undershoot after approximately one second.

Finally, Fig. 2.11 plots the average sliding frequency during the measurement intervals. Since only the length of the relaxation intervals was varied, this apparently reflects a duty-cycle effect. Again, there is a region of slow relaxation up to approximately 10 ms, followed by a logarithmic decay up to slightly less than one second.

The transient response to separated pulses of the *same* sign is slightly more complex. Figures 2.12, 2.13, and 2.14 show plots analagous to those for the bipolar case. For all traces, the peak frequencies increase with time following the beginning of each pulse. The magnitude of the frequency transient increases logarithmically with increasing relaxation time, up to $t_r = 10$ ms, at which time the behavior changes qualitatively. For longer relaxation times, the CDW motion splits: the initial frequency undershoot differs between the near-end contact and the middle contact. For relaxation times longer than 100 ms, the magnitude of both increases at a slower rate than for $t_r < 10$ ms; again, these presumably saturate at times

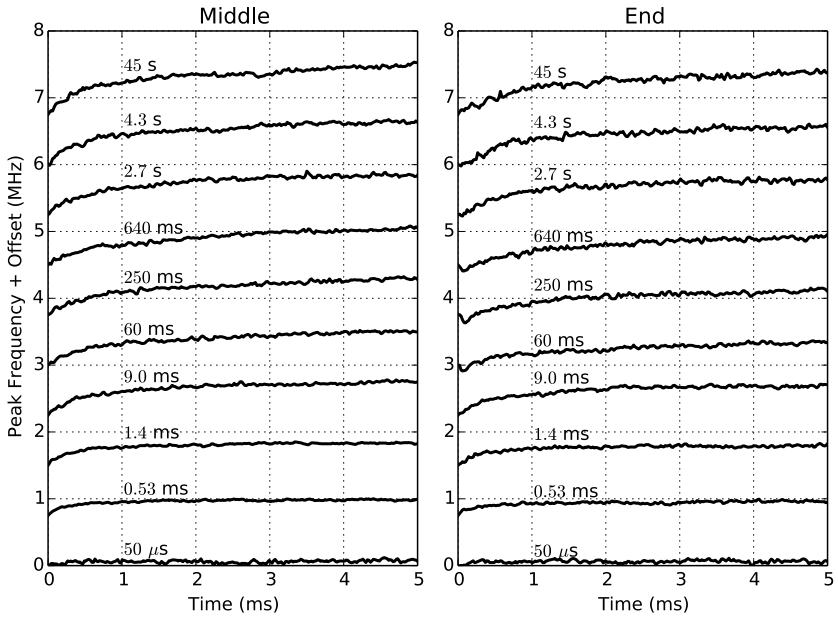


Figure 2.12: Transient frequencies in response to a current pulse of the *same* sign as the preceding one, after variable relaxation intervals of zero bias current. Curves are labeled with the relaxation time in between pulses, and are offset for clarity. The "middle" contact pair is located 500 µm from either current contact, and the "end" pair is 75 µm from the positive end. Sample 2, $T = 90\,\mathrm{K}$.

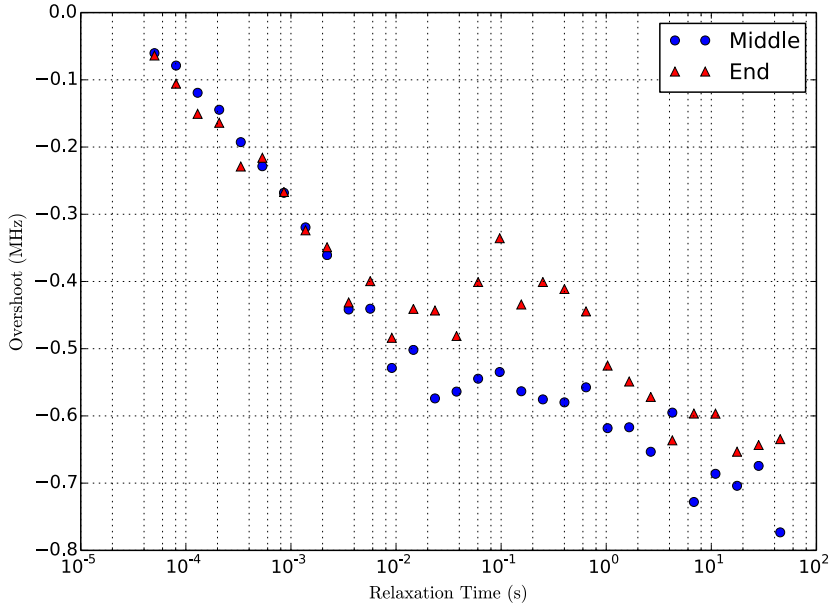


Figure 2.13: Transient "overshoot" $\Delta f = f(t = 0) - f(t = 50\,\mathrm{ms})$ in response to a current pulse of the same sign as the preceding one, after variable relaxation intervals of zero bias current, using the same configuration as in Fig. 2.9.

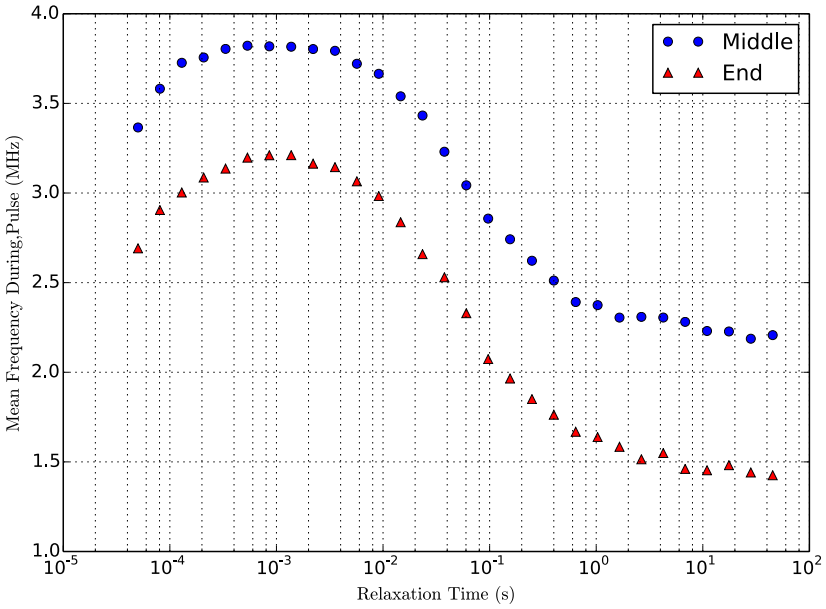


Figure 2.14: Mean sliding frequency during the measurement interval, in response to a current pulse of the same sign as the preceding one, after variable relaxation intervals of zero bias current, using the same configuration as in Fig. 2.9.

longer than were observed here.

The mean sliding frequency again exhibits a duty cycle effect, but it is not monotonic. For small relaxation times, the sliding frequency increases with relaxation time, reaching a maximum at $t_r = 1.0\,\mathrm{ms}$ and then decreasing thereafter.

The size of the transients is strongly temperature dependent. Figure 2.15 compares the relaxation in the bipolar case at $T = 90\,\mathrm{K}$ and $T = 100\,\mathrm{K}$. At higher temperatures, the transients become too small to be readily measured.

Figure 2.16 demonstrates another relaxation effect. The voltage contacts in this experiment were widely spaced (800 µm). With a DC bias, or with short relaxation intervals, the there is a single voltage oscillation peak, but longer relaxation intervals lead to a transient splitting of the peak. According to the argument which we develop below, this splitting persists for too long to be due to elastic shear alone.

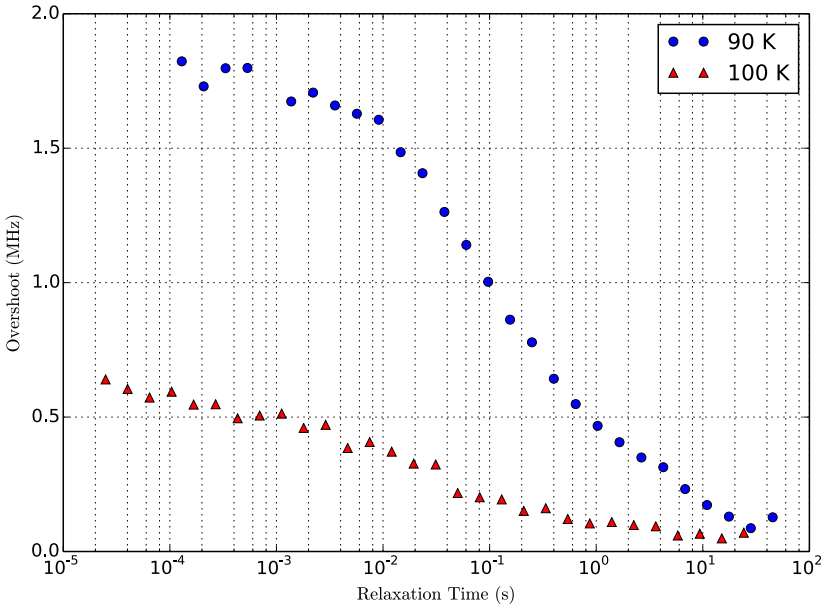


Figure 2.15: Comparison of relaxation for bipolar pulses at $T = 90\,\mathrm{K}$ and $T = 100\,\mathrm{K}$, using the same configuration as in Fig. 2.9.

### 2.3.5 Relaxation above threshold

The CDW dynamics also exhibit slow, glassy relaxation in the *sliding* state. Figure 2.17 shows the evolution of the sliding velocity during current pulses after a long (1200 s) relaxation interval of zero bias current. The only difference between the experimental configurations for the two curves was the sign of the previous pulse, which rules out heating as the source of the transients.

### 2.3.6 Noise below threshold

Theoretical work has predicted a critical divergence of avalanche sizes as the threshold for conduction is approached from below [60, 63, 70, 73, 74]. To search for this divergence experimentally, a sample was biased with sinusoidal alternating currents at $f \sim 100\,\mathrm{Hz}$ with varying amplitudes, near the threshold for depinning. (A sinusoidal drive was chosen to avoid ringing transients.) The threshold was estimated from the differential resistance of the sample as a function of bias current (Fig. 2.18). The threshold is not sharp, so its exact

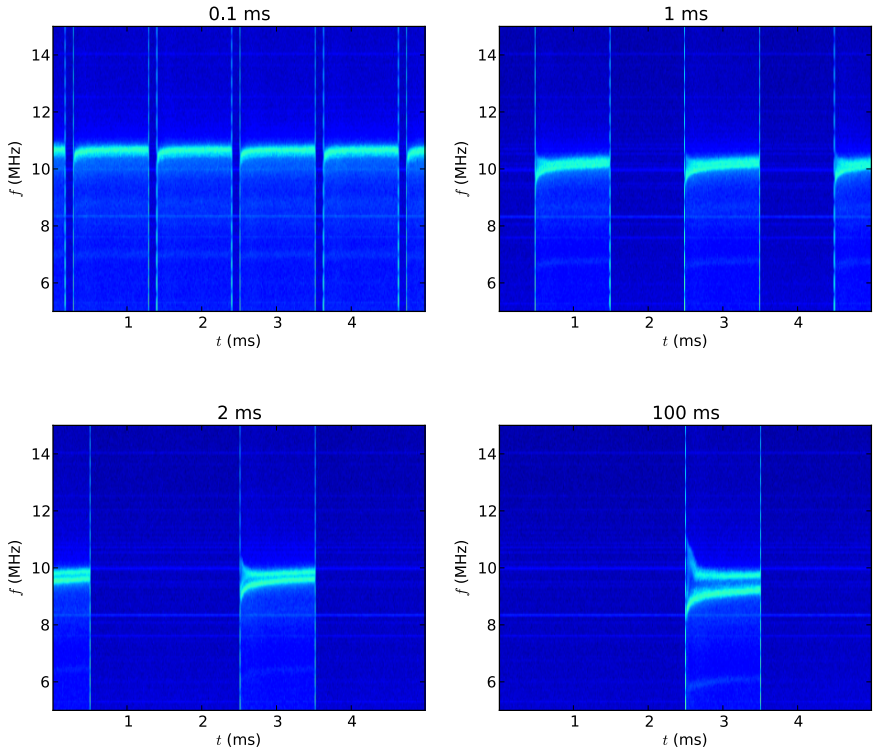


Figure 2.16: Response to repeated 1 ms current pulses of $\approx 1.2 I_T$, separated by various relaxation intervals. The label for each subplot gives the relaxation time. Voltage contacts separated by 800 µm. For short relaxation intervals, there is one voltage oscillation peak, but for longer intervals, the peak splits. Sample 3, $T = 90$ K. Contact pair with spacing $s = 800$ µm.

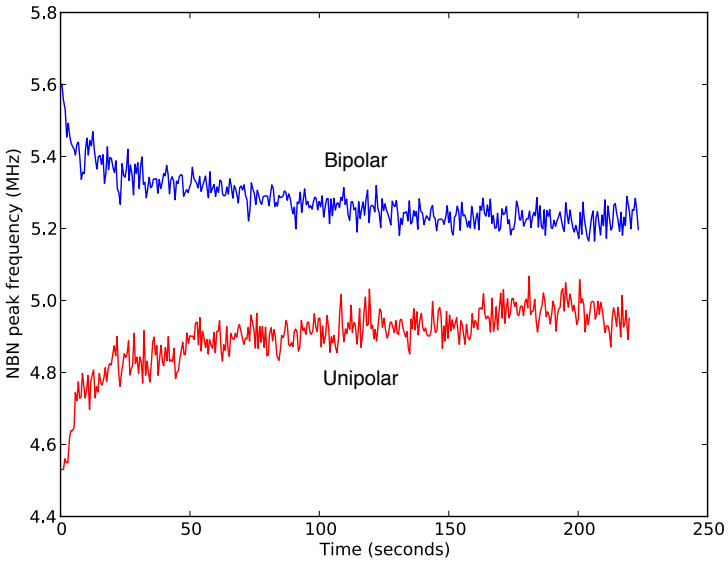


Figure 2.17: Slow transient relaxation of sliding velocity in response to repeated pulses of the same (bottom curve) and opposite (top curve) sign as the previous pulse. Sample 2, $T = 81\,\mathrm{K}$.

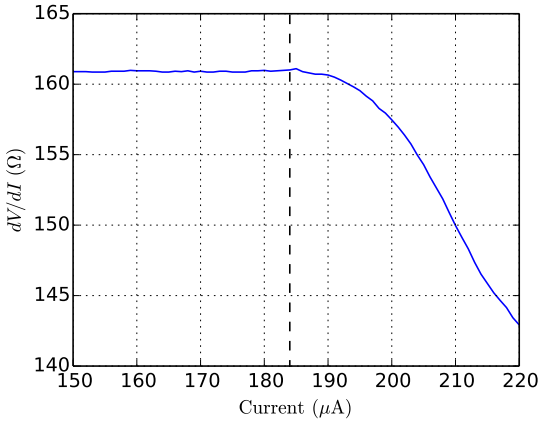


Figure 2.18: Differential resistance vs. bias current of Sample 4 at $T = 120\,\mathrm{K}$. The vertical dashed line shows the estimated location of the threshold for sliding, $I_T = 184\,\mu\mathrm{A}$.

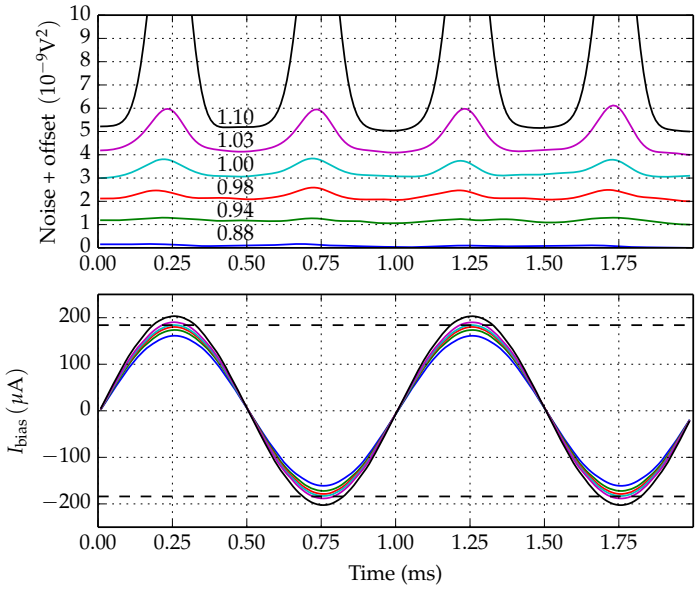


Figure 2.19: Noise in response to 1 kHz alternating bias currents with amplitudes near threshold. Top panel: voltage noise for several bias current magnitudes. The numbers above the curves indicate the ratio $\max(|I(t)|)/I_T$ of the maximum bias current to the threshold current determined from the data in Fig. 2.18. Curves are offset for clarity. Bottom panel: bias current profiles. The dashed lines show the estimated threshold current $I_T$. Sample 4, $T = 120\,\mathrm{K}$.

location is somewhat ambiguous. Furthermore, this threshold is the *total* threshold, which includes the force necessary to drive phase slip at the current contacts. The *bulk* threshold required to overcome pinning forces alone is smaller.

The total voltage noise in a 0-5 MHz bandwidth was recorded as a function of time; the bias current was recorded simultaneously. Curves were averaged over $10^3$ cycles. No excess noise is visible below $0.98I_T$, and the noise increases exponentially *above* threshold. Measurements at temperatures from 80 K to 130 K produced similar results. This suggests that avalanches, if they exist, must be small; or that the critical region is very narrow. It has also been proposed [62] that thermal rounding might suppress the appearance of avalanches.

## 2.4 Analysis and Discussion

In the following, we choose a coordinate system such that $z$ is the sample crystal's in-chain direction, $x$ is in the width direction, and $y$ is along the thickness (the smallest dimension). The CDW sliding velocity is given by

$$v = \frac{1}{Q}\frac{\partial \phi}{\partial t} \tag{2.3}$$

and the washboard frequency (narrowband "noise" frequency) is

$$f = \frac{1}{2\pi}\frac{\partial \phi}{\partial t} = \frac{Q}{2\pi}v = \frac{v}{\lambda} \tag{2.4}$$

where $\lambda$ is the CDW wavelength. The $NbSe_3$ $T_{p_1}$ wavevector is $Q = 0.24\mathbf{b}^*$ [26], with $b^* = 2\pi/3.4805\,\text{Å}$ [39], so $Q = 4.39\,\text{nm}^{-1}$ and $\lambda = 1.43\,\text{nm}$.

### 2.4.1 Elastic shear

There are two possible sources of the initial peak splitting observed in response to current reversals (Fig. 2.3): first, a longitudinal velocity gradient ($\partial v/\partial z \neq 0$); second, shear

($\partial v/\partial x \neq 0$ or $\partial v/\partial y \neq 0$). Recall that the contact pair had a separation of only $s = 50\,\mu\text{m}$, and was located near the middle of the sample, more than 1 mm from the nearest current contact, so a significant longitudinal splitting seems unlikely. However, we can estimate the strain that such a longitudinal splitting would produce: The most distant sub-peaks (in the third pulse of Fig. 2.3) are separated by $\Delta f \approx 300\,\text{kHz}$, and they merge after a time $\Delta t \approx 250\,\mu\text{s}$. Therefore, the minimum strain developed over that time would be[2]

$$\epsilon_z \approx \frac{1}{2}\frac{(\Delta f)(\Delta t)\lambda}{s} = 1 \times 10^{-3}.$$

This is larger than the maximum longitudinal strains observed *near current contacts* [20, 85, 86]; strains near the middle of the sample are much smaller [4, 20, 85, 86]. We thus rule out a longitudinal gradient as the dominant source of the splitting. (However, the transient "bump" in all of the sub-peaks is due to longitudinal strain.)

Instead, we the ascribe splitting and subsequent convergence of the peaks in Fig. 2.3 to shear and the buildup of shear strain. If different transverse regions of the sample have different $i_c$ vs. $E$ characteristics, then in the absence of shear stress, the corresponding regions of the CDW will slide at different velocities (for the same bias). However, this leads to a buildup of shear strain; if the elastic limit is not exceeded, then the transverse regions must eventually slide at the same velocity, with the faster portions "dragging" the slower ones along.

Due to pinning, this shear strain cannot completely relax when the bias current ceases. Thus, at the start of a new pulse in the other direction, strains are in the opposite direction from their steady-state values; they initially *increase* the shear splitting.

Sample 1 is rectangular in cross section (as observed though an optical microscope). It shows a coherent response in the steady state: a single, sharp washboard peak, and complete mode locking (measured at 10 MHz). Nevertheless, it is likely not entirely homogeneous in

[2]The factor of $\frac{1}{2}$ appears because the CDW undergoes a *reversal* of strains at the beginning of the reverse-polarity current pulse; that is, the change in strain is twice the steady-state value.

the transverse direction, due, perhaps, due to a deviation from a perfectly rectangular cross section, or to strain from its arrangement on the substrate.

We can estimate the magnitude of the steady state shear strain. The sample is much wider than it is thick ($h = 430\,\mathrm{nm}; w = 72\,\mu\mathrm{m}$), so we assume that the observed variation is in the width ($x$) direction. Using the same values as above for the frequency splitting $\Delta f$ and merging time $\Delta t$, we find the maximum shear strain to be

$$\gamma_{xz} \sim \frac{(\Delta f)(\Delta t)\lambda}{2w} = 8 \times 10^{-4} \tag{2.5}$$

This is comparable to shear strains measured by X-ray diffraction [40].

The time constant of the transient also provides a simple estimate of the shear modulus $G_{xz}$. To show this, we consider a simplified two-dimensional version of the FLR model:

$$\gamma \frac{\partial \phi}{\partial t} = K_x \frac{\partial^2 \phi}{\partial x^2} + K_z \frac{\partial^2 \phi}{\partial z^2} + \left(\frac{en_c}{Q}\right)(E - E_p) \tag{2.6}$$

where $E_p(j_c)$ is a phenomenological pinning field measured from the sample's $I - V$ characteristic [4]. For bias fields well above threshold (here, $E = 3.2E_T$), $E_p$ is nearly constant, so we will neglect its variation with the sliding velocity. The damping constant $\gamma$ can be determined from the measured limiting high-field CDW resistivity $\rho_c$:

$$\gamma = \rho_c \left(\frac{en_c}{Q}\right)^2. \tag{2.7}$$

We further specialize to the region far from the current contacts, where there is no $z$ dependence of the longitudinal strain ($\partial^2\phi/\partial z^2 = 0$), or external field ($\partial E/\partial z = 0$). However, we allow the pinning field to vary in the $x$ direction; this can result from, e.g., a non-uniform sample cross section. For simplicity, we consider the dynamics in a frame moving with the steady-state CDW velocity (i.e. where $\int_{-w/2}^{w/2}[E - E_p(x)]\,dx = 0$). The phase evolution is

described by a one-dimensional heat equation:

$$\frac{\partial \phi}{\partial t} = \frac{K_x}{\gamma}\frac{\partial^2 \phi}{\partial x^2} + \left(\frac{en_c}{Q\gamma}\right)[E - E_p(x)] \tag{2.8}$$

$$= \alpha^2 \frac{\partial^2 \phi}{\partial x^2} + \beta(x) \tag{2.9}$$

where, for compactness of notation, we have defined $\alpha^2 \equiv K_x/\gamma$ and $\beta(x) \equiv (E - E_p)en_c/(Q\gamma)$. The stress must vanish at the edges of the sample [40, 58], which we place at at $x = 0, x = w$, where $w$ is the sample width. The boundary conditions are

$$\left.\frac{\partial \phi}{\partial x}\right|_{x=0,w} = 0. \tag{2.10}$$

Equations 2.9 and 2.10 are readily soluble in terms of an eigenfunction expansion:

$$\phi(x,t) = \sum_{n=1}^{\infty} T_n(t)\cos(n\pi x/w) \tag{2.11}$$

where

$$T_n(t) = a_n e^{-t/\tau_n} + \beta_n \tau_n \left(1 - e^{-t/\tau_n}\right) \tag{2.12}$$

and $\tau_n = (\pi\alpha n/w)^{-2}$ are the time constants for the phase evolution, the $a_n$ are determined by the initial condition: $a_n = (2/w)\int_0^w \phi(t=0)\cos(n\pi x/w)\,dx$; and the $\beta_n$ are the Fourier coefficients of the pinning field variation: $\beta_n = 2en_c/(wQ\gamma)\int_0^w [E - E_p(x)]\cos(n\pi x/w)\,dx$.

The observed time scale for the elastic shear transient is determined primarily by the slowest time constant,

$$\tau_s \equiv \tau_1 = \left(\frac{w}{\pi\alpha}\right)^2 = \frac{(en_c w)^2 \rho_c}{Q^2 K_x} \tag{2.13}$$

The shear modulus is thus

$$G_{xz} = Q^2 K_x = \frac{(en_c w)^2 \rho_c}{\tau_s} \tag{2.14}$$

Substituting in the measured values for Sample 1 at 90 K ($\rho_c = 5.8 \times 10^{-6}\,\Omega\,\mathrm{m}$, $w = 72\,\mu\mathrm{m}$, and $\tau_s = 200\,\mu\mathrm{s}$), we estimate the shear modulus to be

$$G_{xz} \sim 1.4 \times 10^7\,\mathrm{N/m^2}.$$

This is comparable to the estimated values determined by scaling the longitudinal elastic constant $K_z$ by the ratios of the correlation lengths [75] and from the change in the total shear modulus of $NbSe_3$ upon CDW depinning [110]. The present measurement is, to our knowledge, the most direct measurement to date of the shear modulus in the *sliding* state.

The shear transient time constant shows no discernible variation with the pulse magnitude, over a range of sliding frequencies from 1 MHz to 25 MHz, which is in agreement with the prediction of Eq. 2.13. It does show a small temperature dependence, decreasing by a factor of approximately two from 80 K to 125 K.

Finally, we estimate the change in pinning field across the sample width required to produce this shear transient. In the steady state (i.e. long after the last current reversal),

$$\phi(x) = \sum_{n=1}^{\infty} \beta_n \tau_n \cos(n\pi x/w). \tag{2.15}$$

Next, the current is reversed at $t = 0$. Then $\beta_n \to -\beta_n$, and Eq. 2.15 determines the initial condition: $a_n = -\beta_n \tau_n$. The sliding velocities immediately after the current reversal are

$$\begin{aligned} \left.\frac{d\phi}{dt}\right|_{t=0_+} &= \sum_{n=1}^{\infty} (\beta_n - a_n/\tau_n) \cos(n\pi x/w) \\ &= 2 \sum_{n=1}^{\infty} \beta_n \cos(n\pi x/w) \end{aligned} \tag{2.16}$$

The bandwidth of the NBN peak at $t = 0$ is

$$\Delta f = \frac{1}{2\pi}\left(\max \left.\frac{d\phi}{dt}\right|_{t=0_+} - \min \left.\frac{d\phi}{dt}\right|_{t=0_+}\right). \tag{2.17}$$

Again, we consider only the first term in the expansion. Let

$$E - E_p(x) = \Delta E_p \cos(\pi x/w), \tag{2.18}$$

so that $\beta_1 = \Delta E_p e n_c/(Q\gamma) = \Delta E_p Q/(e n_c \rho_c)$. Then

$$\Delta f = \frac{2Q}{\pi e n_c \rho_c}\Delta E_p \tag{2.19}$$

which gives

$$\Delta E_p \sim 0.12\,\mathrm{V/m} \tag{2.20}$$

This is a factor of 160 less than the threshold field $E_T = 19\,\mathrm{V/m}$, which is consistent with the optically observed uniform cross section of this sample and the complete mode locking.

We also note that, using the form of $E_p$ in Eq. 2.18, the distribution of frequencies within the bandwidth is given by an arcsine distribution $\left(\pi\sqrt{\hat{f}(1-\hat{f})}\right)^{-1}$, where $\hat{f} = (f - f_{\min})/(\Delta f)$. This is reflected in the observed increased power spectral density near the edges of the band in Fig. 2.3. This will occur even when higher terms in the series are present, because the derivative $\partial f/\partial x$ must vanish at the sample edges and any interior extrema.

### 2.4.2 Simulation

Analytically extending the above model to a 2D or 3D geometry, including longitudinal phase slip, is difficult. However, such a model is readily solved numerically, following a procedure

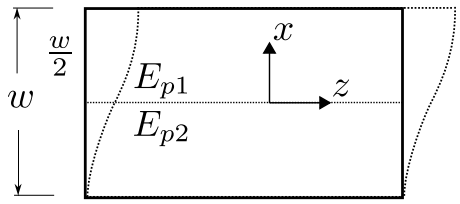


Figure 2.20: Geometry for shear simulation. The sample has a single thickness step at $x = 0$, resulting in two different pinning fields $E_{p_1} - E_{p_2} = \Delta E_p$. The dashed line shows the equilibrium phase profile of the CDW (not to scale).

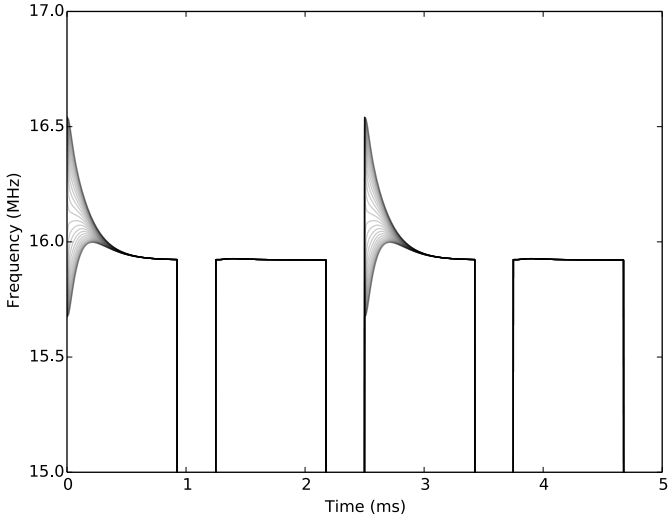


Figure 2.21: Simulation of Eq. 2.21, using the same parameters and bias current profile as in Fig. 2.3. Sliding velocities are plotted for 30 uniformly spaced positions across the width of the sample.

similar to that outlined in Ref. [4], which we generalize here to the 2D case:[3]

$$\frac{\partial\theta}{\partial t} = \left(\frac{Q}{en_c}\right)\frac{1}{\rho_c+\rho_p}\left[\rho_s j_{\rm tot} - E_p + \frac{Q}{en_c}\left(K_x\frac{\partial^2\theta}{\partial x^2} + K_z\frac{\partial^2\theta}{\partial z^2}\right)\right] - \int_{-\infty}^{z} r_{\rm ps}[\theta(x,z',t)]\,dz' \tag{2.21}$$

where $\theta(x,z,t)$ is a renumbered phase, $j_{\rm tot}$ is the total sample current density, and $r_{\rm ps}$ is the phase slip rate. The constants $K_x$, $K_z$, $\rho_c$ and $\rho_s$ are as above, and $E_p$ is computed from the $I-V$ characteristic according to $E_p(j_c) = \rho_s j_{\rm tot} - (\rho_c+\rho_s)j_c$. The correct form of the phase slip rate is unknown, but the distribution of strain in short samples is not especially sensitive to the phase slip mechanism [16]. Here, as in Ref. [4], we use the form

$$|r_{\rm ps}| = r_0 \exp\left(-\frac{t_{\rm ps}}{|\partial\theta/\partial z|}\right),$$

where $r_0 \approx 1.0\times10^{11}\,{\rm m}^{-1}\,{\rm s}^{-1}$ is an attempt rate and $t_{\rm ps} \sim 1.0\times10^{7}\,{\rm m}^{-1}$ is related to the barrier height; both were determined from fits to the data. Figure 2.21 shows the results obtained from integrating the above equation of motion, using the geometry shown in Fig. 2.20 (i.e. a sample with a single thickness step and a $\Delta E_p$ given by Eq. 2.20), and using the same bias current profile as shown in Fig. 2.3. The simulation quantitatively reproduces the observed initial peak splitting and subsequent convergence, along with the overall transient excess velocity.

### 2.4.3 Undershoot, overshoot and relaxation

The simple model above fails to account for two key experimental features: First, there is a marked asymmetry with respect to the bias current direction, particularly for the pulses which reverse the sliding direction. We discuss possible explanations below.

[3] The sample 1 width/thickness ratio is approximately 170, so we neglect variation in the thickness direction.

Second, in response to a repeated pulse of the *same* sign as the previous one (which we will call unipolar), the sample exhibits a transient *increase* of the sliding velocity towards its steady-state value; i.e. an "undershoot". This phenomenon, first observed in measurements of the total sample current [30], cannot be ascribed to elastic relaxation, because any relaxation of the longitudinal strain from its steady-state configuration should produce a transient *overshoot*, as observed in response to current reversals. That is, in the sliding state, the elastic strain opposes the CDW motion, so a reduction in that strain from its equilibrium value should increase the CDW's sliding velocity. Adding elastic relaxation in the "pinned" state to the model defined by Eq. 2.21 indeed produces an overshoot for both unipolar and opposite pulses.

A possible explanation is the relaxation or collapse of dislocation loops. If phase slip is limited by growth, rather than nucleation, of dislocations; if dislocations are generated by the motion of the CDW; and if some of the dislocations collapse or recombine in the pinned state, then the observed unipolar transient could reflect an increase in the concentration of dislocation loops towards its steady-state value. A similar mechanism has been proposed by Gill [36] to account for the low-temperature creep and switching observed in $NbSe_3$.

Glassy relaxation of CDWs has been studied extensively [1, 9, 10, 25, 32, 42, 49, 51, 64, 65, 71, 72, 97, 105, 109, 111]; however, the present work represents the first *direct* measurement of the transient condensate motion after relaxation. Furthermore, theoretical work to date [1, 32, 49, 51, 105] has ignored the effects of dislocations. The data in section 2.3.4 suggest that there are at least two relaxation processes, with different timescales. One is likely the relaxation of elastic strain. In the bipolar case, this strain produces an initial overshoot in the sliding frequency. As the strain relaxes over the rest intervals, the magnitude of this overshoot decreases (Fig. 2.10). Again, however, this cannot be responsible for the undershoot observed in both the unipolar case and for long relaxation times in the bipolar case. The time scale for the collapse of dislocation loops might reasonably be expected to differ from that for elastic relaxation.

We mention in passing two other potential mechanisms for slow relaxation: creep of the CDW region beyond the current contacts [4], and the diffusion of mobile impurities [34]. However, it is unclear how these would result in the observed behavior.

### 2.4.4 Phase slip and the onset of plasticity

We consider possible mechanisms for the CDW's loss of coherence at the near-contact pair in Figs. 2.4 and 2.5. The incoherent signal appears to be the steady state response, which implies that there is plastic slip in the steady state, and only the initial transient is elastic. Thus, we interpret the response as a transition from elastic to plastic behavior: at approximately 250 µs after the start of the pulse, an elastic limit is exceeded, and slip begins.

Shear slip alone seems unlikely to be responsible, for the following reasons: First, sample 2 is relatively narrow (9 µm), so according to the above analysis, the time constant for transverse shear evolution should be very short: scaling sample 1's time constant by the squared ratio of the widths gives $\tau_s \approx 3\,\mu s$, far shorter than the observed 250 µs elastic transient. Second, when the current is reversed, built-up shear strains act in a direction which *increases* the transient shear; here, the reverse happens. Third, the contact pair only 50 µm away, at pair 1, shows no shear at all; nor do pairs closer to the middle of the sample.

However, at low temperatures, longitudinal phase slip has been observed up to hundreds of micrometers from the current contacts [46]. Phase slip occurring within a contact pair produces a velocity gradient and should therefore broaden the washboard frequency peak; additionally, the drop in frequency at pair 2, but not pair 1, could be explained by phase slip in the region between the two. The initial peak frequency $f_0 \approx 1.6\,\mathrm{MHz}$, the time $\Delta t \approx 250\,\mu s$ before the onset of slip, and the distance $l = 1000\,\mu m$ between current contacts yield an estimate of the maximum longitudinal strain:

$$\epsilon \approx \frac{2\pi f_0(\Delta t)}{Ql} = 6 \times 10^{-4}. \tag{2.22}$$

This is in good agreement with the $\epsilon \approx 5 \times 10^{-4}$ found by X-ray diffraction measurements [16, 85] under similar conditions ($I/I_T = 1.5$, $T = 90\,\mathrm{K}$ at a distance of $100\,\mu\mathrm{m}$ from the positive current contact). This has been interpreted [16] as the strain required to depin the dislocation loops responsible for current conversion.

Both X-ray [16] and transport measurements [46] have found that phase slip region near the phase removal contact is smaller than that at the phase injection contact. The cause of this asymmetry is unknown, but it is consistent with the present results: if the region of significant phase slip does not extend as far as the first voltage contact pair, the peak measured there should remain sharp, as it does for the pulse in which the CDW slides toward the near current contact.

The temperature dependence is also in agreement with this picture. At higher temperatures, the region of phase slip becomes much narrower [46], which explains why no peak breakup is observed at $T = 100\,\mathrm{K}$ or above (Fig. 2.6).

The large difference in the steady state frequencies at pairs 1 and 2 implies that there must be a region of sharply concentrated phase slip in the $50\,\mu\mathrm{m}$ length between the contact pairs. Simple models [2, 16] predict a smooth variation of phase slip with position. However, longitudinal splitting into well-defined velocity-coherent domains has been observed in thermal gradient experiments [52, 69, 80, 106]; the field gradient near a contact might play a similar role. Additionally this sample might have a macroscopic defect (such as a grain boundary) in the region between the contact pairs, which would lead to concentrated phase slip.

### 2.4.5 Asymmetry

A common feature of these spatially resolved measurements is the asymmetry with respect to current direction, which appears to have its origin in an asymmetry of the rates of current conversion. No complete theoretical explanation for this has yet been proposed. However, there are three possible mechanisms: (i), asymmetry in the rate of nucleation of dislocation

loops; (ii), asymmetry in the rate of growth of dislocation loops; or (iii), convection of dislocation loops towards the region of phase removal: That is, dislocation loops generated in the bulk, perhaps by the motion of the CDW itself [16], are swept towards the phase removal contact, resulting in a higher concentration of dislocations, and therefore faster equilibration of CDW strain, compared to the region near the injection contact.

### 2.4.6 Conclusions

The experiments listed here represent a small sampling of the types of measurements which are possible with high-performance differential cryogenic amplifiers, which enable observations of CDW dynamics across both time and length. This unprecedented combination of temporal and spatial resolution can provide insight into nearly every aspect of CDW physics. In particular, the measurements reported here illustrate the importance of dislocations and plasticity, for which theoretical understanding is still limited.

Finally, an early question in CDW transport studies was whether the coherent voltage oscillations are generated primarily in the bulk [52, 69, 112], or at the current contacts [80, 95, 106]. Our measurements unambiguously point toward the former: oscillations are detected between differential pairs far from the contacts, and the frequencies of those oscillations change with position within the *same* sample. However, this does not rule out phase slip as the source of the oscillations; in fact, the dependence of the frequencies on longitudinal position suggests that inhomogeneous phase slip occurs at many locations throughout a typical sample.

## 2.5 Appendix 1: Samples

| No. | Length (µm) | Width (µm) | Thickness (µm) | Mounted Date |
|---|---|---|---|---|
| 1 | 3000 | 72 | 0.43 | 08-27 |
| 2 | 1000 | 9 | 0.36 | 09-04 |
| 3 | 1800 | 14 | 0.5 | 06-24 |
| 4 | 1800 | 23 | 0.39 | 04-23 |

# Chapter 3

# Steady-State Response

## 3.1 Introduction

The differential amplifiers reported above make it possible, for the first time, to directly measure the CDW sliding velocity as a function of position along the sample length. Using the same experimental configurations as in the previous chapter, we examine the steady-state spatial dependence and position-position correlations of the $T_{p_1}$ charge-density wave in $NbSe_3$, and particularly of the narrowband voltage oscillations (narrowband "noise", NBN) generated at the washboard frequency of the sliding CDW.

Previous measurements have examined low-frequency noise [7, 11, 13, 55], NBN fluctuations over the entire sample [8, 12] and low-frequency voltage-voltage correlations [47], but, for reasons outlined in the previous chapter, have been limited in bandwidth to approximately 1 MHz.

## 3.2 Methods

The sample preparation methods and measurement techniques described in the previous chapter were again used here, with one significant addition.

Measurements of the fluctuation of the NBN peaks over long time intervals present a

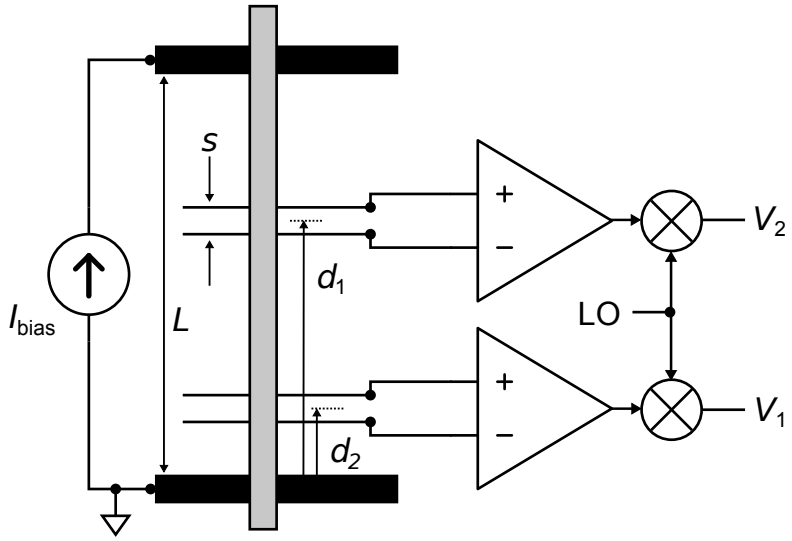


Figure 3.1: Sample contacts, differential amplifiers, and RF mixers used for long-time fluctuation and correlation measurements.

particular challenge. The presence of significant harmonic content and external noise make it necessary to oversample the NBN oscillations by a factor of 5 to 10 to obtain accurate reconstructions. Thus, tracking a 50 MHz peak requires a sampling rate of at least 500 MHz. The number of samples generated in measuring fluctuations over times on the order of a second quickly becomes prohibitive.

To avoid this problem, we use an RF mixer to heterodyne the NBN down to a lower beat frequency, where it is low-pass filtered. A local oscillator is tuned to a frequency approximately 300 kHz below that of the NBN peak, and is mixed with the output from the differential amplifiers. For the highly coherent samples used here, the peak quality factors are on the order of at least several hundred, so even at $f_{NBN} = 50\,\text{MHz}$, the peaks fit comfortably into a 1 MHz digitizer bandwidth. Figure 3.1 shows the amplifier and mixer circuits.

Two quantities are useful for comparing fluctuations at different positions. First is the

normalized cross-correlation:

$$C_{\Delta t}[x,y] = \frac{\langle x(t+\Delta t)y(t)\rangle - \langle x\rangle\langle y\rangle}{\sqrt{\langle x^2\rangle - \langle x\rangle^2}\sqrt{\langle y^2\rangle - \langle y\rangle^2}} \tag{3.1}$$

where $x(t)$ and $y(t)$ are functions of time, and $\langle\cdot\rangle$ denotes a time average.

Second is the spectral coherence, defined as

$$C_{xy}(f) = \frac{|S_{xy}(f)|^2}{S_{xx}(f)S_{yy}(f)} \tag{3.2}$$

where $S_{xy}(f)$ is the cross-spectral density, and $S_{xx}(f)$ and $S_{yy}(f)$ are the auto-spectral densities of signals $x$ and $y$, respectively. Note that $0 \leq C_{xy} \leq 1$, with $C_{xy} = 1$ for perfectly coherent signals.

## 3.3 Results

### 3.3.1 Voltage-voltage correlations

Previous work [47] has examined the voltage-voltage correlations at low frequencies $f < 10\,\text{kHz}$. We have verified these measurements and extended them to higher frequencies.

Figure 3.2 shows the equal-time voltage-voltage correlation between contact pairs separated by 50 µm, as a function of bias field and measurement bandwidth. As observed in Ref. [47], the correlation is greatest just above the threshold, and decreases with increasing bias. The correlation is much weaker at high temperatures.

Additionally, the present high-bandwidth measurements show that these voltage fluctuations are correlated only at low frequencies. Increasing the measurement bandwidth (limited by a digital low-pass filter) decreases the measured correlation coefficient, because the voltage fluctuations are increasingly dominated by uncorrelated high-frequency noise (generated by the CDW motion; the noise floor of the amplifier was at least two orders of magnitude less than the CDW noise in these measurements). Figure 3.3 makes this clear. The spectral

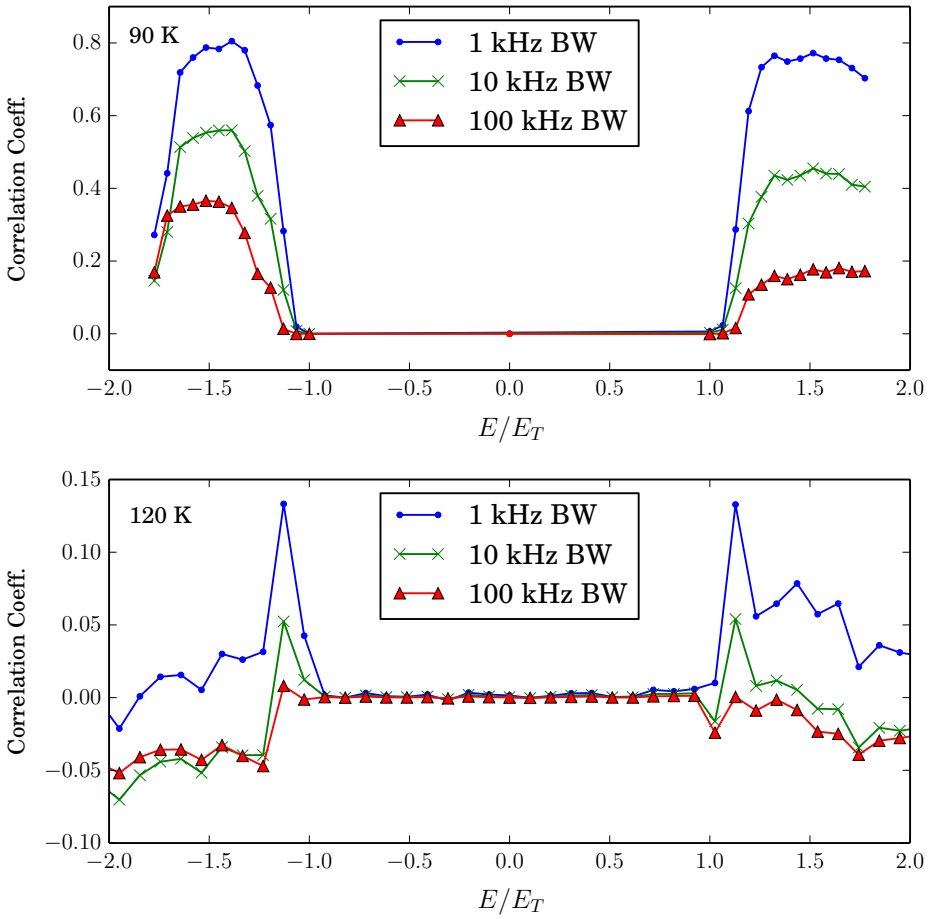


Figure 3.2: Equal-time correlation coefficient $C_0$ of voltage oscillations (not heterodyned) at contact pairs separated by 50 µm, as a function of bias field $E/E_T$ (where $E_T$ is the threshold for CDW conduction) and measurement bandwidth. Sample 5.

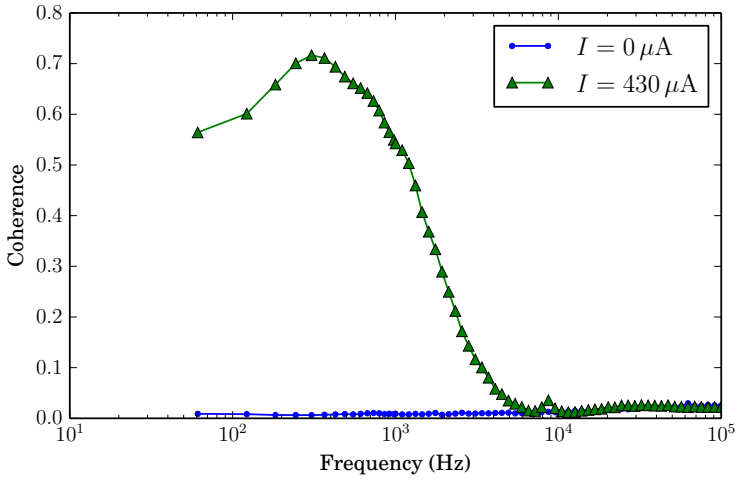


Figure 3.3: Spectral coherence between voltage oscillations at contact pairs separated by 50 µm, for zero bias current and for $I = 1.4I_T$. Sample 5, $T = 90$ K.

coherence between the contact pairs drops off sharply above 10 kHz (which, coincidentally, was the measurement bandwidth in Ref. [47]).

This is not surprising. The high-frequency voltage-voltage correlation should be related to the CDW phase-phase correlation, which decays on a length scale on the order of 1 µm [21], much shorter than the contact spacings here.

However, high-quality samples do exhibit weak long-range correlations at the narrowband oscillation frequency. Figure 3.4 shows the correlation coefficient between contact pairs separated by 900 µm, over the full amplifier (-3 dB) bandwidth of 60 MHz. The sample bias current was adjusted to maintain a NBN peak frequency of 49 MHz at all temperatures. To improve estimates of the small correlation coefficients, averages were taken over multiple successive traces; these also permitted bootstrap estimates of confidence intervals for a null correlation coefficient (by calculating correlations between different-time traces). Small but significant correlations appear sporadically at low temperatures; these may signify intermittent long-range locking or synchronization between regions of the CDW.

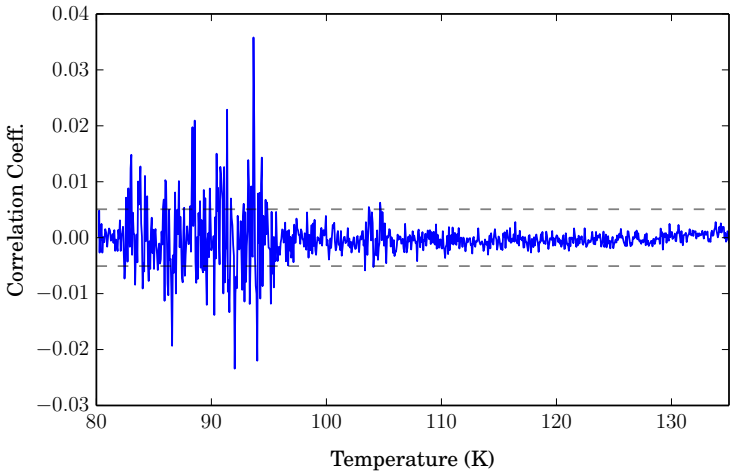


Figure 3.4: Equal-time correlation coefficient $C_0$, over a 60 MHz bandwidth, between contact pairs separated by 900 µm. The sample bias current was adjusted to maintain a NBN peak frequency of 49 MHz as the temperature was increased. The dashed lines are 90% significance levels for a nonzero $C_0$, as estimated via a bootstrapping procedure. A negative coefficient indicates a phase reversal.

### 3.3.2 Velocity fluctuations at a single contact

In all samples observed, the frequency of the NBN peak fluctuates with time (Fig. 3.5); this is most apparent for highly coherent samples with sharp NBN peaks. Using the heterodyne technique described above, the NBN voltage oscillations were recorded for 200 intervals of 1 s, over a total time of 2611 s. For each segment, the spectrogram of the signal was computed, and the peak frequency $f_p(t)$ found at 0.8 ms intervals. The power spectrum of the peak frequencies (a type of "second spectrum" [107]) was computed. This procedure allowed the frequency-dependence of the fluctuation sizes to be measured over five decades of frequency. The gap in frequencies in Fig. 3.6 is an artifact of the way the data were collected: the time required to read the data from the oscilloscope resulted in a delay between successive measurement windows.

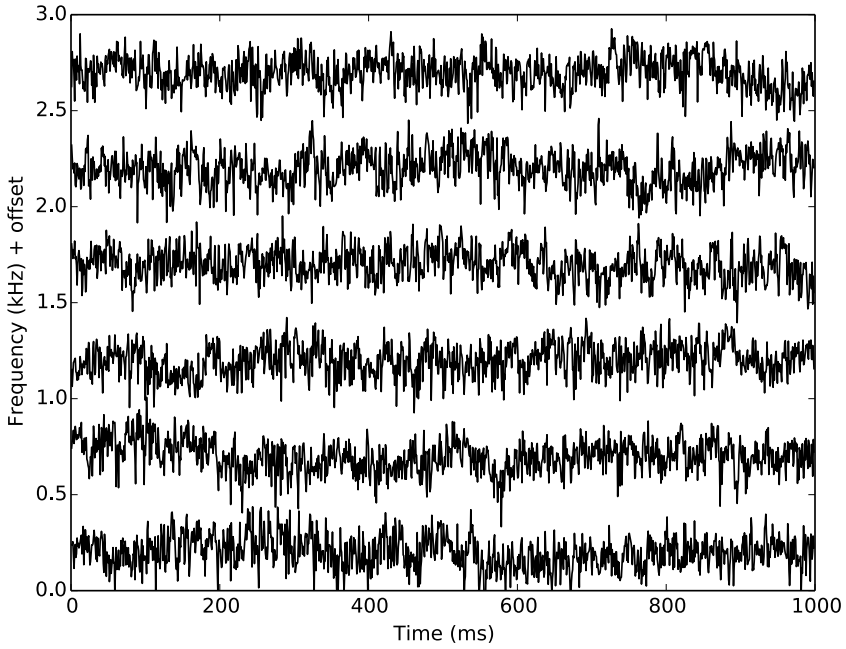


Figure 3.5: Fluctuations of the NBN peak, heterodyned with a 5 MHz LO frequency, at a contact pair near the middle of the sample (500 µm from the nearest current contact). Successive traces are offset for clarity. The width of the peak was significantly smaller than the magnitude of the fluctuations. Sample 2, $T = 80\,\mathrm{K}$.

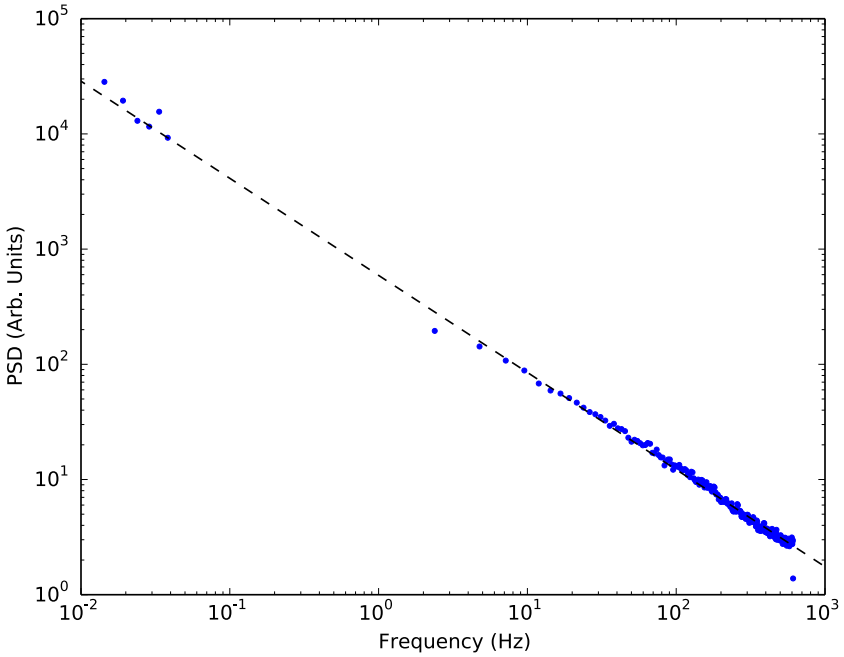


Figure 3.6: Power spectral density of the fluctuations of the NBN peak as shown in Fig. 3.5. The dashed line shows a fit $S(f) \sim f^{-\alpha}$ with $\alpha = 0.84$. Sample 2, $T = 80\,\mathrm{K}$.

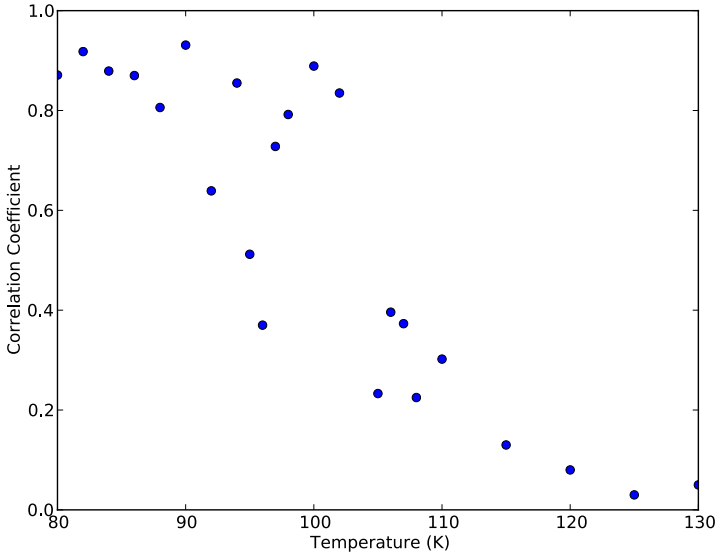


Figure 3.7: Frequency-frequency correlation coefficient vs. temperature of the NBN peak frequency fluctuations between two contact pairs separated by 400 µm. The bias current was adjusted to maintain the NBN peak frequency at 5.6 MHz. Sample 2.

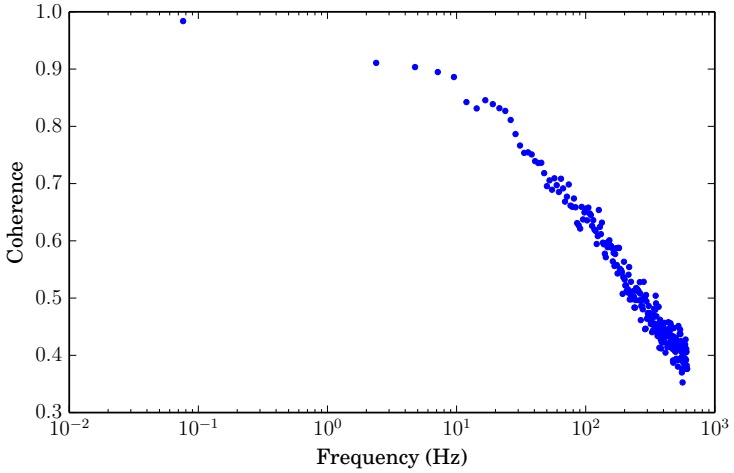


Figure 3.8: Coherence of velocity fluctuations at two contact pairs separated by 400 µm. Sample 2, $T = 80$ K.

### 3.3.3 Velocity fluctuation correlations

As pointed out above, the high-frequency voltage-voltage correlations decay rapidly with distance; furthermore, the voltage does not give direct access to any fundamental state variable of the CDW. However, the high-bandwidth differential amplifiers employed here enable correlation measurements of the fluctuations of the CDW *velocity*, via the NBN peak frequencies.

Using the configuration shown in Fig. 3.1 the NBN peak frequency at each of two contact pairs, separated by 400 µm, was computed from a spectrogram of the heterodyned NBN voltage oscillation signal. The sample was DC-biased to a mean NBN peak frequency of 5.6 MHz. Figure 3.7 shows the correlation coefficient

$$r^2 = \frac{\langle [(f_1 - \overline{f_1})(f_2 - \overline{f_2})) \rangle}{\sigma_{f_1} \sigma_{f_2}} \tag{3.3}$$

where $f_1$ and $f_2$ are the frequencies at pair 1 and pair 2, $\langle \cdot \rangle$ is a time average, and $\sigma_{f_i}$ is the standard deviation, at temperatures from 80 K to 130 K. There is a large amount of scatter, but the general trend is from nearly perfect correlation at 80 K to zero correlation above 130 K. All samples observed showed a relatively sharp drop in correlation in the vicinity of

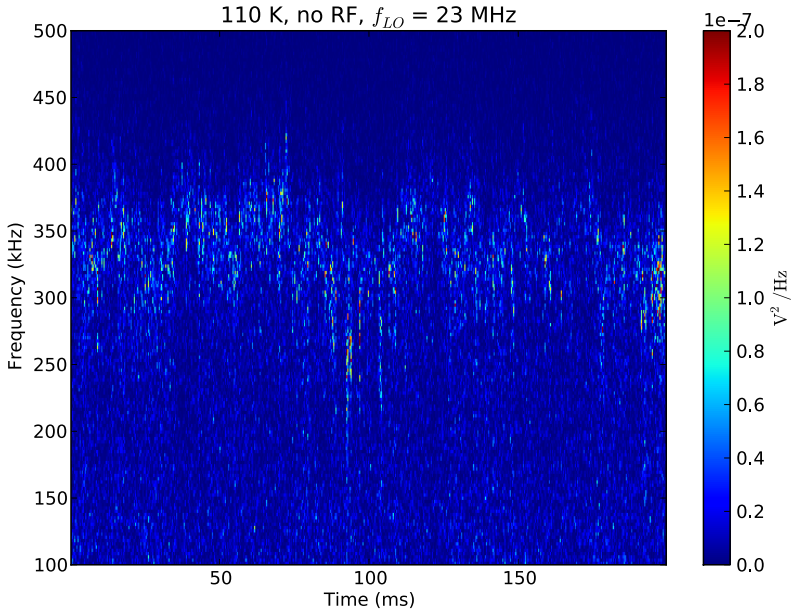


Figure 3.9: Spectrogram of NBN peak fluctuations at a contact pair near the middle of a sample. The NBN oscillations have been heterodyned with a 23 MHz local oscillator signal. Sample 2, $T = 110$ K.

100 K.

### 3.3.4 Mode locking

Previous measurements have found that mode locking to an external AC bias current suppresses the low-frequency broadband noise (BBN) [90] and reduces the width of the NBN peak [8, 104]. These measurements were performed on entire samples and were not time-resolved. Here, we track the NBN peak frequency at a particular location on the sample, far from the current contacts, over a time of 200 ms. Figure 3.9 shows the single-trace spectrogram of the NBN fluctuations at a contact pair near the middle of the sample, DC-biased at approximately $4I_T$. The NBN peak has a width of approximately 90 kHz and shows fluctuations of $\sim 100$ kHz on all resolved time scales (1 ms to 200 ms).

In Fig. 3.10, a 4.65 MHz, 150 mVRMS AC bias has been applied to the sample, and the DC bias has been adjusted to lock the CDW onto the fifth harmonic of the AC drive. The AC bias was lowpass-filtered to reduce the amplitude of its fifth harmonic below 90 dB,

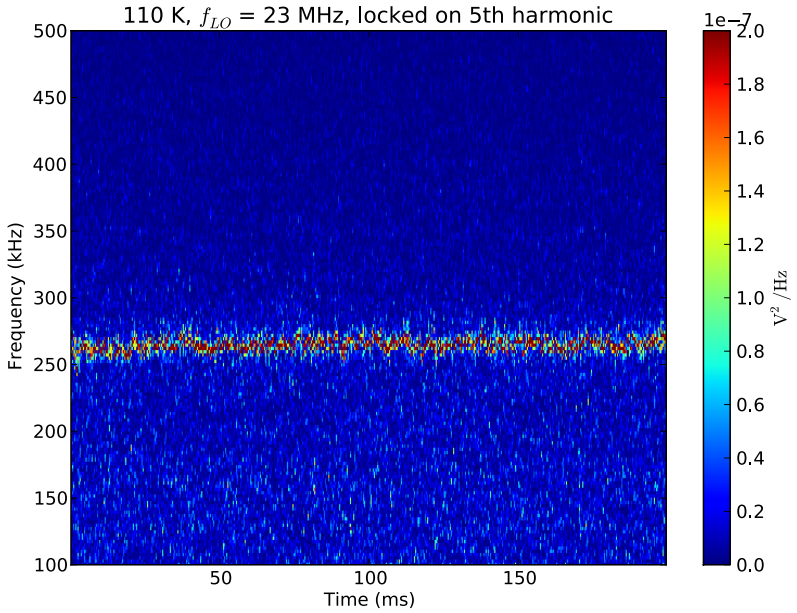


Figure 3.10: Spectrogram of the same sample as in figure 3.9, now mode-locked to the fifth harmonic of a 4.65 MHz, 150 mVRMS AC bias.

ensuring that the measured signal was dominated by the voltage oscillations associated with the CDW. The width of the NBN peak in the mode-locked CDW approaches the resolution of the measurement, and the fluctuations are reduced to $\sim 20$ kHz, but are not completely eliminated.

### 3.3.5 Condensate density

The effective condensate (number) density $n_{\text{eff}}$ can be estimated from the ratio of the CDW current $i_c$ to the NBN peak frequency $f$:

$$n_{\text{eff}} = \frac{i_c}{\lambda A e f} \tag{3.4}$$

where $\lambda = 1.44$ nm is the CDW wavelength, $A$ is the sample cross-sectional area and $e$ is the elementary charge. Figure 3.11 shows one such estimate, as a function of temperature. As the sample was warmed from 80 K to 140 K, the bias current was adjusted via a feedback

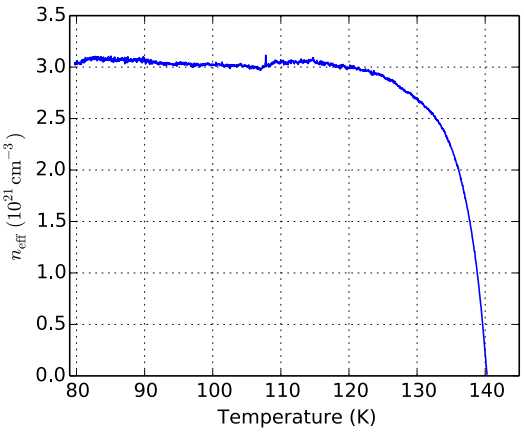


Figure 3.11: Effective condensate density $n_{\mathrm{eff}}$ vs. temperature, as determined from the ratio of the NBN peak frequency to the CDW current. Sample 1.

loop to maintain a constant NBN peak frequency of $f = 10.3\,\mathrm{MHz}$. The CDW current $i_c$ was determined from a four-probe voltage and the independently measured normal resistance vs. temperature: $i_c = i_{\mathrm{tot}} - V/R_n(T)$. The condensate-density–temperature relationship differs qualitatively from that measured previously [58]: rather than decreasing for temperatures below 90 K, the condensate density in the present measurement appears to saturate. The reason for the discrepancy is unclear. However, the relationship reported here does resemble the $T_{p_2}$ behavior reported in Ref. [58].

### 3.3.6 Coherence vs. temperature

Sample 1 showed an exceptionally coherent response at low temperatures. Figure 3.12 shows a spectrum recorded at a contact pair far from the current contacts, at 85 K. There is a single, sharp peak (plus its harmonics); the measured peak width was limited by the FFT resolution, but the quality factor is at least 1000.

At higher temperatures, however, the CDW in this sample appeared to break up progressively into smaller domains. Figure 3.13 plots the power spectral density at two contact pairs, over a temperature range from 80 K to 142 K. The sample was warmed at a rate of 0.5 K/min, and spectra were recorded continuously. The bias current was a constant 6.5 mA.

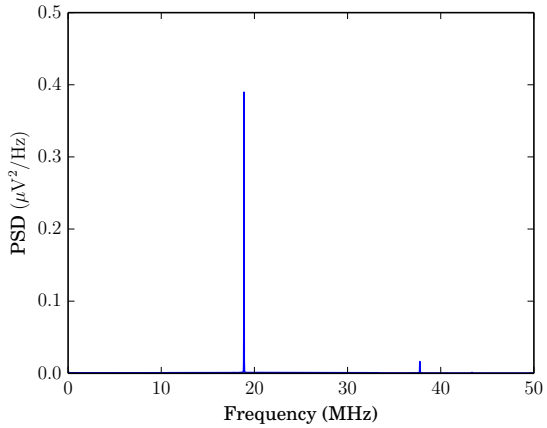


Figure 3.12: Spectrum of voltage oscillations at a contact pair located at $d = 1100\,\mu\text{m}$ from the negative current contact (the total sample length was $3000\,\mu\text{m}$). The sample was DC-biased with $I = 3.00\,\text{mA}$. Sample 1, $T = 85\,\text{K}$.

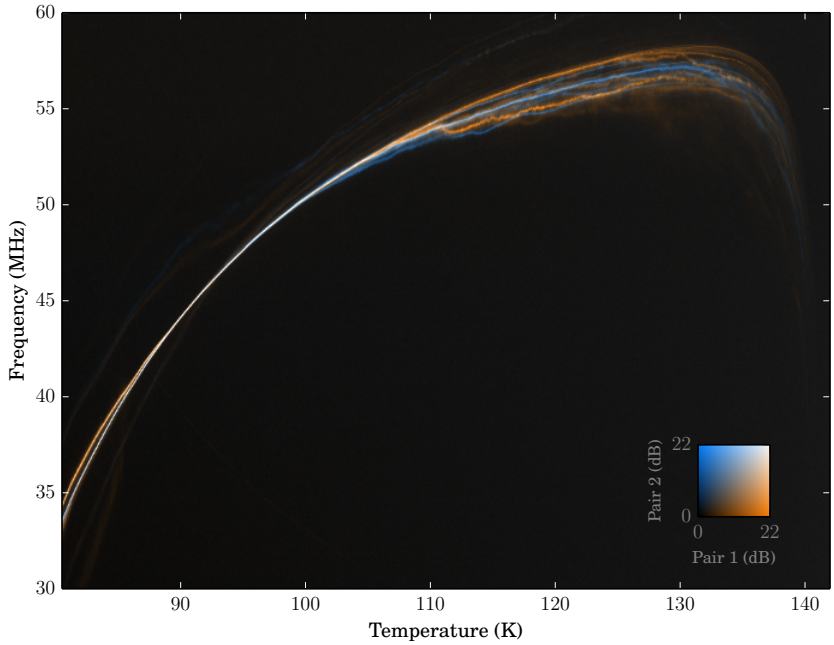


Figure 3.13: Power spectral density vs. temperature at a constant current bias of $I_T = 6.5\,\text{mA}$. Spectra were recorded at pair 1 (orange), located at $d = 1900\,\mu\text{m}$, and pair 2 (blue), located at $d = 1000\,\mu\text{m}$. The spacing for both pairs was $50\,\mu\text{m}$. Sample 1.

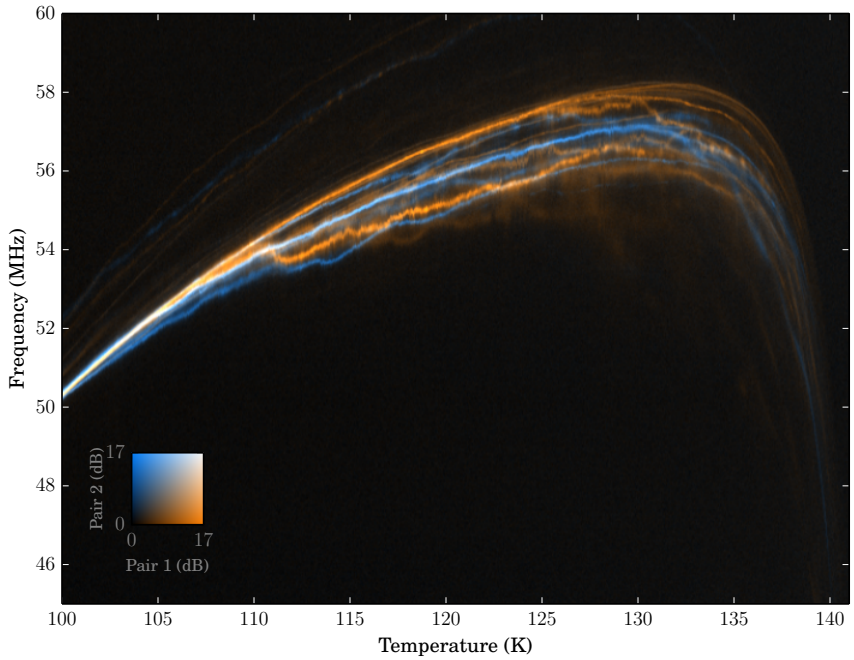


Figure 3.14: Inset of the high-temperature portion of Fig. 3.13

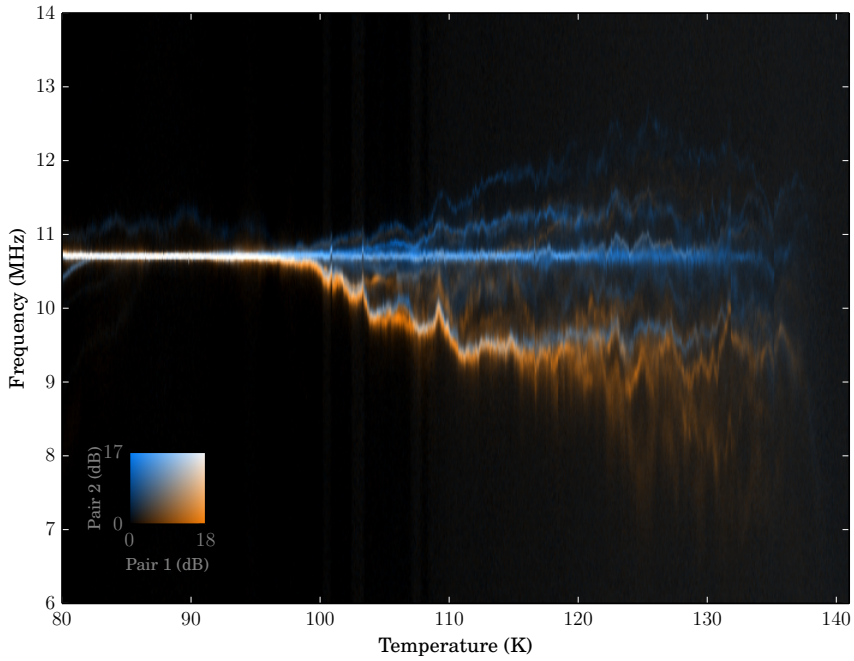


Figure 3.15: Power spectral density vs. temperature, with bias current adjusted to maintain a constant washboard frequency at pair 2. Spectra were recorded at pair 1 (orange), located at $d = 1100\,\mu\text{m}$, and pair 2 (blue), located at $d = 1000\,\mu\text{m}$. The spacing for both pairs was $50\,\mu\text{m}$. Sample 1.

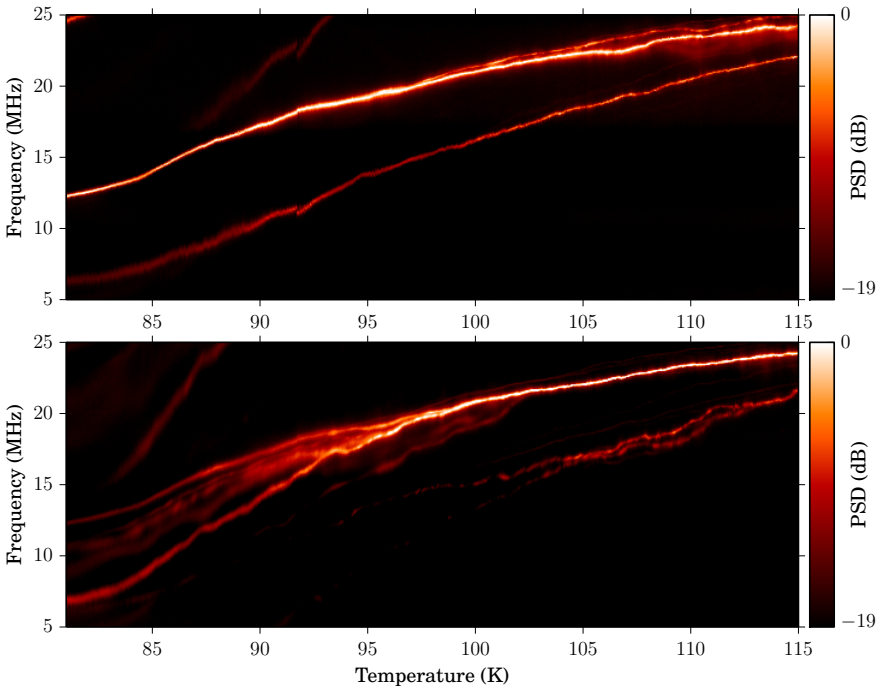


Figure 3.16: Power spectral density vs. temperature at a constant current bias of $I_T = 250\,\mu A$. Top panel: contact pair in center of sample (total sample length 1000 µm). Bottom panel: contact pair 75 µm from negative current contact. The spacing for both pairs was $s = 50\,\mu m$. Harmonics of the fundamental are visible in the upper right, and a small shear domain appears in the lower part of the images. Sample 2.

Figure 3.14 shows a closer view of the high-temperature region where the moving CDW "melts." There is a loss of coherence not only between the contact pairs (which were separated by a distance of 900 µm), but also within the region of the CDW observed by each contact pair (approximately 50 µm long by 72 µm wide).

It might be objected that not only the temperature, but also the sliding velocity varies in the above measurement. Therefore, it was repeated, this time with a constant washboard frequency. The sample was again warmed slowly, but a feedback loop continuously adjusted the bias current to maintain a constant NBN peak frequency at the first contact pair. Figure 3.15 shows the spectra obtained in this way; the behavior is qualitatively similar to that observed in the constant current case.

The above measurements were made with contact pairs far from the current contacts, where phase slip from current conversion is less significant [4, 16]. The region of phase

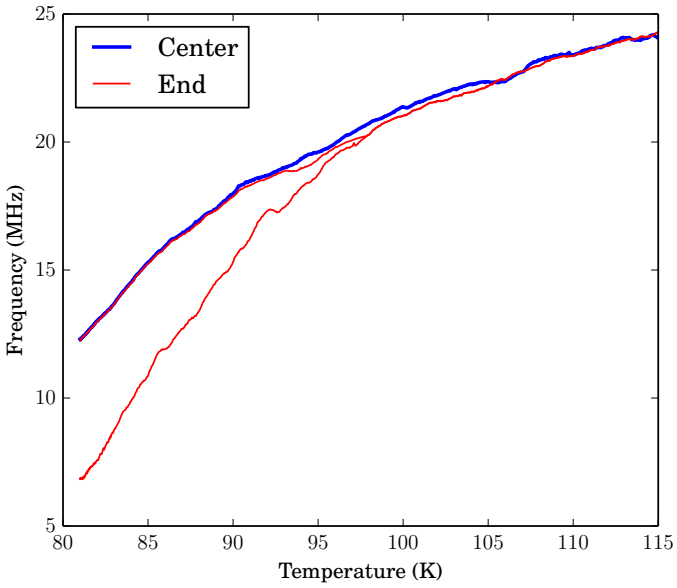


Figure 3.17: Frequencies of the dominant spectral peaks in Fig. 3.16. The peak at the end contact is split below 98 K.

slip near the current contacts is of interest, however, so we made similar measurements on another sample (number 2), with contact pairs close to the current contacts. Figure 3.16 shows spectra for one contact pair located 500 µm from the negative current contact (the CDW was sliding *away* from this contact), and for another contact pair located only 75 µm from the negative current contact. This sample, too, mode-locked completely (at 120 K, RF frequency 15 MHz), but had a small thickness step close to one edge, which generated a shear peak with about 4% of the intensity of the dominant peak.

The main feature of interest, however, is that the main peak of the CDW at the near-contact pair split at temperatures below 98 K, when the CDW was sliding away from the nearby current contact (the peak was not split for the reverse direction of motion). We ascribed a similar feature, reported in the transient measurements in the previous chapter, to phase slip in the region near the current contact.

Figure 3.17 plots the frequencies of the main peaks for both the center contact and the near-end contact. As the temperature decreases below 98 K, the near-end peak splits, with one part becoming coherent with the center-contact peak (i.e. with the motion of the bulk

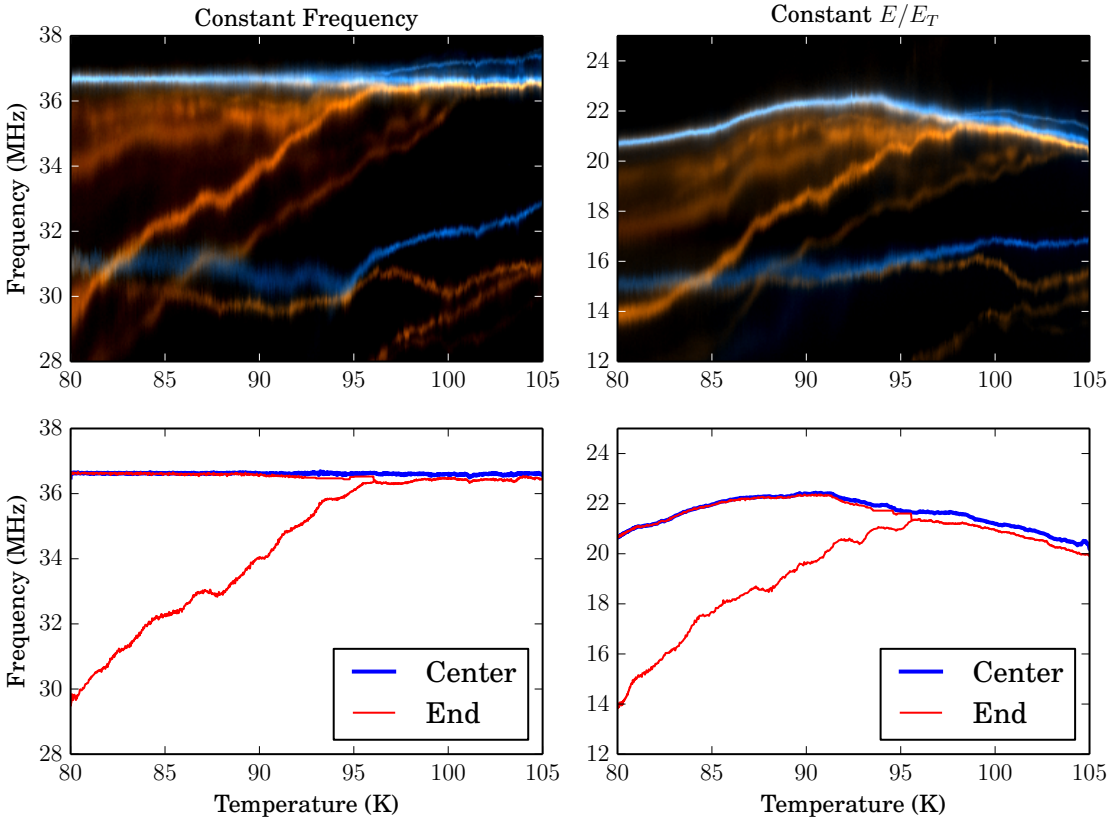


Figure 3.18: Top row: power spectral density at contact pairs at the middle (blue) and near the end (orange) of sample 2 (same locations as in Fig. 3.16). Bottom: Frequencies of the dominant spectral peaks. The data on the left were recorded at a constant NBN peak frequency at the middle pair; the data on the right were recorded with a constant bias field $E/E_T(T)$.

of the CDW), and the other decreasing significantly in frequency compared to the center-contact peak. We note that there is also significant but fairly broad-band spectral power in the region between the split peaks, implying a broad distribution of sliding velocities.

This measurement was repeated with a constant NBN peak frequency maintained at the center contact, and also with a constant ratio of $E/E_T(T)$. For the latter case, the threshold field $E_T(T)$ was measured from independent $dV/dI$ curves over the temperature range of interest. Figure 3.18 shows the results of both of these experiments; they are qualitatively similar.

## 3.4 Conclusions and Future Work

We propose the following tentative picture of the temperature-dependence of the coherence of the $T_{p_1}$ CDW in $NbSe_3$: at low temperatures ($\lesssim 90\,\mathrm{K}$), phase slip extends far from the current contacts. In samples with lengths on the order of a few millimeters (including nearly all the samples reported in the literature), significant longitudinal strain, and therefore phase slip, exists throughout the *entire* sample [16]. The phase slip is not uniformly distributed, however, but is concentrated in the vicinity of lattice defects (which exist in virtually all samples). Thus, the CDW is broken into sample-dependent, longitudinal velocity-coherent regions with abrupt boundaries, as were observed both here (Figs. 3.17 and 3.18) and in Ref. [47].

As the temperature increases, the region of phase slip shrinks toward the current contacts. Far from these, the CDW strain is small, and phase slip is rare. In high-quality samples, the CDW slides uniformly over nearly the entire sample length at temperatures between $\sim 90\,\mathrm{K}$ and $\sim 105\,\mathrm{K}$.

At still higher temperatures, thermal fluctuations begin to break up the CDW. The shear and longitudinal strengths decrease, and sample inhomogeneities increasingly lead to shear and phase slip.[1] The size of velocity-coherent domains decreases, and their number increases,

[1]This is not in contradiction with the observation that most samples show the completest mode locking

until the CDW melts completely at the transition temperature.

The measurements described here were limited in spatial resolution by the number and spacing of the voltage contacts. However, substrates with many more finely-spaced contacts are readily fabricated. Furthermore, we can envision a pair of micro-actuated probes (similar to blunt, conductive AFM tips), which could be positioned anywhere along both dimensions of the sample surface, making it possible to map out the spatial dependence of the CDW velocity, coherence, and phase slip with very high resolution. Combined with the ability to micro- and nanofabricate samples with arbitrary geometries [41, 54, 92], this approach should facilitate a rich array of experiments.

## 3.5 Appendix 1: Samples

| No. | Length (µm) | Width (µm) | Thickness (µm) | Date Mounted |
|---|---|---|---|---|
| 1 | 3000 | 72 | 0.43 | 08-27 |
| 2 | 1000 | 9 | 0.36 | 09-04 |
| 3 | 1800 | 14 | 0.5 | 06-24 |
| 4 | 1800 | 23 | 0.39 | 04-23 |
| 5 | 1000 | 29 | 0.32 | 08-08 |

near 120 K; as we have shown earlier, mode-locking measurements are not directly related to the intrinsic velocity coherence of a sample. Consider, for instance, an extremely long sample, with slight length-wise variations in $E_T$. If its cross-section is reasonably uniform, it will mode lock completely, because the mode-locking plateaus have finite widths. When the sample is DC-biased, however, the CDW sliding velocity will vary along the length.

# Chapter 4

# Other Techniques

This chapter summarizes three experimental techniques which showed promise, but for which only limited data are thus far available. They are included here in the hope that they may serve as the basis for future work.

## 4.1 Ion Gels

It is possible to construct field-effect-transistor (FET)–type devices by using a thin crystal of $NbSe_3$ as the channel, and applying a gate voltage across a dielectric. This results in a modulation of the threshold field $E_T$ for CDW conduction [3] which is surprisingly large, considering the small modulation of the carrier density. A positive gate voltage increases the threshold field, and a negative gate voltage decreases it. No satisfactory explanation of this behavior has yet been proposed, and there has been little experimental work since that of Ref. [3].

The experiments in Ref. [3] used a $SiO_2$ dielectric on a silicon substrate. $NbSe_3$ has a large carrier density ($\sim 3.8 \times 10^{21}\,\mathrm{cm}^{-3}$ [3]) so the carrier density modulation achievable in this way is severely limited by the dielectric strength of the gate insulator and the practical minimum thickness of cleaved $NbSe_3$ crystals. The maximum surface charge density of a capacitor structure with a linear dielectric is $\sigma_{\max} = \epsilon_r \epsilon_0 E_b$, where $\epsilon_r$ is the relative per-

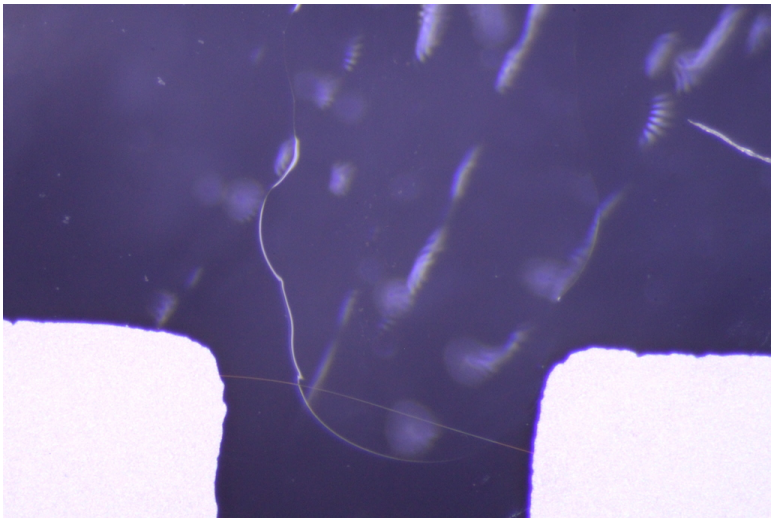

Figure 4.1: Ion gel sample configuration. The $NbSe_3$crystal is the thin, curved horizontal line near the bottom. The white areas in the lower corners are the indium contacts; the clear gel is visible as a patch extending from the top of the image to the region between the contacts. The gate pad is slightly above the pictured region.

mittivity and $E_b$ is the dielectric strength. For $SiO_2$, $\epsilon_r = 3.9$ and $E_b \approx 5 \times 10^8\,\mathrm{V/m}$, so $\sigma_{\max} \approx 1.7\,\mu\mathrm{C/cm^2}$.

The thinnest $NbSe_3$ crystals readily produced by cleaving have thicknesses on the order of 30 µm. The maximum carrier density modulations reported in Ref. [3] were approximately 0.1%. Larger modulations require either thinner crystals (which are difficult to produce and handle), or more exotic gate materials.

One possibility is to use a ferroelectric material, such as lead zirconate titanate (PZT), which can achieve surface charge densities of at least $40\,\mu\mathrm{C/cm^2}$ [57]. Unfortunately, since $NbSe_3$ cannot readily be grown in thin films, it is necessary to manually place small crystals onto the PZT. We attempted to do so with 100 nm and 200 nm thin films atop strontium titanate substrates (grown by Phasis Sàrl), but we found that this inevitably resulted in damage (either mechanical or electrical) and current leakage through the delicate PZT layers. It might be possible to succeed with thicker PZT layers, or with a different sample mounting technique (e.g. coating the PZT with a protective layer of resist, laying a crystal onto the resist, and etching away the resist to allow the crystal to drop).

Ionic liquids are another means of producing large surface charges. The accumulation of

ions at a conducting surface can produce charge densities exceeding 150 μC/cm$^2$ [19]. Ionic liquids have been used to fabricate a variety of field-effect devices [18, 19, 43]. To keep them in place, the liquids are typically mixed with a polymer to form an "ion gel," which can be dissolved in a solvent for ease of application.

We have fabricated $NbSe_3$ field-effect devices using the ionic liquids (N,N-diethyl-N-(2-methoxyethyl)-N-methylammonium bis(trifluoromethylsulphonyl-imide) (DEME-TFSI) and 1-Ethyl-3-methylimidazolium bis(trifluoromethylsulfonyl)imide (EMI-TFSI) mixed with the block copolymer poly(styrene-b-ethylene oxide-b-styrene) (PS-PEO-PS).

Thin crystals of $NbSe_3$ were mechanically cleaved from larger samples. This was most readily accomplished by laying a crystal on a glass substrate, then gently peeling it up with a needle-like tungsten tool. Electrostatic adhesion tended to cleave away long (up to several millimeters), thin strands, which remained stuck to the glass as the parent crystal was lifted away. Applying a drop of isopropanol floated the thin strands and allowed them to be lifted and transferred to a sapphire substrate.

Indium was evaporated through a mask to form contacts to the ends of the crystal, and a third gate contact was evaporated nearby. A drop of a solution of the ion gel in ethyl cellulose was applied across the gate and the crystal. However, it was crucial that the drop did not touch the contact pads, so that the entire gate voltage was dropped across the surface of the sample (the "channel" of the FET). Figure 4.1 depicts this configuration.

The sample was dried under vacuum overnight to eliminate moisture from the gel. A voltage was applied between the gate and the channel at room temperature, to polarize the ionic liquid, and then the sample was cooled to 30 K.

A major drawback of this technique is that, since the ionic liquids freeze well above the Peierls transition temperatures, it was necessary to warm the sample to near room temperature to change the gate voltage. The differential contraction of the ion gel upon cooling often damaged or even severed the $NbSe_3$ crystal. Applying thinner layers of gel reduced, but did not eliminate, this problem. Additionally, the gel appeared to react electrochemically with

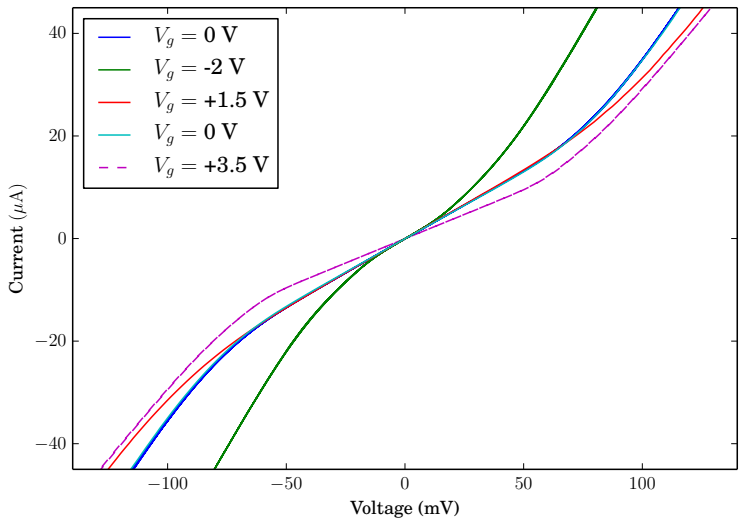


Figure 4.2: Variation of the $I - V$ characteristic of a $0.17\,\mu m^2$ sample, for gate voltages applied in the sequence shown in the legend. The $V_g = 0$ curve was done twice to ensure that the changes were reversible. Applying a gate voltage of 3.5 V, however, damaged the sample, as revealed by the decrease in below-threshold conductivity.

the crystal. If a constant gate voltage was applied at room temperature, the resistance of the sample increased steadily over a timescale of several hours.

These difficulties limited the success of this experiment. Nevertheless, it was possible to achieve modulations of the threshold field comparable to those in Ref. [3], using a crystal that was 12 times thicker, indicating a correspondingly larger surface charge density. Figure 4.2 shows current-voltage characteristics at several gate voltages, applied in the sequence shown the legend. The qualitative behavior and sign of the effect agree with those in Ref. [3]. Returning the gate voltage to zero after the second and third curves reproduced the original $V_g = 0$ curve, suggesting that the changes were not due to sample damage (or, at least, were reversible). On the other hand, later applying a larger gate voltage (3.5 V) *did* damage the crystal, which was reflected in its increased below-threshold resistivity.

The magnitude of the modulation achieved with a relatively thick crystal suggests that this is a potentially promising technique, if the problem of sample damage can be solved. It seems plausible that some combination of ionic liquid, mounting technique, and cooling procedure might accomplish this.

## 4.2 Focused Ion Beam Milling

Naturally defect- and step-free crystals of $NbSe_3$ are extremely rare. Much more common are samples with only a few large thickness steps. It is sometimes possible to cleave away, by hand, a step-free portion [53, 58], but this requires considerable finesse and luck. Another approach is to etch the crystal using standard lithography techniques [75]; however, this is a time-consuming process, involving many steps. Focused ion beam (FIB) milling can pattern crystals quickly and precisely, and has been used to create samples with a variety of geometries [76, 92, 94].

As a test of the FIB milling process, crystal with several thickness steps, and a large step-free portion was selected and mounted on an alumina substrate patterned with an array of 200 nm thick by 2 µm wide gold traces. Wider traces were used as current contacts. The ends of the crystal were affixed with drops of ethyl cellulose dissolved in ethyl acetate.

A nearly step-free portion of the crystal was isolated by milling a channel through the crystal, using an FEI Strata 400 dual-beam SEM FIB at the Cornell Center for Material Research (CCMR). To avoid excessive sample damage, the scanning electron microscope (SEM) beam was used for alignment and imaging. Thin strips of $NbSe_3$ were left at the voltage contacts, to avoid milling through the latter. The entire process took approximately two hours.

Figure 4.4 shows a mode-locking curve for the sample after milling. The CDW locks almost completely at the 1:1 peaks. The lack of perfect mode locking may be due to a small remaining thickness step, which is visible on the left side of the crystal in Fig. 4.3. There is no indication of serious sample damage from the gallium ion bombardment.

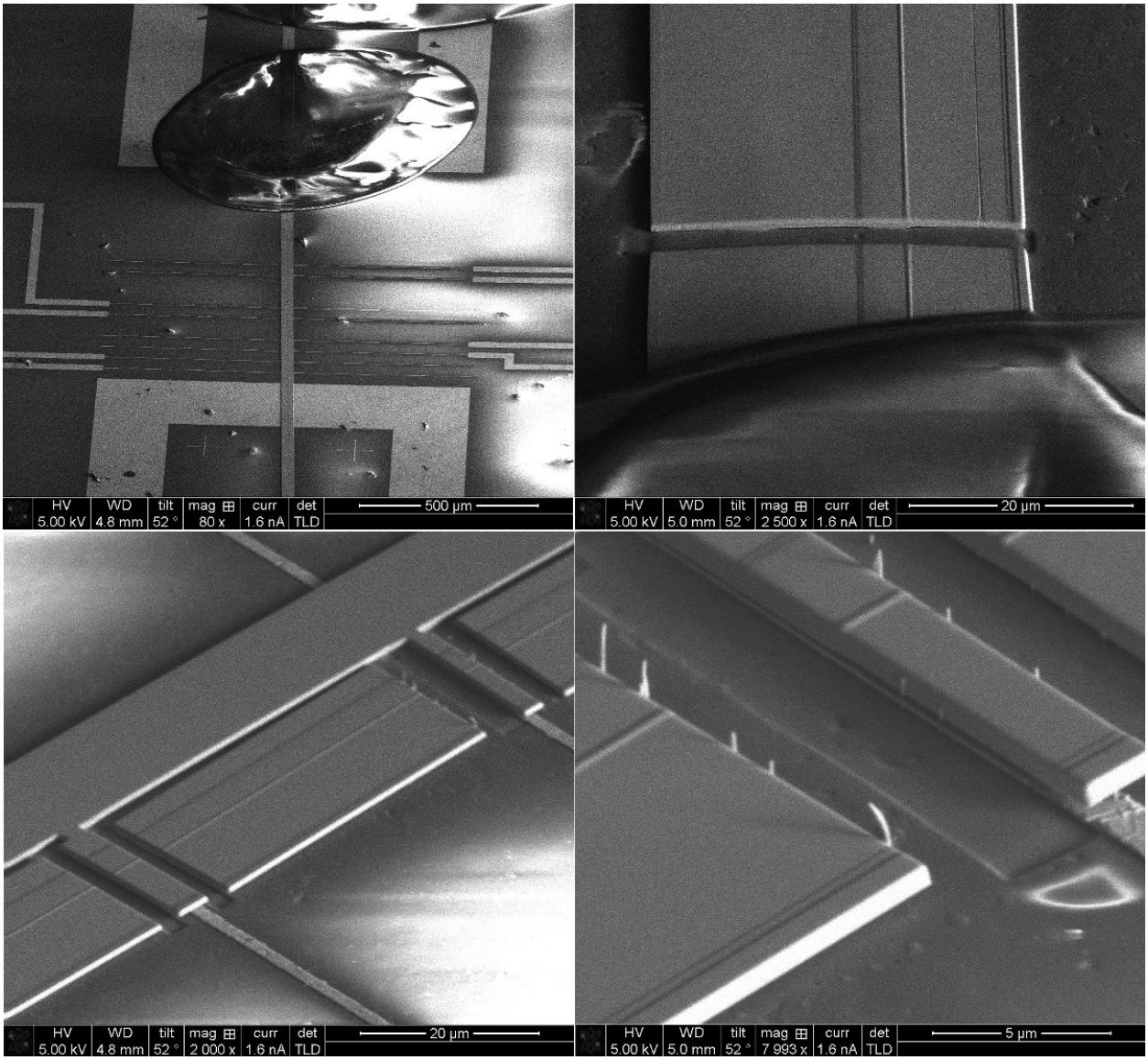


Figure 4.3: SEM images of FIB processing of a $NbSe_3$ crystal. Top left: original crystal (vertical), laid atop gold traces (horizontal). The elliptical object at the top is ethyl cellulose. Top right: cross-section cut through the crystal beyond a current contact, showing the thickness steps. The apparent curvature is distortion due to charging of the ethyl cellulose. Bottom left: crystal after milling. A channel has been cut to isolate the step-free portion; thin strips have been left at the voltage contacts. Bottom right: closeup of one of the voltage contacts, showing that the crystal has curved away from the substrate. Also visible are thin whiskers of $NbSe_3$ cleaved during the milling process.

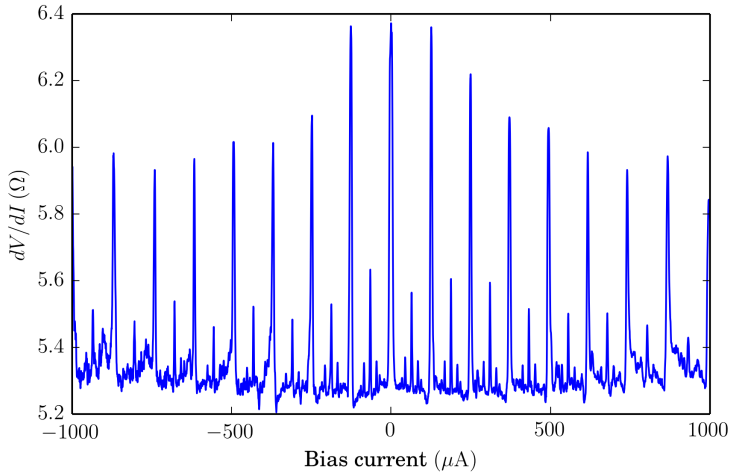


Figure 4.4: Mode-locking of the FIB-milled sample in Fig. 4.3. The sample shows nearly complete locking at the 1:1 peaks. RF bias: 350 mV RMS, 5 MHz. $T = 120$ K.

## 4.3 Pulsed High-Field Measurements

For bias fields well above thresholds, the CDW conductance approaches a limiting value $\sigma_\infty$. The leading correction has been calculated [96] using perturbation theory (in 3D) to be

$$\sigma = \sigma_\infty - cE^{-1/2} \tag{4.1}$$

However, experiments at high fields have instead found $\sigma = \sigma_\infty - cE^{-1}$. [100, 101].

Measuring the $I-V$ characteristic of $NbSe_3$ at more than a few times threshold requires a pulsed technique to avoid heating the sample. It is difficult to simultaneously achieve short pulse times and high precision. A naive experiment measures the total sample current for a set voltage

$$I_{\text{tot}} = V(G_{\text{norm}} + G_\infty - cE^{-\alpha}). \tag{4.2}$$

The quantity of interest, the last term, is a small perturbation riding atop a large signal. Digital storage oscilloscopes can sample at rates well above 1 GS/s, but have limited resolution (typically 8 bits) and linearity. Boxcar integrators offer an alternative method of acquisition,

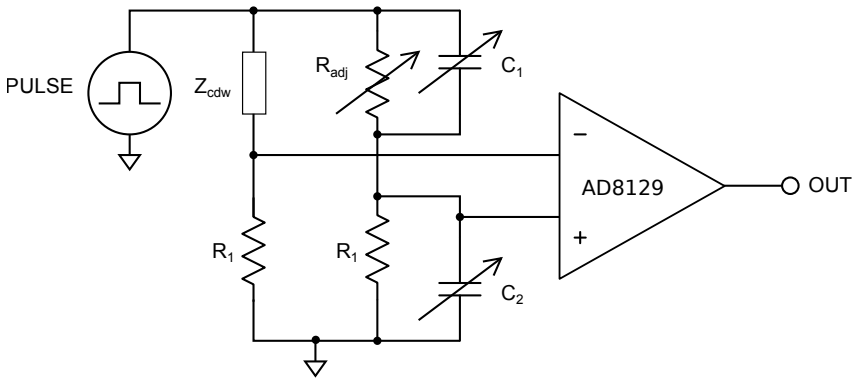


Figure 4.5: Bridge configuration for pulsed measurements of the high-field CDW conductance. $R_{\mathrm{adj}}$, $C_1$, and $C_2$ are adjusted to null the bridge for high fields. The output of the high-speed differential amplifier is digitized by an oscilloscope.

but these, too, suffer from poor accuracy: a leading model from Stanford Research Systems specifies an accuracy of 3%. Therefore, in either case, it is necessary to subtract the large and variable common-mode voltage before digitizing the signal.

A more practical approach is to directly measure the sample conductivity using a bridge configuration. Figure 4.5 shows the measurement configuration. The CDW conductor forms one leg of the bridge. A variable resistor and two variable capacitors adjust the impedances of two other legs to null the bridge voltage (the capacitors are necessary to balance parasitic inductances and capacitances in the cryostat wiring). A high-speed differential amplifier senses and amplifies the bridge voltage; the output from the amplifier is digitized by a high-speed digital oscilloscope. Leads are kept short to minimize ringing artifacts. Pulses as short as 50 ns can be measured.

The bridge is nulled for *high* fields; i.e. to balance a conductance of $G_{\mathrm{norm}}+G_{\infty}$. Thus, the output is proportional to the desired quantity, $cE^{-\alpha}$. This greatly improves the sensitivity and accuracy of the measurement. Figure 4.6 shows data for the $T_{p_1}$ CDW at 120 K, acquired using 100 ns pulses. A fit of Eq. 4.2 to the data gives $\alpha = 0.63$, which is closer to the prediction of Ref. [96]. Further measurements using samples of varying thicknesses should provide insight into the role of dimensionality in the asymptotic behavior.

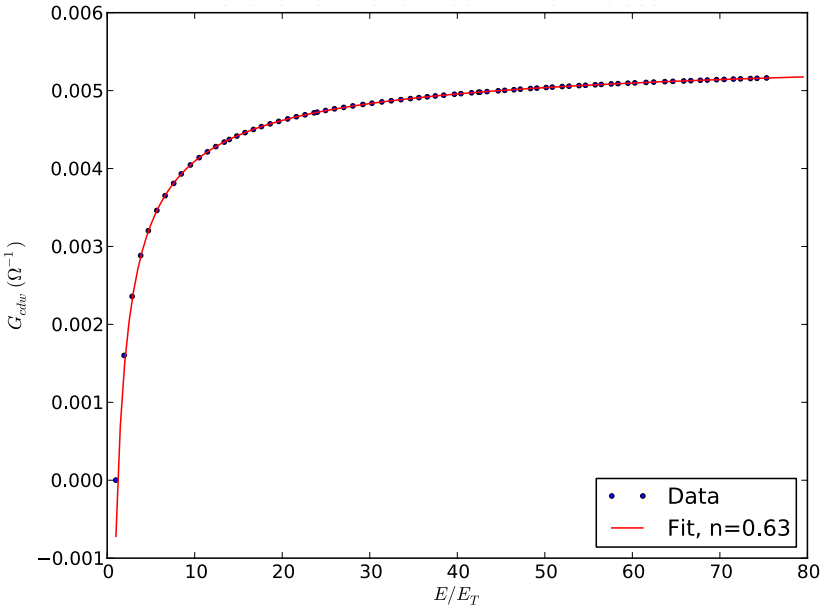


Figure 4.6: Pulsed high-field conductance of a 2 µm thick by 40 µm wide by 3 mm long $NbSe_3$ sample at $T = 120\,\mathrm{K}$, using the configuration in Fig. 4.5 and 100 ns pulses. The dots are measurements, and the line is a fit of Eq. 4.2 with $\alpha = 0.63$.

# Appendices

# Appendix A

# Crystal growth

The procedures for the growth of the $NbSe_3$ crystals used in this work were based on those in [99], but differed slightly. Crystals were grown in ampoules of GE type 214 fused quartz, with 22 mm inner diameter by 25 mm outer diameter by 300 mm long round-bottomed bodies, and 9 mm inner diameter by 11.8 mm outer diameter by 200 mm long necks.

The ampoules were cleaned according to the following procedure. The deionized (DI) water used had a resistivity of at least 17 $M\Omega$ cm.

1. Insides and outsides washed with a detergent (e.g. Alconox®)
2. Filled with DI water and drained, five times; outsides rinsed with DI water
3. Insides and outsides rinsed with acetone, and then isopropanol
4. Rinsed five times with DI water
5. Filled with a 3:9 mixture of 40% hydrofluoric acid : 70% nitric acid
6. Allowed to etch for one hour
7. Rinsed five times with DI water
8. Dehydrated by baking in vacuum of better than $1 \times 10^{-6}$ mbar at 900 °C for 12 hours

| Segment | L | M | R | time (hours) | |
|---|---|---|---|---|---|
| 0 | 0 | 0 | 0 | start | |
| 1 | 380 | 315 | 250 | 4 | warming |
| 2 | 630 | 565 | 500 | 20 | |
| 3 | 715 | 650 | 590 | 6 | |
| 4 | 715 | 650 | 590 | 48 | reverse transport |
| 5 | 605 | 680 | 745 | 8 | |
| 6 | 605 | 680 | 745 | 297 | growth |
| 7 | 0 | 100 | 270 | 14 | cooling |
| 8 | 0 | 0 | 0 | 5 | |

Table A.1: Furnace program for $NbSe_3$ growth. The temperature at each of the left (L), middle (M), and right (R) zones was ramped linearly to the specified temperature (in °C) over the specified time. The starting and ending temperatures were set to 0 °C (to ensure the furnace turned off completely), but the actual temperatures were never lower than ambient ($\approx 20\,°C$).

Ampoules were stored under vacuum until immediately before loading. The Nb source was a fine powder: Alfa Aesar Puratronic 99.99%, stock number 40510, lot A27K15; the Se source was in the form of pellets: Alfa Aesar stock number 00290, lot G13K29.[1] Each ampoule was loaded with 0.56 g Nb and 1.46 g Se. The ampoule was evacuated to a pressure of less than $1 \times 10^{-4}$ mbar, and then was back-filled with oxygen to a pressure of 60 mbar. The neck was sealed with an oxy-hydrogen torch.

Ampoules were placed in a digitally-controlled three-zone tube furnace. The time-temperature profile is listed in Table A.1 and plotted in Fig. A.1. The ampoules were positioned with their bottoms at the right (R) zone, and their tops at the left (L) zone. An initial reverse transport phase ensured that all material was carried to the bottom end of the ampoule, and that there were few nucleation sites for crystals in the rest of the ampoule. The time-temperature profile had a large influence the crystal sizes and morphologies; the profile listed here was found to produce acceptably large and well-formed crystals.

[1]Some other Nb sources were found to contain significant amounts of hydrogen. During baking, this reacted with oxygen and selenium in the ampoule to form water and hydrogen selenide.

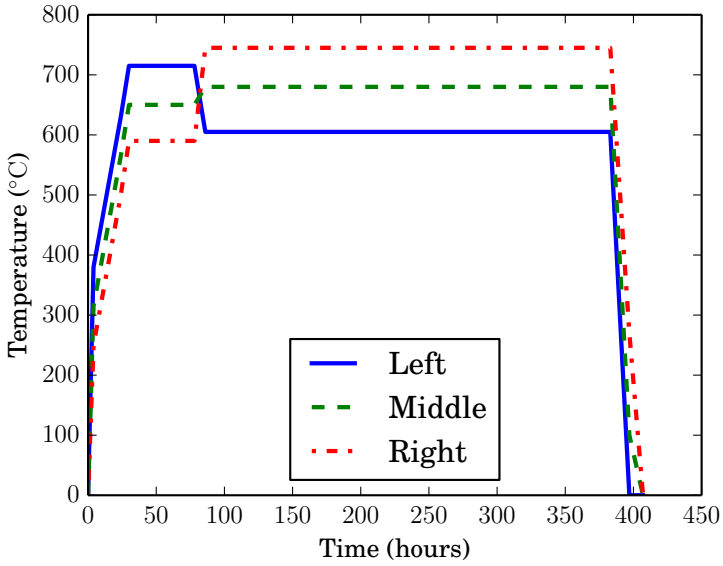


Figure A.1: Furnace program for $NbSe_3$ growth

# Appendix B

# Sample mounting and cryostats

Samples were mounted on polished alumina substrates (Fig. B.1) pattered with 20 nm thick gold traces. These substrates were prepared at the the Cornell NanoScale Science and Technology Facility (CNF) using standard photolithography and lift-off techniques. A 2 nm Cr adhesion layer was thermally evaporated through a resist mask onto the alumina; immediately afterward, a 18 nm of Au was deposited via electron-beam evaporation.

Crystals of $NbSe_3$ were selected, trimmed to length with a sharp razor blade, and laid atop the contact traces. The ends were left at least 0.5 mm longer than the contacted portion, to avoid damage to the latter. If the crystal did not initially make good contact with the traces, a drop of isopropanol was applied, which, as it evaporated, pulled the crystal into contact via surface tension. Electrostatic attraction was usually sufficient to hold the crystal in place, but a drop of 0.5% (w/v) ethyl cellulose in ethyl acetate improved contact resistances and reliability.

Spring-loaded "pogo" pins (Fig. B.6) were used to contact the square pads on the substrates. The substrates were mounted on a solid copper block in the cryostat, which minimized thermal gradients across the sample.

Most of the data in this work were collected using a custom-made immersion cryostat. Figure B.2 shows the lower portion of the cryostat, and Fig. B.4 shows the room-temperature portion. A vacuum-tight cylindrical stainless steel shield surrounds the stage and wiring.

The shield is lowered into a dewar of liquid nitrogen. Radiation and conduction through residual gas cool the stage and sample. A film heater affixed to the bottom of the copper sample stage maintains the stage temperature, which is monitored using a silicon diode sensor, and controlled by a Cryocon Model 24 temperature controller.

The cryogenic amplifiers are mounted below and are isolated from the sample stage, so that they can remain at approximately 77 K (and thus benefit from reduced thermal noise), even when the sample stage is at a higher temperature. To facilitate maintenance and testing, the amplifiers are placed on printed circuit boards (PCBs) having the same dimensions and edge-contact pattern as a standard Secure Digital (SD) card, and are inserted into SD card holders mounted on the cryostat (Fig. B.3).

Coaxial cables are used to conduct high-frequency signals from the cryogenic amplifiers to the room temperature stage, and to conduct the sample bias currents. Auxiliary twisted pairs supply power to the amplifiers. All of the cabling passes through vacuum-tight feedthroughs (sealed using a high-vacuum wax) in a room-temperature flange.

Great care was taken to reduce noise and electromagnetic interference (EMI) in the cryostat. A continuous metal shield surrounds the entire assembly. The amplifiers are powered by rechargeable batteries. The heater is enclosed by copper foil, and all the heater and temperature sensor wiring runs through its own separate shielded conduit. Additionally, the heater and temperature controller wiring is lowpass-filtered before it enters the cryostat. Without this shielding, the temperature controller introduced unacceptable noise into the measurements. The current source used to supply a DC bias to the samples was also found to be noisy, so this, too, is filtered through a 10 Hz lowpass filter outside of the cryostat.

High-quality samples of $NbSe_3$ are rare. Most crystals, even those which are visually uniform, do not exhibit complete mode locking. Thus, it is often necessary to test a large number of samples before a good specimen is obtained. The cryostat described above, like most medium- to large-sized cryostats, requires a long time (approximately 45 minutes, in this case) to cool from room temperature to cryogenic temperatures, and approximately the

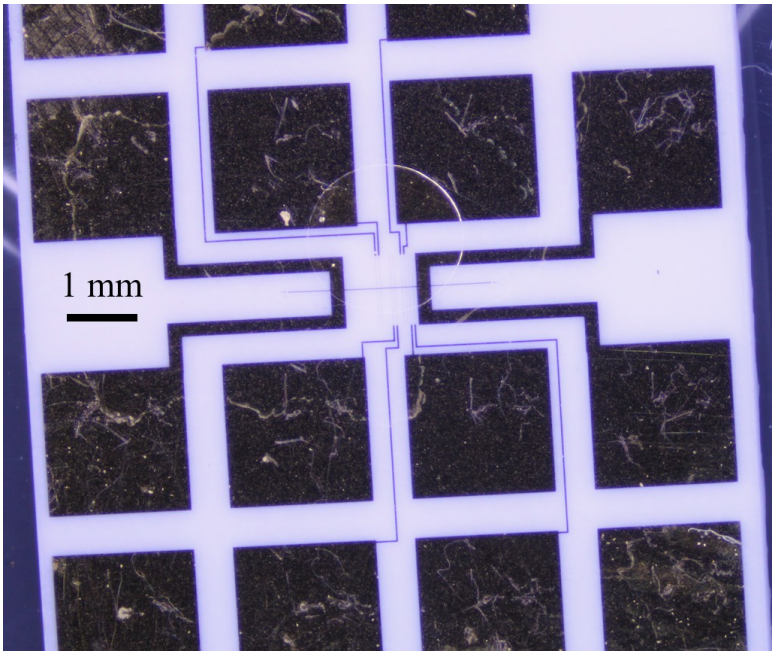


Figure B.1: Alumina sample substrate. Gold traces 20 nm in thickness are evaporated on top of the alumina. A crystal of nbse is laid across the contact pattern and affixed with a drop of ethyl cellulose dissolved in ethyl acetate. The large square pads make contact with spring-loaded "pogo pins," pressed down from above.

same time to warm up again.

To facilitate rapid testing of samples, a small cryostat, with a low-mass sample stage, was developed (Fig. B.5). It is unshielded and has only twisted-pair wiring, but it is sufficient to measure mode-locking quality and other basic transport characteristics. A fused quartz enclosure allows the sample to be viewed easily, and improves radiative cooling. To further increase the cooling rate, the enclosure can be filled with helium. This cryostat can be cycled (cooled and warmed again) in approximately ten minutes.

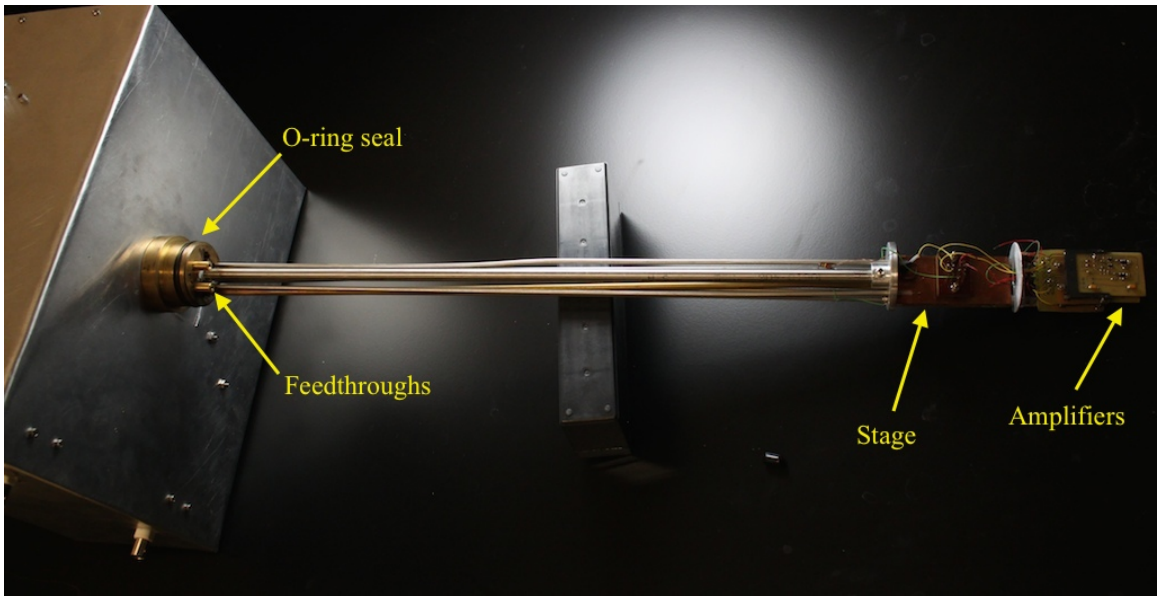


Figure B.2: Lower portion of the immersion cryostat. Coaxial cables and other wiring are led through vacuum-tight feedthroughs in the room-temperature portion. An O-ring forms a seal with a cylindrical stainless steel shield (not shown). The stage is located approximately 50 cm below the room-temperature portion.

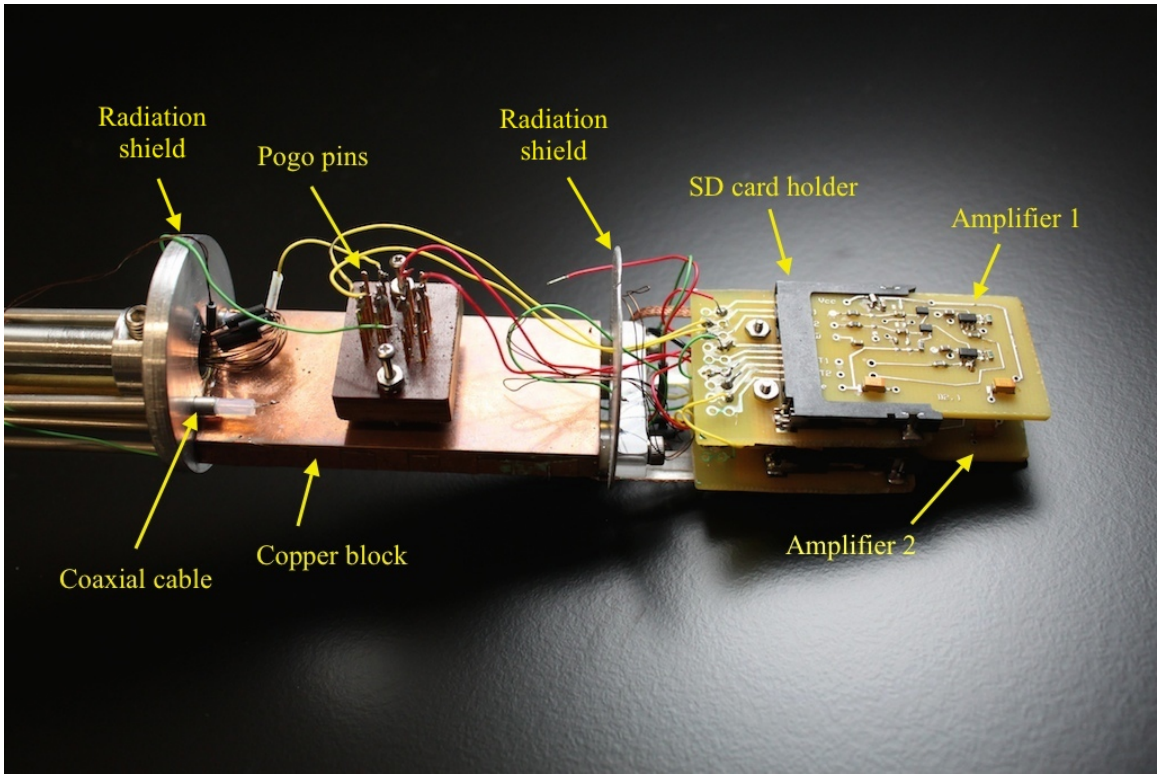


Figure B.3: Cryostat stage. Coaxial cables run from the room-temperature portion (toward the left) to the stage. A film heater (not shown) is attached to the bottom of the stage and completely surrounded by copper foil. The heater wiring is routed through its own separate metal tube. The sample substrate is placed on top of the copper block, and the screws are used to bring the pogo pins firmly into contact with the sample pads. The amplifiers are mounted in secure-digital (SD) card holders located below and isolated from the stage.

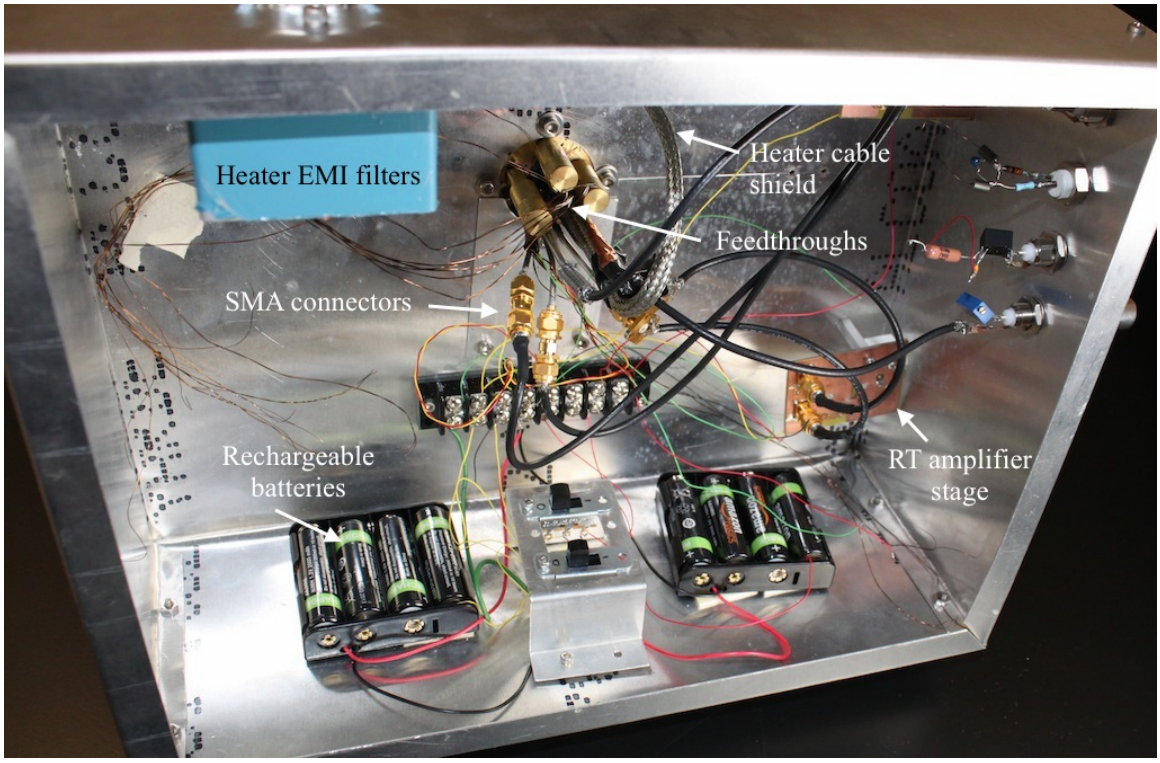


Figure B.4: Room-temperature portion of the cryostat. The signals from the cryogenic differential amplifiers stages are further amplified and buffered by the room-temperature stages. The amplifier is powered by rechargeable batteries. A metal lid (not shown) completes the shielding.

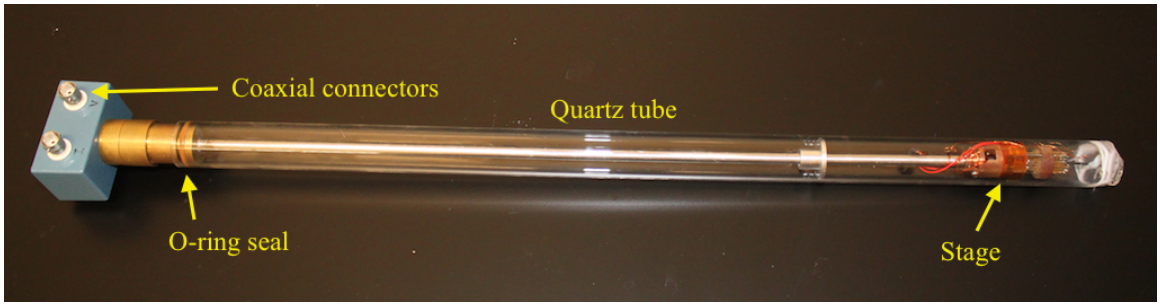


Figure B.5: Small cryostat, used for rapid testing of sample quality

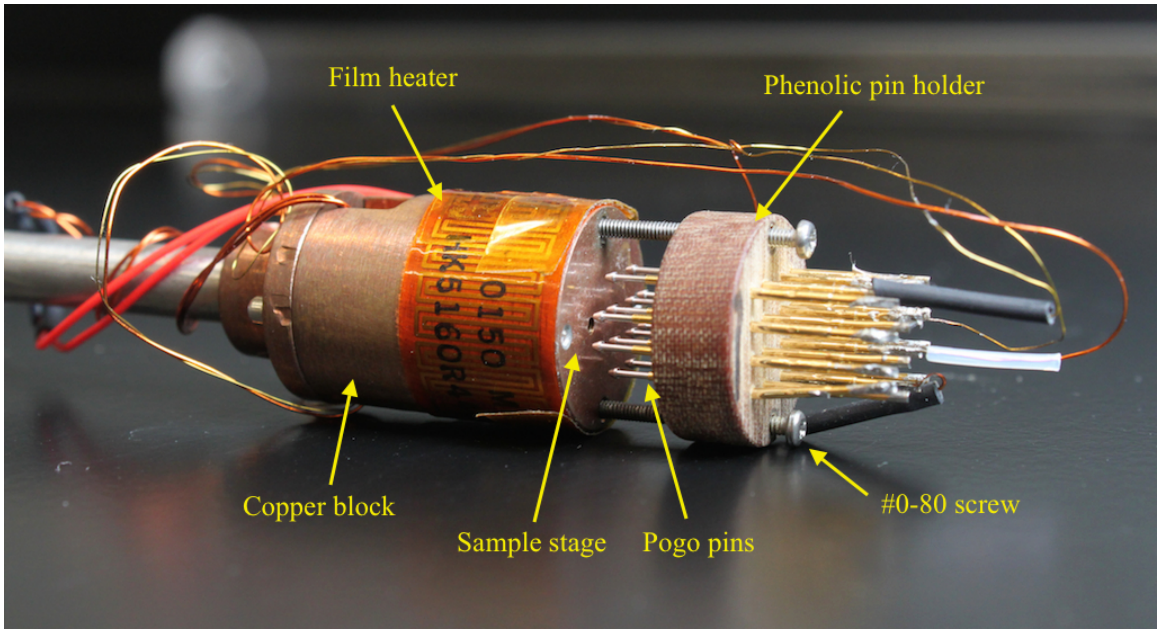


Figure B.6: Small cryostat stage

# Bibliography


[1] S. Abe. Numerical experiments on glassy charge density waves. *J. Phys. Soc. Japan*, 55(6), 1986.

[2] T. L. Adelman, M. C. de Lind van Wijngaarden, S. V. Zaitsev-Zotov, D. DiCarlo, and R. E. Thorne. Phase slip and the spatiotemporal response of charge-density waves in $NbSe_3$. *Phys. Rev. B*, 52(8), 1995.

[3] T. L. Adelman, S. V. Zaitsev-Zotov, and R. E. Thorne. Field-effect modulation of charge-density-wave transport in $NbSe_3$ and $TaS_3$. *Phys. Rev. Lett.*, 74(26), 1995.

[4] T. L. Adelman, M. C. de Lind van Wijngaarden, S. V. Zaitsev-Zotov, D. DiCarlo, and R. E. Thorne. Spatially resolved studies of charge-density-wave dynamics and phase slip in $NbSe_3$. *Phys. Rev. B*, 53(4), 1996.

[5] N. Beev and M. Kiviranta. Cryogenic low-noise dc-coupled wideband differential amplifier based on SiGe heterojunction bipolar transistors. *Rev. Sci. Instrum.*, 83(066107), 2013.

[6] N. Beev and M. Kiviranta. Fully differential cryogenic transistor amplifier. *Cryogenics*, 57, 2013.

[7] S. Bhattacharya, J. P. Stokes, M. O. Robbins, and R. A. Klemm. Origin of broadband noise in charge-density-wave conductors. *Phys. Rev. Lett.*, 54(22), 1985.

[8] S. Bhattacharya, J. P. Stokes, and M. J. Higgins. Temporal coherence in the sliding charge-density-wave condensate. *Phys. Rev. Lett.*, 59(16), 1987.

[9] K. Biljakovic, J. C. Lasjaunias, and P. Monceau. Aging effects and nonexponential energy relaxations in charge-density-wave systems. *Phys. Rev. Lett.*, 62(13), 1989.

[10] K. Biljakovic, J. C. Lasjaunias, P. Monceau, and F. Levy. Towards equilibrium ground state in charge-density-wave systems. *Phys. Rev. Lett.*, 67(14), 1991.

[11] I. Bloom, A. C. Marley, and M. B. Weissman. Nonequilibrium dynamics of discrete fluctuators in charge-density waves in $NbSe_3$. *Phys. Rev. Lett.*, 71(26), 1993.

[12] I. Bloom, A. C. Marley, and M. B. Weissman. Correlation between broad-band noise and frequency fluctuations of narrow-band noise in the charge-density wave in $NbSe_3$. *Phys. Rev. B*, 50(16), 1994.

[13] I. Bloom, A. C. Marley, and M. B. Weissman. Discrete fluctuators and broadband noise in the charge-density-wave in $NbSe_3$. *Phys. Rev. B*, 50(8), 1994.

[14] S. Brazovskii and N. Kirova. Plastic sliding, strained states and current conversion in density waves. *Synth. Metals*, 103:2589–2592, 1999.

[15] S. Brazovskii and T. Nattermann. Pinning and sliding of driven elastic systems: From domain walls to charge density waves. *Adv. in Phys.*, 53(2):177–252, 2004.

[16] S. Brazovskii, N. Kirova, H. Requardt, F. Ya. Nad, P. Monceau, R. Currat, J. E. Lorenzo, G. Grubel, and Ch. Vettier. Plastic sliding of charge density waves: X-ray space resolved-studies versus theory of current conversion. *Phys. Rev. B*, 61(16): 10640–10650, 2000.

[17] C. Brun, Z. Z. Wang, and P. Monceau. Scanning tunneling microscopy at the $NbSe_3$ surface: Evidence for interaction between $q_1$ and $q_2$ charge-density waves in the pinned regime.

[18] J. H. Cho, J. Lee, Y. Xia, B. Kim, Y. He, M. J. Renn, T. P. Lodge, and C. D. Frisbie. Printable ion-gen gate dielectrics for low-voltage polymer thin-film transistors on plastic. *Nature Materials*, 7:900–906, 2008.

[19] A. S. Dhoot, J. D. Yuen, M. Heeney, I. McCulloch, D. Moses, and A. J. Heeger. Beyond the metal-insulator transition in polymer electrolyte gated polymer field-effect transistors. *Proc. Nat. Acad. Sci.*, 103(2):11834–11837, 2006.

[20] D. Dicarlo, E. Sweetland, M. Sutton, J. D. Brock, and R. E. Thorne. Field-induced charge-density-wave deformations and phase slip in $NbSe_3$. *Phys. Rev. Lett.*, 70(6), 1993.

[21] D. DiCarlo, R. E. Thorne, E. Sweetland, M. Sutton, and J. D. Brock. Charge-density wave structure in $NbSe_3$. *Phys. Rev. B*, 50(12), 1994.

[22] T. Ekino and J. Akimitsu. CDW tunneling density of states in $NbSe_3$. *Physica B*, 194-196:1221–1222, 1994.

[23] R. M. Fleming. The non-linear response of $NbSe_3$ to pulsed electric fields. *Solid State Comm.*, 43(2), 1982.

[24] R. M. Fleming and C. C. Grimes. Sliding-mode conductivity in $NbSe_3$: Observation of a threshold electric field and conduction noise. *Phys. Rev. Lett.*, 42(21), 1979.

[25] R. M. Fleming and L. F. Schneemeyer. Transient electrical response of $K_{0.30}MoO_3$. *Phys. Rev. B*, 28(12), 1983.

[26] R. M. Fleming, D. E. Moncton, and D. B. McWhan. X-ray scattering and electric field studies of the sliding mode conductor $NbSe_3$. *Phys. Rev. B*, 18(10), 1978.

[27] H. Frölich. On the theory of superconductivity: the one-dimensional case. *Proc. R. Soc. Lond. A*, 223:296–305, 1954.

[28] H. Fukuyama. Pinning in Peirls-Fröhlich state and conductivity. *J. Phys. Soc. Japan*, 41(2), 1976.

[29] H. Fukuyama and P. A. Lee. Dynamics of the charge-density wave. I. Impurity pinning in a single chain. *Phys. Rev. B*, 17(2), 1978.

[30] J. C. Gill. Transient non-linear conduction in niobium triselenide. *Physica B*, 108, 1981.

[31] J. C. Gill. Transient non-linear phenomena and metastable states of charge-density waves in nioblium triselenide. *Solid State Comm.*, 39(11):1203–1208, 1981.

[32] J. C. Gill. Thermally initiated phase-slip in the motion and relaxation of charge-density waves in niobium triselenide. *J. Phys. C: Solid State Phys.*, 19:6589–6604, 1986.

[33] J. C. Gill. Charge-density wave transport. *Contemp. Phys.*, 27(1), 1986.

[34] J. C. Gill. Dislocation and the motion of weakly pinned charge density waves: Experiments on niobium triselenide containing mobile indium impurities. *Phys. Rev. B*, 53 (23), 1996.

[35] J. C. Gill. Pulse duration memory of weakly pinned charge-density waves. *Phys. Rev. B*, 63(125125), 2001.

[36] J. C. Gill. A model of coherent creep and switching in charge density wave conduction in $NbSe_3$ at low temperatures. *J. Phys. IV France*, 12(Pr9-161), 2002.

[37] G. Grüner. The dynamics of charge-density waves. *Rev. Mod. Phys.*, 60(4), 1988.

[38] G. Grüner. *Density Waves in Solids*. Perseus Publishing, 1994.

[39] J. L. Hodeau, M. Marezio, C. Rocau, R. Ayroles, A. Meerschaut, J. Rouxel, and P. Monceau. Charge-density waves in $NbSe_3$ at 145 K: crystal structures, x-ray and electron diffraction studies. *J. Phys. C: Solid State Phys.*, 11:4117–4134, 1978.

[40] A. F. Isakovic, P. G. Evans, J. Kmetko, K. Cicak, Z. Cai, B. Lai, and R. E. Thorne. Shear modulus and plasticity of a driven charge density wave. *Phys. Rev. Lett.*, 96 (046401), 2006.

[41] A. F. Isakovic, K. Cicak, and R. E. Thorne. End-current injection contacts for anisotropic materials: Fabrication and application to the quasi-one-dimensional conductor $NbSe_3$. *Phys. Rev. B*, 88(115141), 2008.

[42] G. Kriza and G. Mihály. Stretched-exponential dielectric relaxation in a charge-density-wave system. *Phys. Rev. Lett.*, 56(23), 1986.

[43] M. Lee, J.R. Williams, S. Zhang, C.D. Frisbie, and D. Goldhaber-Gordon. Electrolyte gate-controlled kondo effect in $SrTiO_3$. *Phys. Rev. Lett.*, 25(107), 2011.

[44] P. A. Lee and H. Fukuyama. Dynamics of the charge-density wave. II. Long-range Coulomb effect in an array of chains. *Phys. Rev. B*, 17(2), 1978.

[45] P. A. Lee and T. M. Rice. Electric field depinning of charge-density waves. *Phys. Rev. B*, 19(8), 1979.

[46] S. G. Lemay, M. C. de Lind van Wijngaarden, T. L. Adelman, and R. E. Thorne. Spatial distribution of charge-density-wave phase slip in $NbSe_3$. *Phys. Rev. B*, 57(20): 12781–12791, 1998.

[47] S. G. Lemay, K. Cicak, K. O'Neill, and R. E. Thorne. Probing charge-density-wave dynamics: Spatial noise correlations and nonlocal conduction. *Phys. Rev. B*, 64(205106), 2001.

[48] Y. Li, S. G. Lemay, J. H. Prince, K. Cicak, K. O'Neill, K. Ringland, K. D. Finkelstein, J. D. Brock, and R. E. Thorne. Imaging shear in sliding charge-density waves by X-ray diffraction topography. *Phys. Rev. Lett.*, 83(17), 1999.

[49] P. B. Littlewood. Sliding charge-density waves: A numerical study. *Phys. Rev. B*, 33 (10), 1986.

[50] P. B. Littlewood. Screened dielectric response of sliding charge-density waves. *Phys. Rev. B*, 36(6), 1987.

[51] P. B. Littlewood and R. Rammal. Glassy relaxation in the Fukuyama-Lee-Rice model of charge-density waves. *Phys. Rev. B*, 38(4), 1988.

[52] J. W. Lyding, J. S. Hubacek, G. Gammie, and R. E. Thorne. Evidence for bulk "narrow-band noise" in $NbSe_3$: Thermal gradient studies. *Phys. Rev. B*, 33(6), 1986.

[53] M. P. Maher, T. L. Adelman, J. McCarten, D. Dicarlo, and R. E. Thorne. Size effects, phase slip, and the origin of $f^{-\alpha}$ noise in $NbSe_3$. *Phys. Rev. B*, 43(12), 1991.

[54] O. C. Mantel, F. Chalin, C. Dekker, and H. S. J. van der Zant. Charge-density-wave current conversion in submicron $NbSe_3$ wires. *Phys. Rev. Lett.*, 84(3), 2000.

[55] A. C. Marley, M. B. Weissman, and H. T. Hardner. Out-of-phase noise in charge-density waves carrying current. *Phys. Rev. B*, 50(7), 1994.

[56] H. Matsukawa. Static and dynamic properties of charge-density-waves described by the fukuyama-lee-rice model. II. Perturbational analysis on the dc + ac combined phenomena. *J. Phys. Soc. Japan*, 56(4), 1987.

[57] S. Matthews, R. Ramesh, T. Venkatesan, and J. Bendetto. Ferroelectric field effect transistor based on epitaxial perovskite heterostructures. *Science*, 276(11), 1997.

[58] J. McCarten, D. A. DiCarlo, M. P. Maher, T. L. Adelman, and R. E. Thorne. Charge-density-wave pinning and finite-size effects in $NbSe_3$. *Phys. Rev. B*, 46(8), 1991.

[59] A. Meerschaut and J. Rou. Le seleniure $NbSe_3$: obtention et structure. *J. Less-Common Metals*, 39:197–203, 1975.

[60] A. A. Middleton. Critical behavior of charge-density waves below the threshold for sliding. *Phys. Rev. Lett.*, 66(1), 1991.

[61] A. A. Middleton. Asymptotic uniqueness of the sliding state for charge density waves. *Phys. Rev. Lett.*, 68(5), 1992.

[62] A. A. Middleton. Thermal rounding of the charge-density-wave depinning transition. *Phys. Rev. B*, 45(16), 1992.

[63] A. A. Middleton and D. S. Fisher. Critical behavior of charge-density-waves below threshold: Numerical and scaling analysis. *Phys. Rev. B*, 47(7), 1993.

[64] G. Mihály and L. Mihály. Spontaneous decay of metastable states in orthorhombic $TaS_3$. *Phys. Rev. Lett.*, 52(2), 1984.

[65] L. Mihály and G. X. Tessema. Dielectric hysteresis and relaxation in the charge-density-wave compound $K_{0.3}MoO_3$. *Phys. Rev. B*, 33(8), 1986.

[66] P. Monceau. Electronic crystals: an experimental overview. *Adv. in Phys.*, 61(4), 2012.

[67] P. Monceau, N. P. Ong, A. M. Portis, A. Meerschaut, and J. Rouxel. Electric field breakdown of charge-density-wave–induced anomalies in $NbSe_3$. *Phys. Rev. Lett.*, 37 (10), 1976.

[68] P. Monceau, J. Richard, and M. Renard. Interference effects of the charge-density-wave motion in $NbSe_3$. *Phys. Rev. Lett.*, 45(1), 1980.

[69] P. Monceau, M. Renard, J. Richard, and M.C. Saint-Lager. Breaking of the cdw coherence in various inhomogeneous situations. *Physica B*, 143:64–68, 1986.

[70] C. R. Myers and J. P. Sethna. Collective dynamics in a model of sliding charge-density waves. I. Critical behavior. *Phys. Rev. B.*, 47(17), 1993.

[71] F. Nad and P. Monceau. Charge-density-wave glass state in quasi-one-dimensional conductors. *Phys. Rev. B*, 51(4), 1995.

[72] F. Ya. Nad and P. Monceau. Transition of charge-density-wave conductors into a glassy-like state. *Solid State Comm.*, 87(1), 1993.

[73] O. Narayan and D. S. Fisher. Threshold critical dynamics of driven interfaces in random media. *Phys. Rev. B*, 48(10), 1993.

[74] O. Narayan and A. A. Middleton. Avalanches and the renormalization group for pinned charge-density waves. *Phys. Rev. B*, 49(1), 1994.

[75] K. O'Neill, K. Cicak, and R. E. Thorne. Measurement of the shear strength of a charge density wave. *Phys. Rev. Lett.*, 93(6), 2004.

[76] K. O'Neill, E. Slot, R. E. Thorne, and H. S. J. van der Zant. In-chain tunneling through charge-density-wave nanoconstrictions and break junctions. *Phys. Rev. Lett.*, 96:096402, 2006.

[77] N. P. Ong and J. W. Brill. Conductivity anisotropy and transverse magnetoresistance of $NbSe_3$. *Phys. Rev. B*, 18(10), 1978.

[78] N. P. Ong and K. Maki. Generation of charge-density-wave conduction noise by moving phase vortices. *Phys. Rev. B*, 32(10), 1985.

[79] N. P. Ong and P. Monceau. Anomalous transport properties of a linear-chain metal: $NbSe_3$. *Phys. Rev. B*, 16(8), 1977.

[80] N. P. Ong, G. Verma, and K. Maki. Vortex-array model for charge-density-wave conduction noise. *Phys. Rev. Lett.*, 52(8), 1984.

[81] P. Parilla and A. Zettl. Transient charge-density-wave dynamics in $NbSe_3$. *Phys. Rev. B*, 32(12), 1985.

[82] R. E. Peierls. *Ann. Phys. Leipz.*, 4(121), 1930.

[83] A. Perucchi, L. Degiorgi, and R. E. Thorne. Optical investigation of the charge-density-wave phase transitions in $NbSe_3$. *Phys. Rev. B*, 69(195114), 2004.

[84] E. Pinsolle, N. Kirova, V. L. R. Jacques, A. A. Sinchenko, and D. Le Bolloc'h. Creep, flow, and phase slippage regimes: An extensive view of the sliding charge-density wave revealed by coherent X-ray diffraction. *Phys. Rev. Lett.*, 109(256402), 2012.

[85] H. Requardt, F. Ya. Nad, P. Monceau, R. Currat, J. E. Lorenzo, S. Brazovskii, N. Kirova, G. Grübel, and Ch. Vettier. Direct observation of charge density wave current conversion by spatially resolved synchrotron X-ray studies in $NbSe_3$. *Phys. Rev. Lett.*, 25, 80.

[86] D. Rideau, P. Monceau, R. Currat, H. Requardt, F. Nad, J. E. Lorenzo, S. Brazovskii, C. Detlefs, and G. Grübel. High resolution X-ray scattering techniques for studying the sliding CDWS distortions in $NbSe_3$. *Nuc. Instrum. Meth. in Phys. Res. A.*, 476-468, 2001.

[87] D. Rideau, P. Monceau, R. Currat, H. Requardt, F. Nad, J. E. Lorenzo, S. Brazovskii, C. Detlefs, and G. Grübel. X-ray scattering evidence for macroscopic strong pinning centers in the sliding CDW state of $NbSe_3$. *Europhys. Lett.*, 56(2), 2001.

[88] J. Schäfer, E. Rotenberg, S. D. Kevan, P. Blaha, R. Claessen, and R. E. Thorne. High-temperature symmetry breaking in the electronic band structure of the quasi-one-dimensional solid $NbSe_3$. *Phys. Rev. Lett.*, 87(19), 2001.

[89] J. Schäfer, M. Sing, R. Claessen, E. Rotenberg, X. J. Zhou, R. E. Thorne, and S. D. Kevan. Unusual spectral behavior of charge-density waves with imperfect nesting in a quasi-one-dimensional metal. *Phys. Rev. Lett.*, 91(6), 2003.

[90] M.S. Sherwin and A. Zettl. Complete charge-density-wave mode locking and freeze-out of fluctuations in $NbSe_3$. *Phys. Rev. B*, 32(8), 1985.

[91] A. A. Sinchenko and P. Monceau. Charge-density wave gaps of $NbSe_3$ measured by point-contact spectroscopy in different crystallographic orientations. *Phys. Rev. B*, 67 (125117), 2003.

[92] E. Slot and H. S. J. van der Zant. Focused-ion-beam fabricated charge density wave devices. *J. Phys. IV France*, 12(Pr9-103-108), 2002.

[93] E. Slot, H. S. J. van der Zant, and R. E. Thorne. Electric-field distribution near current contacts of anisotropic materials. *Phys. Rev. B*, 65(033403), 2001.

[94] E. Slot, H. S. J. van der Zant, K. O'Neill, and R. E. Thorne. Crossover from two-dimensional to one-dimensional collective pinning in $NbSe_3$. *Phys. Rev. B*, 69(073105), 2004.

[95] L. Sneddon. Sliding charge-density waves: II. ac properties. *Phys. Rev. B*, 29(2), 1984.

[96] L. Sneddon, M. C. Cross, and D. S. Fisher. Sliding conductivity of charge-density waves. *Phys. Rev. Lett.*, 49(4), 1982.

[97] D. Starešinić, K. Hosseini, W. Bütting, K. Biljaković, E. Riedel, and S. van Smaalen. Glass transition and secondary relaxation in the charge-density-wave system $K_{0.3}MoO_3$. *Phys. Rev. B*, 69(113102), 2004.

[98] G. X. Tessema and N. P. Ong. Phase-plot studies of the alternating charge-density-wave current in niobium trielenide. *Phys. Rev. B*, 31(2), 1985.

[99] R. E. Thorne. Effect of crystal-growth conditions on charge-density-wave pinning in $NbSe_3$. *Phys. Rev. B*, 45(11), 1992.

[100] R. E. Thorne. A history of the $i - v$ characteristic of cdw conductors. *J. Phys. IV France*, 131:89–94, 2005.

[101] R. E. Thorne and J. R. Tucker. Experiment versus the classical model of deformable charge-density waves: Interference phenomena and mode locking. *Phys. Rev. Lett.*, 58 (8):828–831, 1987.

[102] R. E. Thorne, W. G. Lyons, J. W. Lyding, and J. R. Tucker. Charge-density-wave transport in quasi-one-dimensional conductors. II. ac-dc interference phenomena. *Phys. Rev. B*, 35(12), 1987.

[103] R. E. Thorne, W. G. Lyons, J. W. Lyding, J. R. Tucker, and J. Bardeen. Charge-density-wave transport in quasi-one-dimensional conductors. I. Current oscillations. *Phys. Rev. B*, 35(12), 1987.

[104] R. E. Thorne, J. S. Hubacek, W. G. Lyons, J. W. Lyding, and J. R. Tucker. ac-dc interference, complete mode locking, and origin of coherent oscillations in sliding charge-density-wave systems. *Phys. Rev. B.*, 37(17), 1988.

[105] J. Toner. Glassy dynamics of two-dimensional vortex glasses, charge-density waves, and surfaces of disordered crystals. *Phys. Rev. Lett.*, 67(18), 1991.

[106] G. Verma and N. P. Ong. Effect of a thermal gradient on charge-density-wave conduction-noise spectrum in $NbSe_3$. *Phys. Rev. B*, 30(5), 1984.

[107] M. B. Weissman. Low-frequency noise as a tool to study disordered materials. *Annu. Rev. Mater. Sci.*, 26:395–429, 1996.

[108] J. A. Wilson. Bands, bonds, and charge-density waves in the $NbSe_3$ familiy of compounds. *Phys. Rev. B*, 19(12), 1979.

[109] W-Y. Wu, L. Mihály, G. Mozurkevich, and G. Gruner. Low-frequency response of pinned charge-density-wave condensates. *Phys. Rev. B*, 33(4), 1986.

[110] X.-D. Xiang and J. W. Brill. Effects of charge-density-wave depinning on the elastic properties of $NbSe_3$. *Phys. Rev. B*, 39(2), 1989.

[111] Z. G. Xu and J. W. Brill. Relaxation and elastic anomalies in charge-density-wave conductors. *Phys. Rev. B*, 45(8), 1992.

[112] A. Zettl, M. Kaiser, and G. Grüner. Non-equilibrium transport in $NbSe_3$: Effects of a temperature gradient. *Solid State Comm.*, 55(8), 1985.

# Volume II

X-Ray Fluorescence Imaging of Archaeological Artifacts

# Contents

# List of Figures

# Chapter 1

# Introduction

## 1.1 X-ray fluorescence imaging

Archaeological artifacts are often poorly preserved. Weathering, leaching, erosion, fading, encrustation, and even deliberate alteration can all conceal the original appearance, design, and construction of these artifacts. For example, the ancient Mesopotamian glass fragments analyzed later in this volume were once decorated with intricate patterns of brightly colored glass, but these colors are now all but invisible to the unaided eye.

X-ray fluorescence imaging (XRFI) is a powerful technique for recovering this lost information. A narrow, collimated beam of synchrotron-generated X-rays is swept across the

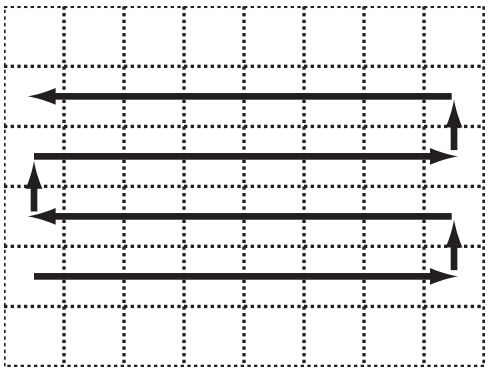

Figure 1.1: To generate an XRFI map, the beam is swept back and forth across the sample in a zig-zag pattern. A fluorescence spectrum is recorded at each point on a regular grid.

surface of the sample, following a raster pattern (Fig. 1.1). The atoms near the surface of the sample (within a few hundred micrometers, depending on the density) fluoresce with photons of characteristic energies. By recording an energy spectrum at each point on a regular grid of "pixels," and fitting these spectra to the known atomic spectra, it is possible to map out the distribution of elements, with sensitivities approaching a few parts per million, across the entire surface of a sample.

Even when visual evidence of decorative patterns has been lost, traces elements often remain. Additionally, the penetration depth of X-rays makes it possible to image features hidden under layers of dirt, paint, or other encrustation.

Synchrotron-based X-ray fluorescence imaging (SR-XRFI) offers many advantages over conventional tube-based analysis. Synchrotron beams are monochromatic, which greatly eases analysis of the spectra, and improves sensitivity. The beam energy can be tuned to most efficient excite fluorescence in the elements of interest, or to vary the penetration depth. The collimated beams can be focused down to spots smaller than a micrometer. Perhaps most importantly, the intensities of synchrotron beams are millions of times higher than those available from tube sources. Spectra with good counting statistics can be acquired in milliseconds, instead of hours. The analyses reported below would be infeasible with a tube source.

## 1.2 Experimental setup

The following basic configuration was used (with minor variations where noted), for all of the measurements reported below. The work was performed at beamline F3 at the Cornell High Energy Synchrotron Source (CHESS). Figure 1.4 shows a photograph of the sample hutch at F3. A double-bounce multilayer molybdenum–boron carbide monochromator provided a tunable 10-20 keV beam with a bandwidth of 0.6% and a flux of approximately $1 \times 10^{11}$ photon/s/mm$^2$ whose intensity was monitored using a set of ion chambers. Beam

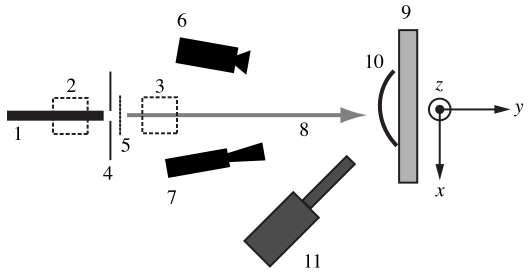


Figure 1.2: Experimental setup. (1) Incident x-ray beam (2) first ion chamber (3) second ion chamber (4) beam size control slits (5) attenuator (6) wide field camera (7) zoom camera (8) attenuated, narrow X-ray beam (9) XYZ stage (10) sample.

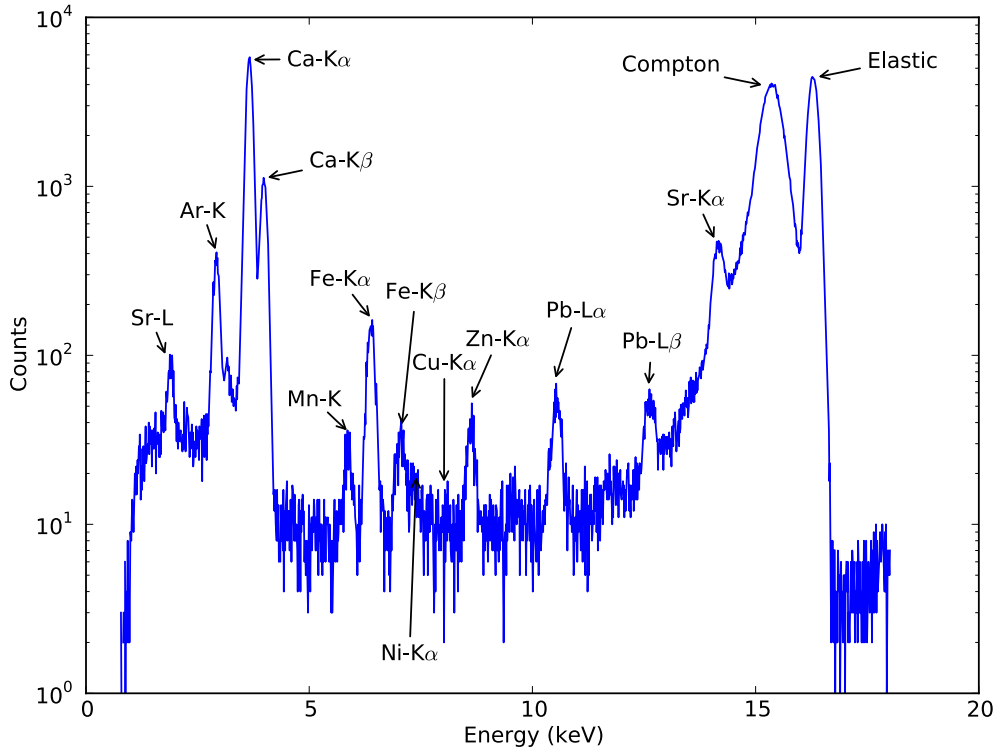


Figure 1.3: A typical XRF spectrum. The fluorescence peaks for several elements are labeled, as are the Compton and elastic scattering peaks. The argon peak is due to atmospheric argon, not the sample.

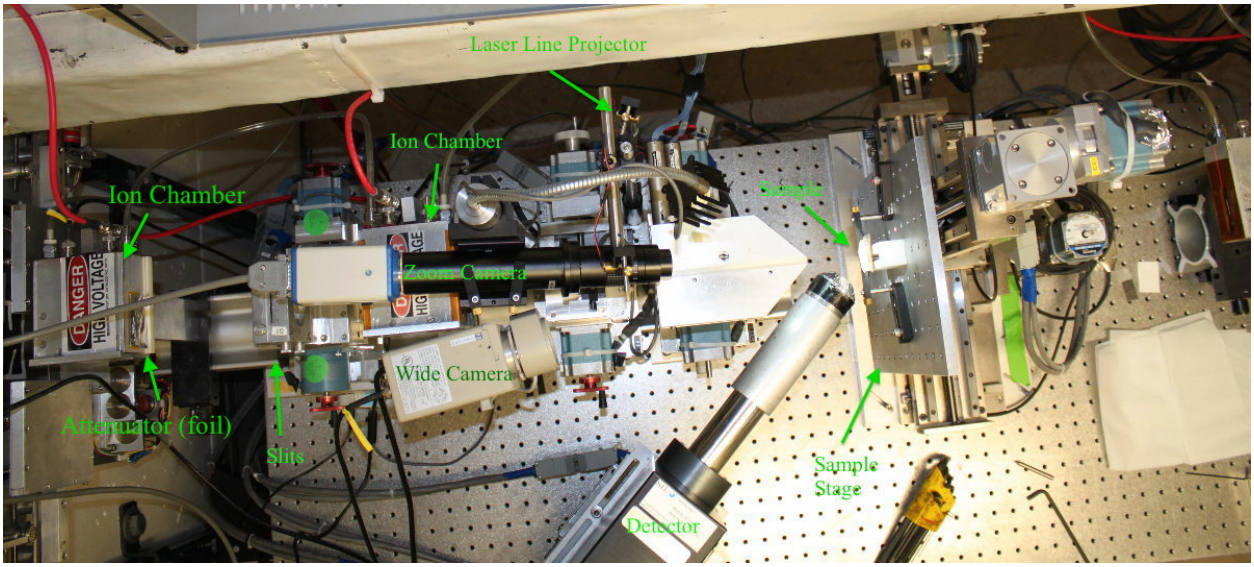


Figure 1.4: An overhead view of the setup inside the sample hutch at CHESS's F3 beamline.

size was controlled by a pair of adjustable slits, one horizontal and one vertical. Samples were mounted on a motorized XYZ table, which could be positioned with an accuracy of better than 10 µm. The sample stage was typically oriented with its surface perpendicular to the beam, and the detector was located at 45 to one side, in the horizontal plane of the beam (Fig. 1.2). (See below for a discussion of the tradeoff between Compton scattering and topography effects.) Fluorescent and scattered photons were measured using a four-element Vortex-ME4 silicon drift detector (SII Nanotechnology). Count rates were limited to approximately 100,000 per second per element by attenuating the incident beam, to avoid detector pulse pile-up and excessive dead times. A DXP-XMAP (XIA LLC) digital spectrometer generated spectra of photon counts versus energy.

To generate XRF images, an XRF spectrum was recorded at each point or pixel by raster scanning the XYZ table and thus the sample relative to the X-ray beam. Typical grid spacings were 0.1 mm to 0.25 mm, and scan speeds were typically 1 mm/s, the maximum allowed by table motors. The zig-zag pattern shown in Fig. 1.1 avoided wasting time while the stage translated back to the beginning of each row. During the horizontal motions, the MCA counted photons continuously, so the recorded spectra for each pixel represent the average over the full width of the pixel. To locate the X-ray beam on the sample and register

XRF and optical images, the sample was illuminated using crossed laser lines and imaged using two video cameras.

Data acquisition and sample positioning were automated by the SPEC software package (Certified Scientific Software). The EPICS software system (Argonne National Laboratory) served as an interface between SPEC and the DXP-XMAP. Graphical display of element maps and estimates of elemental compositions were performed using XPAXS (Darren Dale, CHESS), which used the PyMCA library (Armando Sol, European Synchrotron Radiation Facility) [36] for fundamental parameters elemental composition analysis.

Figure 1.3 shows a representative XRF spectrum. Each element fluoresces at multiple energies, but the ratio of the intensities of the sub-peaks is known, so fitting algorithms (such as the one used in PyMCA) take advantage of this by fitting groups instead of individual peaks. This makes it possible, in most cases, to separate the contributions of elements with overlapping peaks.

## 1.3 Comparison with other analytical techniques

While a comprehensive review of elemental analysis methods in art and archaeology is beyond the scope of this work, a brief summary of the competing techniques may help to clarify the advantages and disadvantages of SR-XRFI.

### 1.3.1 Instrumental Neutron Activation Analysis (INAA)

In this technique, samples are irradiated with low-energy neutrons, some of which are captured by atomic nuclei in the sample. The resulting isotopes are often unstable and subsequently decay, emitting radiation. Typically, the gamma radiation spectrum is measured; since isotopes decay with unique gamma emission energies, it is possible to identify and quantify the elements in the sample.

INAA offers excellent sensitivity, precision, and repeatability for most elements (excep-

tions include difficult-to-activate elements such as carbon and iron), and matrix effects are negligible. For these reasons, it is widely accepted as a standard reference method for elemental analysis of archaeological samples [19].

Neutrons and gamma rays have large penetration depths, so INAA is necessarily a bulk sampling technique; it is generally not possible to analyze distinct regions of a sample without first physically separating them. Furthermore, the difficulty of focusing neutron beams, as well as the long counting times required, preclude spatial analysis.

While INAA is, in principle, non-destructive (except for a small amount of transmutation and radiation damage), samples remain radioactive for years after activation. Thus, it is not common to activate entire objects; instead, a small portion ($\sim 1\,\mathrm{g}$) is removed with a drill or burr. This type of destructive sampling is not acceptable for some artifacts.

### 1.3.2 Microprobe Analysis/Ion Beam Analysis

Instead of photons, charged particles (electrons, protons, or other ions) can be used to illuminate samples. Tightly focused beams (often called microprobes) can achieve resolutions on the order of nanometers, although micron- or millimeter-sized beams are more typical. Microprobe beams are readily scanned across a sample surface, yielding 2D element maps in the same way as in XRFI. There are several variations on the basic technique:

### 1.3.3 Electron Microprobe Analysis (EPMA)

An incident beam of high energy (tens of kEV) electrons excites sample atoms, and the resulting characteristic X-rays are analyzed, as in XRF. Many scanning electron microscopes (SEMs) include an energy-dispersive X-ray detector (SEM-EDX) for this purpose, and dedicated instruments exist. Resolutions on the order of hundreds of nanometers are possible (limited by the interaction volume), but samples must be placed on a stage under vacuum, which severely limits sample dimensions and materials. Although EPMA itself is non-destructive, most samples require preparation, which can include embedding in resin,

polishing, and coating with a conductive film. Detection limits are on the order of 1000 ppm [16].

### 1.3.4 Particle-Induced X-Ray Emission (PIXE)

The sample is excited by a beam of ions (most commonly, protons), and as in the above techniques, the resulting X-ray spectrum is measured. Until recently, PIXE required the sample to be placed under high vacuum (due to the short mean free path of ions in the atmosphere), which severely limited the sample dimensions and material. However, it is possible to carry out microprobe analysis at atmospheric pressure – either in ambient air or helium – by using a beam "nozzle" fitted with an extremely thin window, placed very close to the sample, at the expense of some resolution and signal-to-noise ratio [10].

Unsurprisingly, since the techniques differ only in the exciting particles, PIXE and XRF provide similar information and suffer from similar drawbacks. Like XRF, PIXE typically results in little sample alteration, although radiation damage, sputtering, and heating can occur, especially at higher beam currents. Also like XRF, microprobe analysis suffers from matrix and geometric effects and so is a qualitative or semi-quantitative tool, unless great care in is taken in sample preparation and calibration. PIXE analysis is even more surface-sensitive than XRF: typical sampling depths are on the order of 100 micrometers [25]. Limited depth profiling can be accomplished by varying the beam energy or incidence angle [10]. Given the similarities between PIXE and SR-XRF, the choice between the two may be determined by the nearest available beamline.

A closely related technique, particle-induced gamma-ray emission (PIGE) measures the gamma ray spectrum from nuclear excitations. PIGE is most sensitive to light elements, which are difficult to quantify using PIXE or XRF, so these techniques can be complementary.

### 1.3.5 Laser-Ablation Mass Spectrometry (LA-MS)

This technique uses a pulsed laser to vaporize small craters from a sample surface; the vapor then undergoes elemental analysis in a mass spectrometer. By moving the sample or the laser focus, it is possible to obtain spatial profiles with a resolution of  10 micrometers [26–28]. LA-MS offers good sensitivity, with detection limits near 1 ppb [18], and accuracy [13], and can distinguish between isotopes. Ablation by successive laser pulses can generate depth profiles [14]. However, this technique is necessarily destructive (although the minor damage may be acceptable in some cases), limited to relatively small vacuum-compatible samples, and samples a smaller range of elements than XRF or PIXE.

### 1.3.6 Secondary Ion Mass Spectrometry (SIMS)

An energetic ion beam can sputter atoms from the surface of a sample, generating secondary ions which are detected by a mass spectrometer. The ion beam can be focused to spots as small as 50 nm [37]. Only the first few atomic layers are sputtered, which means that SIMS is practically non-destructive, and also that it is the most surface-sensitive of the techniques mentioned here. SIMS can achieve detection limits as low as 1 part per billion for a wide range of elements. However, ion sputtering is a complex process which depends on beam properties, the matrix, and the ions sputtered, so accuracies are limited to around 5% with careful calibration [44]. Sputtering can also be used to generate depth profiles of the first few nanometers of the surface [37]. Like LA-MS, SIMS must be performed under high vacuum.

### 1.3.7 Laser-Induced Breakdown Spectroscopy (LIBS)

This fairly recent technique uses a laser to vaporize a small portion of the sample surface into a plasma. It is reminiscent of LA-MS, but in this case, the atomic emission spectrum of the plasma is measured. LIBS can be performed in ambient air (or even under water), so there are no fundamental limits on sample size or composition, and the equipment can be made

portable. LIBS is slightly destructive, but in most cases the damage is microscopic [17]. Detection limits as low as 0.02 ppm have been reported for bright elements such as sodium, but more typical limits are on the order of 100-1000 ppm [46]. Matrix effects, and dependence on pulse energy and sample geometry, among other factors, limit accuracy to 1% under ideal conditions, and up to 60% in the field [12].

# Chapter 2

# Techniques

## 2.1 Sample Mounting

Artifacts come in a wide range of shapes and sizes, from tiny sherds to entire vases and stelae, and so we have developed a variety of mounting techniques. Often, these are ad-hoc, but there are methods which work well for large classes of objects.

The upper limit of sample size is set by the available clearance around the beam center. At F3, a permanent beam pipe runs roughly parallel to the beam, about 25 cm away in the horizontal (x) direction. The optical table lies approximately 35 cm below the beam (z direction) (though this distance could in principle be increased); a typical setup gives about 20 cm of space in the direction of the beam (y). Far more spacious beam lines exist; for instance, B16 at the Diamond Light Source could accommodate almost any conceivable portable artifact.

Archaeological artifacts are by definition irreplaceable, and are often extremely valuable. The foremost consideration in sample mounting is to minimize the risk of damage to the object. This generally precludes the use of adhesives or tapes directly in contact with the sample. Additionally, many artifacts are delicate, so clamping forces must be kept small. On the other hand, the sample must be held securely enough that it cannot shift during

stage motions: besides the obvious risk of falling, any motion of the sample relative to the stage will ruin the registration of the XRF data. To reduce this problem (among others), the motor controllers at F3 limit the stage motion to 1 mm/s, with gentle accelerations. (For additional insurance, we place a large foam pad beneath the stage, but none of the hundreds of samples we have examined has ever come loose.)

Care must be taken not to contaminate the sample surface, particularly if trace elements are of interest. We always handle samples with powder-free nitrile gloves. Any material that comes in contact with the sample should be carefully considered: for instance, many plastics, fabrics, and foams are treated with bromine-based flame retardants, and these can introduce bromine concentrations many orders of magnitude higher than background levels in samples. Fortunately, the same setup used for XRF on samples can be used to quickly check potential materials. XRF in air is not sensitive to elements lighter than sulfur, so pure polymers containing hydrogen, carbon, nitrogen, oxygen, fluorine, or silicon are generally suitable.

A related – but unavoidable – problem is that many artifacts have less-than-perfect (and often unknown) conservation histories. It is difficult to determine how the elemental makeup of an object has been altered since its creation. Aggressive cleaning can leach or introduce elements of interest: we have known anthropologists to casually rinse sherds under unfiltered tap water.

After safety, the next goal is to mount the object in a way that allows the desired portion to be imaged. This is not always straightforward – for example, one may wish to scan the entire outer surface of a sherd, in which case no clamps or bands can be placed in front of it. The entire region must be turned towards both the detector and the beam, and nothing can shadow it from either.

The sample stage at F3 is an aluminum plate, similar to an optical breadboard, 8.5" (216 mm) wide by 12" (305 mm) high, with 1/4-20 tapped holes on a 1" (25.4 mm) grid. These holes make it easy to attach a large variety of brackets, posts, and clamps. Many

off-the-shelf components are available from optical parts suppliers (e.g. Thorlabs), and we have fabricated custom attachments as well.

The simplest way to mount large objects, such as tablets or vases, is to set them on a padded shelf or L-bracket. The low accelerations of the stage allow the object to stand mostly under its own weight, and a few small clamps or plastic bands gently hold it back against the vertical stage. We always try to set up redundant restraints, so that a single-point failure will not allow the object to fall.

The ideal mount for vases, pots, and other solids of revolution would be a stepper-motor-controlled rotary table. This would allow nearly the entire surface to be scanned while maintaining the same angles of incidence for the beam and detector. Unfortunately, these are not commonly available at beam lines.

Smaller objects can be held against the breadboard (usually with a piece of foam interposed) using miniature optical post clamps. These are tightened by finger pressure, rather than by a screw, so clamping force is easier to control. Usually four clamps are sufficient to stabilize a sample. However, it can be difficult to arrange the clamps so that they do not get in the way.

We have fabricated custom vises (figure vise). These have a dovetail slide which can be screwed to the breadboard in at any angle, and sliding plastic jaws with several holes for posts. The posts are covered by rubber tubing. This system makes it easy to arrange the posts to clamp even irregularly shaped objects by their edges, leaving the entire face clear for scanning. The compliance and high friction coefficient of the rubber mean that only a small clamping force is needed to secure an object. We have found this to be the best way to mount individual sherds.

### 2.1.1 High-Throughput Scanning

Due to the speed of synchrotron-based XRFI, we have found that a large fraction of available beam time (up to 50%) can be spent in changing samples, especially when many small objects

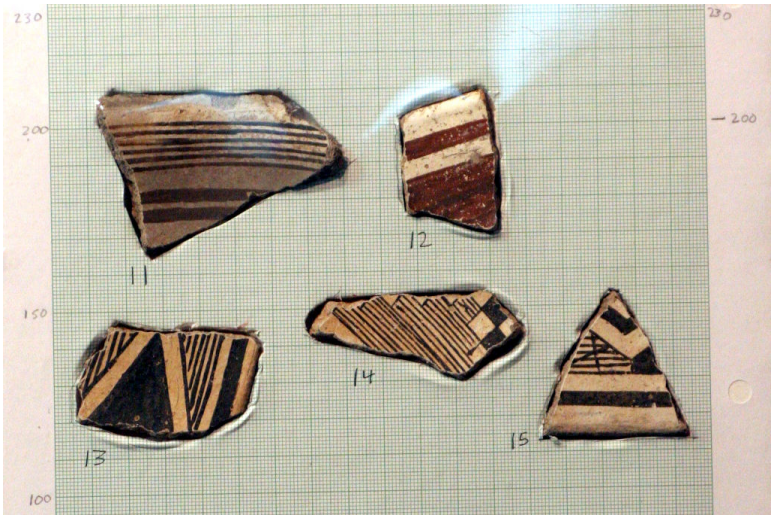


Figure 2.1: Samples are placed into cutouts in a soft foam-core board. A thin plastic shrink film holds the samples in place. The millimeter grid allows for rapid and accurate scan alignment and registration.

are to be scanned. It can take from several minutes to half an hour to open the hutch, remove the previous sample, mount a new sample, and align the corners of the scan region. It is often desirable to analyze large collections of objects, for comparison, for clustering, or to allow a more integrative analysis. Therefore, we have developed techniques which greatly reduce overhead from mounting samples and aligning scans.

### 2.1.2 Foam Mounting

We have adopted a mounting system based on rigid foam sheets (extruded polystyrene works well) (Fig. 2.1). A cavity in the shape of a sample, and slightly larger, is carved out using a knife. The sample fits snugly (but not tightly) into the cavity, protruding a couple millimeters above the surface of the foam. Many small samples can be mounted on one 200 mm x 250 mm sheet. Next, a piece of thin polyolefin shrink film is wrapped around the foam, covering all sides, and secured with tape on the back. Finally, the film is shrunk in place with a common hair dryer. The result is a transparent, wrinkle-free film which gently but securely holds the objects in place.

Because the film is so thin (less than 25 µm) and has a shrink temperature of less than

100 °C, the film contracts very quickly, with minimal heating of the samples. If this slight heating is a concern, the film can be stretched by hand, but we feel that heat-shrinking is one of the most delicate possible ways of retaining objects; with a thin film, and the shallow angle of pull, the force of applied to the sample is extremely small.

The film contains only hydrogen and carbon, so it generates no interfering fluorescence, and its X-ray absorption in the energy range of interest is much less than that of the air between the sample and detector (and is easily accounted for in the analysis). Nevertheless, if this absorption is unacceptable, it is possible to cut windows into the film to expose regions of interest. The benefit of a continuous film is that the entire surface of the object can be imaged with no shadowing or artifacts from the mounting apparatus.

Mounting samples in this way is somewhat time consuming, but it has the great advantage that it can be done in advance. Clamping the entire foam sheet to the stage takes less than a minute. While one batch of samples is being scanned, the next can be mounted.

### 2.1.3 Automated Alignment

To avoid wasting time scanning uninteresting or empty areas, it is necessary to locate the rectangular scan regions fairly precisely (within 1 mm or so). The usual way of doing this is to drive the stage around, moving the crosshairs to each of the four corners and recording their coordinates. It often takes some trial and error to ensure that the rectangle is as small as possible but still includes all the features of interest. The stage motion is slow; thus, so is the procedure, especially if there are many regions to define.

We have developed a process which dovetails nicely with the above foam mounting system: before the cavities are excavated, a sheet of millimeter grid paper is glued to the surface. After the samples are mounted, enough of the grid remains visible to measure coordinates. In this way, the scan regions can be defined ahead of time. When the foam board is mounted on the stage, all that remains is to register it with the stage's x and z coordinates. This can be done by locating two points on the grid, or by using registration marks on the stage.

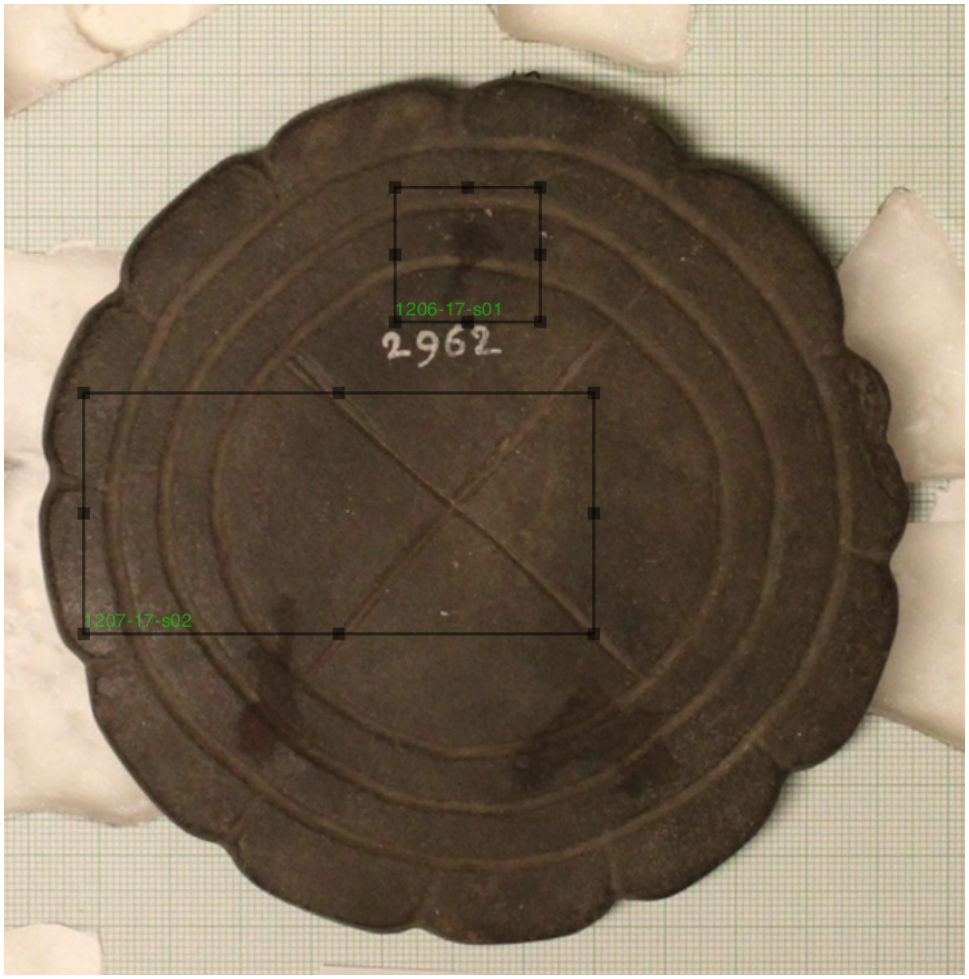


Figure 2.2: Using custom software, scan areas are drawn onto a photograph of the sample. The software rectifies the image and translates the rectangles into stage coordinates.

As an additional refinement, we have written software to automate this process. First, the foam board with the mounted samples is photographed with a digital camera. To minimize errors due to lens distortion and the topography of the samples, we use a lens with a long focal length. Next, the sample-space 2D coordinates of four points on the grid are used to rectify the digital image; that is, a matrix is computed which transforms between the pixel coordinates of the image and the 2D coordinates in millimeters on the mounting board. The image is corrected for perspective and distance.

Then, using an interface similar to a graphics editor, rectangles are drawn on the image to define scan regions (Fig. 2.2). A resolution can be specified for each region. The software calculates the time which will required for each scan, as well as the total time (this is invaluable in allocating time efficiently among samples and scans). Finally, the program generates a SPEC macro script which carries out all of the scans.

We have found this system to be immensely helpful: it greatly reduces overhead; it allows for efficient planning; and it all but eliminates human error in setup. Furthermore, it automatically generates a detailed record of exactly what has been scanned, along with images of the scan regions. Prior to these innovations, it was possible to scan a couple dozen sherds during a week-long run. Since then, we have scanned over one hundred objects in a week. The limit is now set by the detector count rate and stage speed, not sample handling.

### 2.1.4 Delicate Samples

Some objects require special handling. Exceptionally fragile items, or those with sharp protrusions (such as glass fragments), cannot be safely mounted in foam; the protrusions tend to catch. For these, we use a modified version of the above procedure. The objects are carefully slipped into small polyester or polyolefin bags (polyethylene is too sticky), and the bags are taped to the foam board. Samples mounted in this way are more likely to shift slightly during scans.

To image the cross-sections of delicate pieces (e.g. glass sherds), the objects are set on a

soft, but smooth, horizontal shelf on the stage, with the edge to be scanned nearly flush with the edge of the shelf. For security, the sample is surrounded (but not touched) by a "fence" of foam pieces. The sample's own weight is sufficient to keep it in place during scans.

In some cases, it is possible for museum conservators to pack objects in a way that allows them to be scanned without removing them from their packages. For instance, an object can be cradled in a plastic-lined foam cutout and covered with a thin plastic film.

# Chapter 3

# The Surface Orientation Effect

Analysis of XRFI data is most straightforward for objects with flat surfaces. For objects with surface relief, such as vases or tablets with incised letters [23, 24], variations in local surface orientation relative to the incident X-ray beam modulate the intensity of X-ray fluorescence received at the detector [3]. These geometry-related intensity modulations cannot easily be distinguished from those due to variations in sample composition. The problem of quantitative X-ray fluorescence (XRF) analysis of objects with arbitrary geometries is difficult and often ill-posed [42]. Computationally-intensive Monte Carlo methods [31, 39–41] have been successfully applied in some cases.

Here, we derive simple expressions for the variation of fluorescence intensity with surface orientation, and discuss a procedure to correct fluorescence maps for the effects of surface relief. Although the necessary assumptions about sample surface relief and composition and about measurement geometry are fairly restrictive, the analysis is still useful for many real-world samples, as we will illustrate.

## 3.1 Variation of detected fluorescence intensity with surface and detector angles

To analyze the effect of surface relief, we make the following simplifying assumptions:

1. Variations in the surface relief and sample composition are small on the scales of the incident X-ray beam width ($\sim 1\,\mu\text{m} - 1\,\text{mm}$) and penetration depth ($\sim 500\,\mu\text{m}$), respectively.

2. The detector is far from the surface, so that differences in path length and angle from various points in the X-ray illuminated and fluorescing sample volume to the detector can be neglected, and integration over the detector's solid angle is unnecessary.

3. The sample's surface relief and the sample and detector orientations are such that there is an unobstructed path from the incident beam's interaction point to the detector for all points on the sample surface. I.e., the path to the detector from one point on the sample surface is not blocked by another part of the surface.

4. There is no secondary fluorescence.

As illustrated in Fig. 3.1, we choose coordinates so that the beam intersects the surface at the origin, and define unit vectors $\hat{\mathbf{b}}$ along the incident X-ray beam direction, $\hat{\mathbf{n}}$ along the surface normal at the point of interaction with the X-ray beam (lying at some distance beneath the sample surface along the incident beam path), and $\hat{\mathbf{d}}$ from the interaction point to the detector.

The intensity of the fluorescence signal at the detector is

$$I = \lambda \int_0^\infty e^{-\mu_i s_i} e^{-\mu_f s_f}\, ds_i \tag{3.1}$$

where $\lambda$ is a constant involving the fluorescence yield and detector solid angle; $\mu_i = \mu(E_i)$ $[\mu_f = \mu(E_f)]$ is the sample attenuation coefficient at the incident [fluorescent] energy, and $s_i$

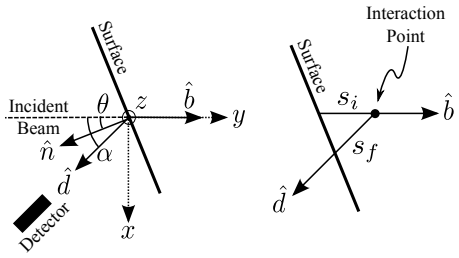


Figure 3.1: Measurement geometry for calculation of variation of XRF signal intensity with surface orientation. Left: $\hat{\mathbf{b}}$, $\hat{\mathbf{n}}$, and $\hat{\mathbf{d}}$ are the incident beam direction, the surface normal direction, and the direction from the interaction point to the detector. The rotations of $\hat{\mathbf{n}}$ and $\hat{\mathbf{d}}$ around the $z$ axis (with respect to $-\hat{\mathbf{b}}$) are given by $\theta$ and $\alpha$, respectively. The detector lies in the $xy$ plane. Right: Expanded view of the region around the interaction point. The incident beam travels a distance $s_i$ from the surface to the interaction point, and the fluorescent photons travel a distance $s_f$ from the interaction point to the surface.

$[s_f]$ is the length of the line from the sample surface to the interaction point along the beam direction [detector direction].

To determine $s_f$, note that the interaction point is located at $s_i\hat{\mathbf{b}}$, so the ray from the interaction point to the detector is given by $s_i\hat{\mathbf{b}} + s\,\hat{\mathbf{d}}$, for $s > 0$. The equation of the surface is $\hat{\mathbf{n}} \cdot \mathbf{r} = 0$, so the outgoing ray intersects the surface at

$$(s_i\hat{\mathbf{b}} + s_f\hat{\mathbf{d}}) \cdot \hat{\mathbf{n}} = 0.$$

Thus,

$$s_f = -\frac{\hat{\mathbf{b}} \cdot \hat{\mathbf{n}}}{\hat{\mathbf{d}} \cdot \hat{\mathbf{n}}} s_i \equiv k s_i \,^{1} \tag{3.2}$$

where $k$ is a geometrical factor. Then

$$\begin{aligned} I &= \lambda \int_0^\infty \exp\left[-(\mu_i + k\mu_f)s_i\right] ds_i \\ &= \frac{\lambda}{\mu_i + k\mu_f}. \end{aligned} \tag{3.3}$$

[1] $s_f$ is negative or fails to exist when the surface is angled away from the detector.

In our coordinate system, the beam points along the $+y$ direction ($\hat{\mathbf{b}} = \hat{\mathbf{y}}$), and the detector lies in the $xy$ (horizontal) plane, making an angle $\alpha$ with $-\hat{\mathbf{y}}$. Then, if $\hat{\mathbf{n}} = (n_x, n_y, n_z)$, and $\hat{\mathbf{d}} = (\sin\alpha, -\cos\alpha, 0)$,

$$\begin{aligned} k = -\frac{\hat{\mathbf{b}} \cdot \hat{\mathbf{n}}}{\hat{\mathbf{d}} \cdot \hat{\mathbf{n}}} &= \frac{-n_y}{n_x \sin\alpha - n_y \cos\alpha} \\ &= (\cos\alpha + \tan\theta \sin\alpha)^{-1} \end{aligned} \tag{3.4}$$

where $\theta$ is the rotation of the surface normal around the $z$ axis; $\theta = 0$ for a surface parallel to the $x$-$z$ plane. Finally, we have

$$I(\theta) \propto \frac{1}{1 + (\mu_f/\mu_i)(\cos\alpha + \tan\theta \sin\alpha)^{-1}}. \tag{3.5}$$

Figure 3.3 shows $I(\theta)$ versus surface orientation angle $\theta$ at several detector angles $\alpha$ calculated using Eq. 3.5 and $\mu_f/\mu_i = 20$ (typical, e.g., for potassium fluorescence in a calcite matrix, with an incident energy of 16 keV).

The above calculation leads to several observations. One, changes in the surface orientation $\theta$ result in changes in the detected fluorescence intensity and thus, if no correction is performed, in *apparent* changes in elemental composition (Fig. 3.4). The magnitude of this intensity variation with $\theta$ increases with increasing $\mu_f/\mu_i$, and so is often most apparent for low-$Z$ elements, which have relatively small mass absorption coefficients $\mu_i$.

Two, under the given approximations, rotations of the surface normal out of the $xy$ plane (within $\pm 90°$) do not change the detected fluorescence intensity. Thus, whenever possible, objects should be mounted so that their dominant surface curvature runs perpendicular to the detector–incident beam ($xy$) plane. For instance, mounting a cylindrical sample with its axis in the $xy$ plane avoids position-dependent modulation of the fluorescence intensities.

Finally, the angle effect vanishes as the detector position approaches the incident beam, and is maximal when the detector is perpendicular to the beam. For polarized incident

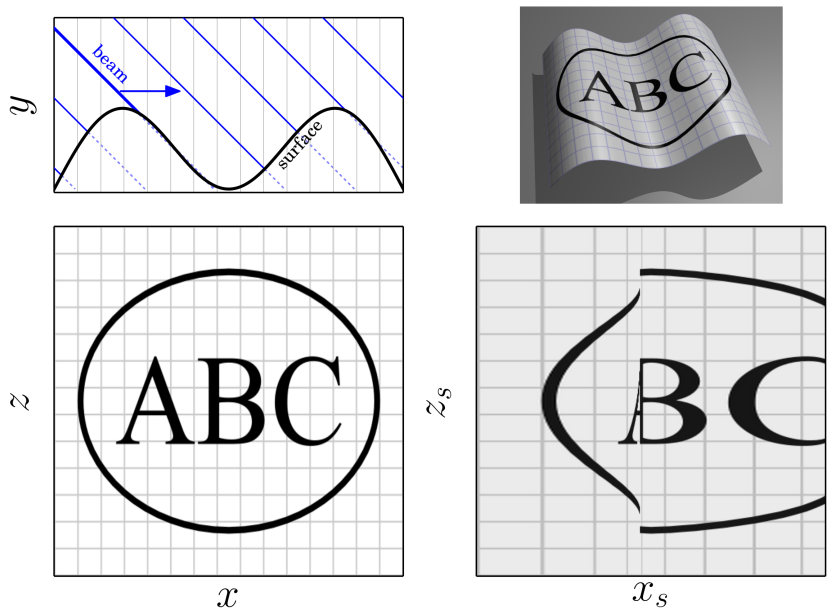


Figure 3.2: Distortion of a scan map with the incident beam at an angle of 45° to the sample stage. Upper right: Hypothetical curved sample with a design on its surface. Lower left: Un-distorted map of the design. Upper left: Cross-sectional view, showing the intersection of the beam with the sample surface. The beam is swept from left to right (the other scan dimension is not shown). Lower right: Resulting distorted scan map. Note the "folding" which occurs where the surface tangent angle exceeds the beam incidence angle.

radiation (e.g., synchrotron radiation), Compton scattering is greatly reduced when the detector is perpendicular to the beam, in the plane of polarization) [15]. To minimize Compton background, typical XRF configurations place the the detector at $\alpha = 90°$ and the sample normal at $\theta = 45°$. However, for samples with appreciable surface relief, a better approach is to orient the sample's "mean" normal in the $-\hat{\mathbf{y}}$ direction, and to set the detector at as small an angle $\alpha$ as practicable (typically about 45°). The very high counting rates possible using modern detectors make the Compton background less problematic.

Orienting the sample and translation stage perpendicular to the beam solves another problem, too: if the stage is at any other angle, sample topography will vary the interaction point of the beam in stage $xz$ coordinates, and therefore in the *image* coordinates 3.2. This distorts the images—sometimes discontinuously—and can lead to difficulty in registering the XRFI scan maps with actual features on the sample.

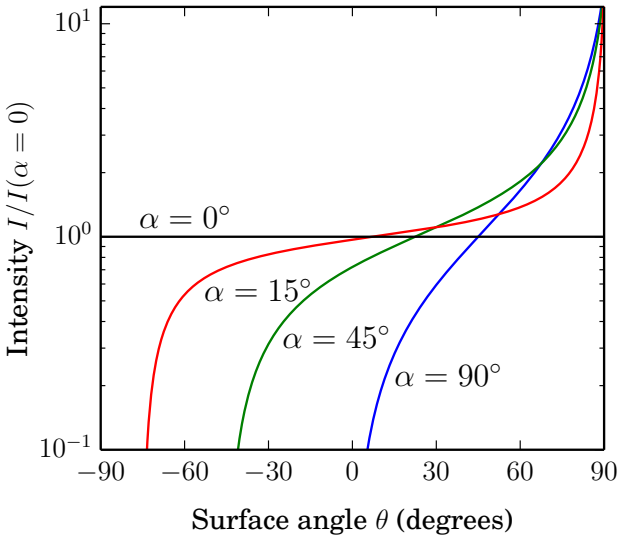


Figure 3.3: Variation of detected fluorescence intensity with surface angle $\theta$, as given by Eq. 3.5, with $\mu_f/\mu_i = 20$ and four detector angles $\alpha$

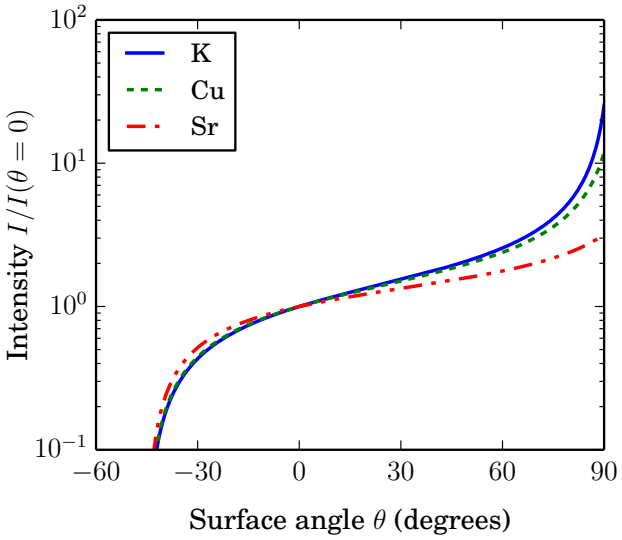


Figure 3.4: Variation of detected fluorescence intensity with surface angle $\theta$ for the $\mathrm{K} - K_{\alpha 1}$, $\mathrm{Cu} - K_{\alpha 1}$, and $\mathrm{Sr} - K_{\alpha 1}$ lines, in a $CaCO_3$ matrix, with incident beam energy 16.5 keV and detector angle $\alpha = 45°$

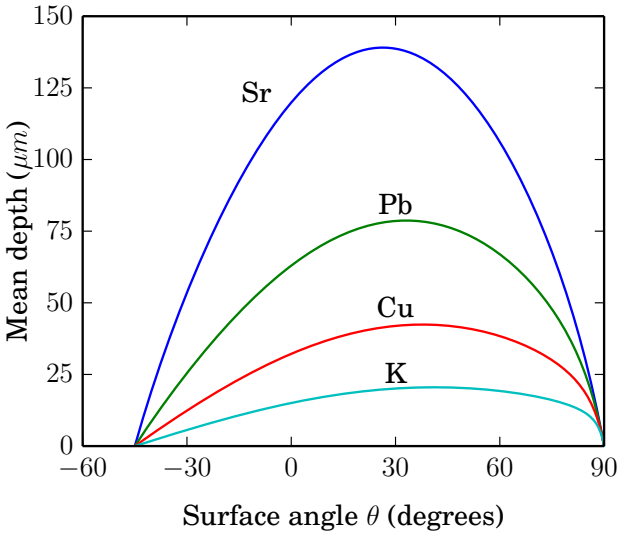


Figure 3.5: Mean depth from which detected fluorescent photons originate, for the $\mathrm{K}-K_{\alpha 1}$, $\mathrm{Cu}-K_{\alpha 1}$, $\mathrm{Pb}-L_{\alpha 1}$, and $\mathrm{Sr}-K_{\alpha 1}$ lines, in a $CaCO_3$ matrix, with incident beam energy 16.5 keV, and detector angle $\alpha = 45°$

The surface and detector angles also affect the penetration depth of the X-rays, and therefore the surface sensitivity of the measurement. From Eq. 3.3, we can find the mean depth at which the recorded fluorescent photons are generated:

$$\begin{aligned} \bar{d} &= \frac{\int_0^\infty \cos(\theta) s_i \exp\left[-(\mu_i + k\mu_f)s_i\right] ds_i}{\int_0^\infty \exp\left[-(\mu_i + k\mu_f)s_i\right] ds_i} \\ &= \frac{\cos\theta}{\mu_i + \mu_f(\cos\alpha + \tan\theta \sin\alpha)^{-1}}. \end{aligned} \tag{3.6}$$

Figure 3.5 shows the variation in penetration depth with angle in a typical calcite sample. This effect further complicates analysis of XRFI data from samples with relief.

## 3.2 Correction of XRFI maps for the effects of surface relief

If the approximate matrix of a sample is known and is spatially uniform, and the non-matrix elements are present in trace concentrations, then good approximations to $\mu(E)$ can be calculated. In that case, the only undetermined variable in Eq. 3.5 is $\theta$. Therefore, if $\theta(x, z)$ (where $x, z$ are coordinates on the sample surface) can be determined, the XRFI data can be corrected for surface relief, at least to the extent that the approximations leading to Eq. 3.5 hold.

The most straightforward way to find $\theta(x, z)$ is to spatially profile the surface of the object, e.g., with a laser displacement sensor or via stereo photogrammetry. The 3D profile must then be registered with the XRFI data. Profiling may not always be feasible due to equipment and time constraints. This raises the question: is it possible to correct for angle based on the fluorescence data alone? Often, the matrix of a sample contains one XRF-visible element that is present in roughly uniform and high concentration over the entire surface—for instance, calcium in marble, limestone, or gypsum. In this case, we can assume that the reference element is, in fact, uniformly distributed, and use the intensity of one of its fluorescence lines to invert Eq. 3.5 and find $\theta(x, z)$. Eq. 3.5 can then be used to correct the XRFI maps for each trace element.

We have found the following inversion and correction procedure to be effective:

1. Given the matrix composition, compute the absorption coefficient $\mu(E)$ for the energy range of interest. We use the data in [8] and [30].

2. Choose a single fluorescence peak from the fitted spectra, for a major matrix element that is expected to be uniformly distributed (in this case, Ca-K$\alpha$).

3. Let $I(x, z)$ be the intensity (i.e. number of counts) of this peak at points $x, z$ in the

scan; $I_0$ the median of $I$ in a relatively flat region of the sample; and $k_0$ the geometric constant (according to Eq. 3.4) for this region.

4. Compute

$$\begin{aligned} \gamma_0 &= I_0(\mu_i + k_0\mu_f) \\ k(x,z) &= [\gamma_0/I(x,y) - \mu_i]/\mu_f \end{aligned} \tag{3.7}$$

5. Invert Eq. 3.4 to find $\theta$.

Next, with $k(x,z)$ determined by Eq. 3.7, calculate a correction factor as a function of the energy E of the fluorescence:

$$C(E,x,z) = \frac{\mu_i + k(x,z)\mu(E)}{\mu_i + k_0\mu(E)} \tag{3.8}$$

Finally, we apply this correction to the XRF spectrum at each pixel of the scan, re-fit the peaks in the corrected spectra, and then generate corrected XRFI maps for each element of interest.

## 3.3 Application to an incised tablet

As an example of the application of the above inversion and correction procedure, we examined a gypsum ($CaSO_4 \cdot 2H_2O$) tablet from what is now Iraq, dated ca. 1000 BCE, shown in Figure 3.6. The tablet is deeply incised with cuneiform figures. XRFI measurements were performed at beamline F3 of the Cornell High Energy Synchrotron Source (CHESS), using an incident beam energy of 17.0 keV, a stage angle of 90°, and a detector angle of 45°. The detector was a four-element Vortex ME4 silicon drift detector from SII Nanotechnology.


Figure 3.6: Photograph of deeply incised gypsum tablet dated ca. 1000 BCE from what is now Iraq (Harvard Semitic Museum no. 1897.1.1), with scan region examined in Figs. 3.7 through 3.9 outlined in white. Image adjusted to enhance brightness and contrast.

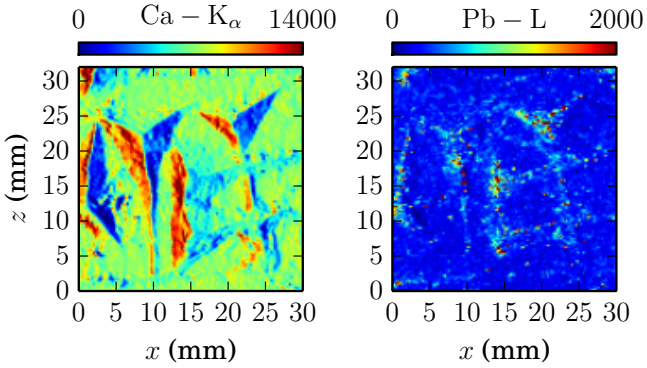


Figure 3.7: Uncorrected Ca-K$\alpha$ and Pb-L fluorescence maps for the tablet in Fig. 3.6. Ca is expected to be roughly uniformly distributed within the tablet, but the Ca fluorescence intensity shows large variations, especially in incised regions, due to variations in surface orientation. The same effect complicates the interpretation of the map for Pb, a trace element whose concentration might be expected to correlate with incision. Scan taken with detector angle $\alpha = 45°$, stage angle $\theta_0 = 0°$, beam energy $E_i = 17.0\,\mathrm{keV}$, beam size 300 µm, and step size 250 µm.

Fluorescence spectra were fit using the PyMCA software library [36]. Figure 3.7 shows the uncorrected Ca-K$_\alpha$ and Pb-L$_\alpha$ fluorescence maps for the outlined scan region in Fig. 3.6.

Calcium should be roughly uniformly distributed throughout the tablet, but the Ca map shows pronounced intensity variations that correlate with variations in surface angle. The detector was located to the right of the image, leading to apparently enhanced calcium fluorescence from the left-hand sides of the incisions.

The Pb map appears to indicate larger Pb concentrations in the incisions. However, it is not clear whether this is a geometric artifact since, like Ca, Pb fluorescence is stronger on the left-hand sides of the incisions. This tablet illustrates typical complications in interpreting fluorescence maps from non-planar objects.

Applying the inversion procedure outlined above, using the Ca-K$\alpha$ peak at 3.69 keV as the reference peak, yields the map of surface orientation angle $\theta$ shown at top of Fig. 3.8. Figure 3.8, bottom left, shows a rendering of the surface with angles as shown at top, shaded as if illuminated by a light from the approximate position of the detector; the luminance $L$ was computed using Lambertian shading, with $L \propto \cos(\alpha - \theta)$. Interestingly, this shows

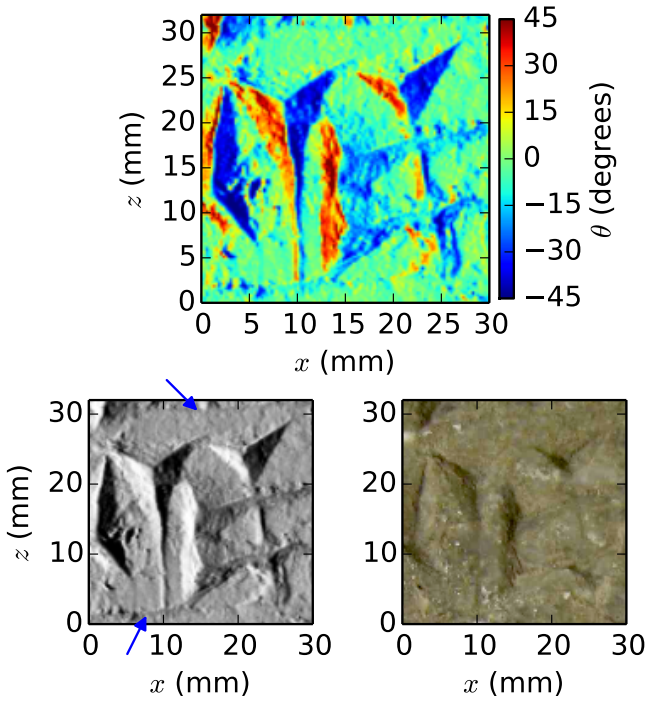


Figure 3.8: Top: Map of surface angle $\theta$ computed from the Ca $-$ K$\alpha$ fluorescence map of Fig. 3.7. Bottom left: Rendering of surface of the scanned area, computed from the surface angle map above and shaded as if obliquely illuminated from the right side by a light source. The reconstruction gives a clear and detailed picture of the surface relief, including the fine horizontal rulings at the top and bottom (marked by arrows). Bottom right: Photograph of the scanned area, adjusted to enhance contrast and brightness.

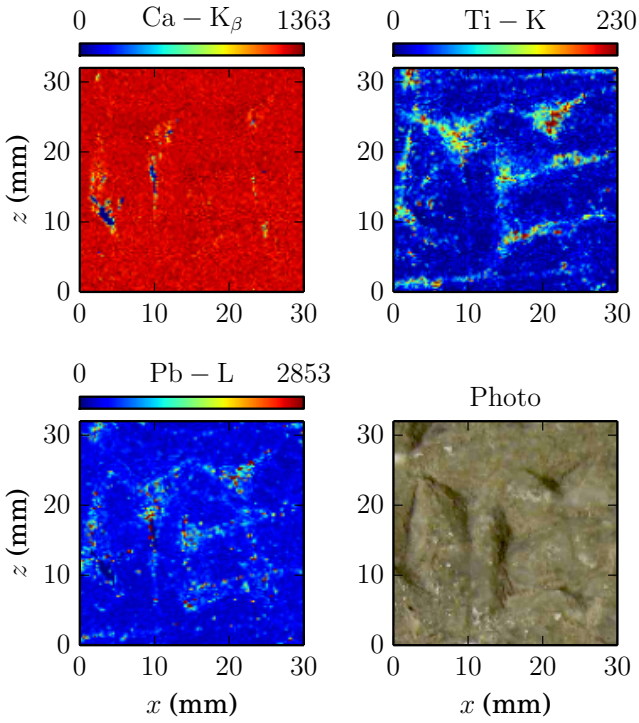


Figure 3.9: Angle-corrected fluorescence maps for $\mathrm{Ca}-\mathrm{K}\beta$, Pb-L, and Ti-K. As expected, the Ca map is nearly uniform (except where the angle exceeds $-45°$). The corrected Pb and Ti maps show an increased concentration of these elements in the incised areas.

the pattern of relief more clearly than the optical photograph shown at bottom right; and it is surprisingly accurate, considering the restrictive approximations under which it was computed.

Using the surface orientation map in Fig.3.8, the XRFI maps can now be corrected. We first check the corrected $\mathrm{Ca}-\mathrm{K}\beta$ map (4.01 keV) map. This $\mathrm{Ca}-\mathrm{K}\beta$ peak was measured and fitted independently of the $\mathrm{Ca}-\mathrm{K}\alpha$ peak, so if our model is valid, the corrected $\mathrm{Ca}-\mathrm{K}\beta$ map shown at upper left in Fig. 3.9 should be nearly flat. Indeed, it is, aside from small regions where the surface was at an angle $\theta < -\alpha = -45°$ and so was blocked from the detector's view.

Figure 3.9 also shows corrected Pb and Ti fluorescence maps. In contrast to Fig. 3.7, Pb now appears evenly distributed between the left and right sides of the incisions. We are

confident, therefore, that there actually is an increased concentration of Pb (and also Ti), within the incised features. These trace elements could have been introduced from the tools used to carve the figures (titanium has been associated with bronze-age tin production [1]); paint used to decorate the tablet; or contaminants which, e.g., have been scrubbed from the field of the tablet but not from the protected valleys.

We emphasize that in calculating the corrections, we have assumed that the sample composition normal to the average surface plane is uniform within the X-ray attenuation length (roughly 600 µm). In the limiting case where all trace elements were concentrated within a very thin surface layer (i.e., much thinner than the attenuation length), there would be a smaller correction to the trace element concentrations, proportional to $1/\cos\gamma$, where $\gamma$ is the angle between the surface normal and $-\hat{\mathbf{b}}$. Applying this latter correction produced maps that were qualitatively similar to the uncorrected ones. In either case, there is evidently an increased concentration of Pb and Ti in the incisions.

Also note that our correction procedure assumes that elements of interest do not affect the detected fluorescence from the matrix reference element. For example, a thick Pb surface layer (e.g., from a pigment) would absorb and therefore mask the Ca fluorescence that we use as a reference, and Eq. 3.7 would then underestimate the surface angle. For the specimen considered here, there is no visual or XRF evidence of such layers; the elements of interest are present in trace concentrations.

## 3.4 Conclusions

We have derived simple expressions for the modulation of X-ray fluorescence intensity by surface orientation relative to the incident beam, and we have demonstrated a correction procedure applicable to trace element maps of such samples. The analysis assumes that the major elemental constituents of the matrix are homogeneous throughout the sample, that the surface is locally flat on the scale of the X-ray beam, and that absorption of matrix

element fluorescence by trace element layers can be neglected. These assumptions should be approximately valid for a wide range of samples.

A key advantage of this method is its simplicity, both in the requisite experimental apparatus (a single detector, and no separate apparatus for determining surface topography) and in its analysis. However, the estimates of surface angles might be improved by using multiple detectors, e.g., positioned in pairs on opposite sides of the beam. One approach to dual-detector topography correction was reported in [35]. However, that work simply used the sum and difference of the maps from the two detectors, and, as Eq. 3.5 shows, the variation of fluorescence intensity with angle is not linear, even in the case of a flat, homogeneous surface. Fitting Eq. 3.7 to fluorescence maps from multiple detectors would likely yield better corrections, and would reduce the occurrence of "blind spots" where the detector's view is blocked by another part of the sample. Finally, the recently developed highly parallel annular detectors [29] raise an intriguing possibility: Analyzed using methods similar to those outlined here, a single scan might provide extremely detailed reconstructions of both the composition and geometry of a sample.

# Chapter 4

# De-colored Nuzi Glass

## 4.1 Abstract

We have used synchrotron-based X-ray fluorescence imaging to analyze de-colored and weathered fragments of ancient Mesopotamian glass. We have developed effective techniques, using clustering and classification algorithms, to recover the original colors and patterns of decoration, and we have applied these methods to a set of samples.

## 4.2 Introduction

We have applied XRFI to fifteen fragments of glass from the ancient Meso-potamian city of Nuzi (located in present-day Iraq), all from the collection of the Harvard Semitic Museum. The age of these has been estimated, using textual and archaeological evidence, to be approximately 3500 years [6]. Most of the fragments we have analyzed are from colorful core-formed vessels. To create these, an artisan shaped a paste of glass-forming material and binder around a friable core (e.g. of clay and sand). Trails of glass in contrasting colors were applied hot, then dragged with a point to form scalloped patterns; finally, these were marvered flush with the surrounding surface.

All of the samples in this study have been heavily altered: the surfaces are weathered,

and the colors have faded, often so much that the original colors are visually unrecognizable. It seemed possible, however, that at least some of the colorant elements remained, albeit, perhaps, in different chemical states. Thus, we hoped that XRFI might be able to reveal the original colors.

Furthermore, the analytical work on these artifacts has been limited to date, so we sought to provide insight into their composition, construction, and state of alteration.

These artifacts are very well suited to XRFI: they have mostly smooth, gently curved surfaces, and relatively little surface contamination or encrustation. They are locally homogeneous (on the scale of analysis used, $\sim 100\,\mu m$), and are not layered. These characteristics greatly simplify the analysis of XRFI data.

## 4.3 Previous Analyses

The earliest analyses of glass from the Nuzi site were by R.H. Brill and coworkers, who used X-Ray diffraction (XRD), electron microprobe, and others to determine the mean compositions of several samples and colorants [5–7]. Brill found that the blue glasses were colored with copper, but not (unlike similar Egyptian glasses) with cobalt; yellow with lead; and antimony was the typical opacifier. Lead isotope analysis indicated a Mesopotamian origin for these samples.

Shortland and coworkers used wavelength-dispersive (WDS) X-Ray spectrometry [32] and laser-ablation inductively-coupled mass spectrometry (LA-ICPMS) [33,34] to determine elemental compositions. Ancient Mesopotamian and Egyptian glasses have been found to contain copper, lead, and iron as colorants, and calcium and lead antimonate as opacifiers. Table 4.1 summarizes the principal colorants found in these glasses.

| Elements | Color |
|---|---|
| Ca + Sb | White |
| Ca + Cu + Sb | Opaque turquoise |
| Cu | Blue |
| Cu + Pb + Sb | Opaque green |
| Mn | Black, purple |
| Pb + Sb | Yellow |
| Fe | Transparent green |

Table 4.1: Colorants

## 4.4 Experimental Methods

The artifacts were imaged at beamline F3 at CHESS, using procedures described in the previous chapter. Typically, a 100 µm to 250 µm, 6.5 keV beam was used, with integration times of approximately 0.1 s per pixel.

A practical note: many of these fragments are extremely fragile. The leaching of silica from the glass matrix has left them in a very friable state; thus, we found it best to handle them as little as practicable. Whenever possible, we mounted the pieces using the plastic bag technique. Additionally, the fragments appear to be sensitive to the ambient relative humidity: changes in the hydration state of the weathering products leads to expansion or contraction of the matrix and can make the pieces more susceptible to fracturing.

For each piece, the majority of the outer surface was imaged. In some cases, additional scans were made of the cross section and inner surface.

## 4.5 Analysis

All of the fragments studied show high elemental contrast between regions of different original glass color. For reasons outlined in the preceding chapter, we did not attempt an analysis of absolute element concentrations. Although figures are reported below, they should be taken as order-of-magnitude estimates, at best. Far better determined are the *relative* concentrations of elements among different regions of each sample, and even among samples.


Figure 4.1: Sample 6

The elements used as colorants are present in low concentrations ($< 3\%$) [5–7] in a fairly uniform silicate matrix, so we expect matrix effects to be consistent. There is some geometrical variation due to the curvature of the fragments, but, since the pieces are smooth, this is distributed on a scale that is large compared to the decoration.

Because of the large volume of data, we will present the analysis of just one typical fragment. The others were carried out along similar lines, and the techniques should be broadly applicable. A table of sample numbers and museum numbers is given in Appendix 1.

### 4.5.1 Sample 6

This fragment (Fig. 4.1) shows moderately heavy weathering and what appears to be a black contaminant on the surface and in pits left by corrosion. At least five bands of trailed decoration are visible; the colors of these differ slightly from that of the surrounding material, but the colors are faint and indistinct. It is not obvious from a visual examination what the original colors were. Due to the weathering and contamination, even the borders of some

of the bands are unclear. However, as we will see, enough traces of color remain to give us some confidence in the results of the XRF analysis.

This artifact has fractured further since the museum photograph in figure 4.1 was taken. We scanned the largest two of these sub-fragments (referred to as 6a and 6b), which comprise most of the area of the original piece. They are, respectively, the lower right and upper left sections of the sample. The fracture line between these two can be seen faintly in the photograph.

#### Element Maps

Figure 4.2 shows the element maps most useful for discriminating between colors in this sample. These correspond loosely to the colorant elements described by Shortland [34]. As in previous analyses of glass from this site, no significant cobalt was detected. Unfortunately, the calcium and manganese signals were dominated by patches of surface contamination. These elements have low-energy fluorescence lines (3.7 keV for Ca-K$\alpha$ and 5.9 keV for Mn-K$\alpha$), and correspondingly short penetration depths. However, we have used strontium as a proxy for calcium. The penetration depth of strontium fluorescence (K$\alpha$ = 14.1 keV) is far greater, so the strontium element maps are less surface-sensitive. Since strontium is isoelectronic with calcium and has a similar ionic radius, it substitutes for calcium in many minerals, and glasses incorporating these [4]. Although the Ca/Sr ratio certainly varies among glasses, we expect it to be consistent for a particular batch of glass.

In the following, we refer to the collection of all element maps for a particular scan as an image, by analogy with a more typical multi-color photographic image.[1]

### 4.5.2 Pre-processing

As described in chapter 1, we use the algorithms implemented in PyMCA [36] to fit peaks in the raw spectra and estimate the mass fraction of each element. Since the scan regions are

[1] A typical digital image has three channels: red, green, and blue. Here, the $n$ channels are the concentrations of the $n$ elements analyzed.

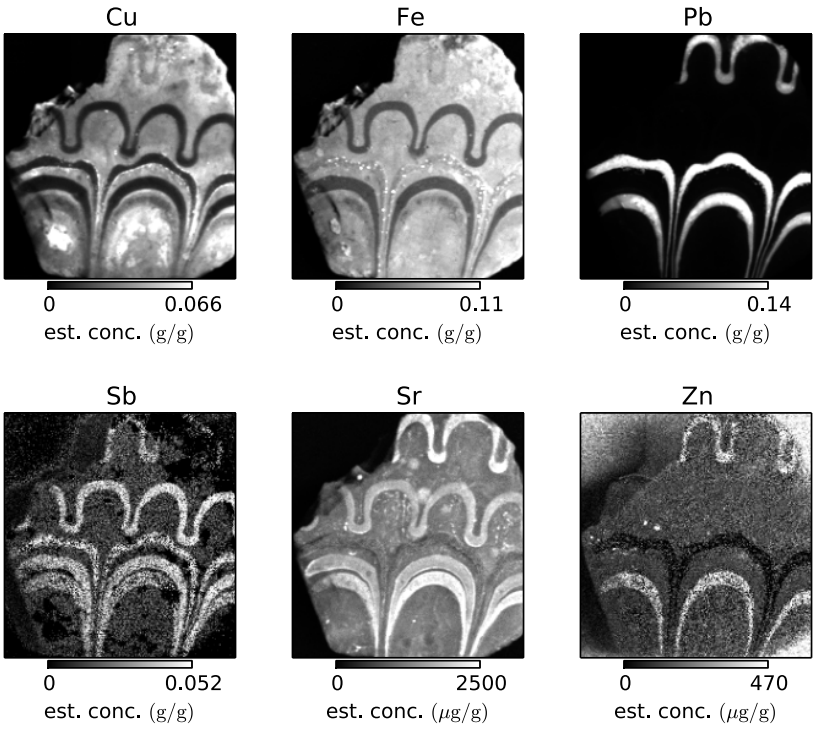


Figure 4.2: Selected element maps from sample 6a

rectangular, they typically include "background" regions off of the sample edges. Including these irrelevant areas would skew statistics and complicate the analysis, so we mask them off. This is easily done by hand, although the process could be automated.

Next, we apply a smoothing filter. Shot noise is the dominant noise source for low-concentration elements. We trade spatial resolution for reduced noise by applying a Gaussian filter with a footprint size proportional to $(\bar{n}_e)^{-\frac{1}{2}}$, where $\bar{n}_e$ is the mean number of counts per pixel for a given element, up to a maximum of $5 \times 5$ pixels. This allows us to maintain overall spatial resolution using the high-count elements (e.g. lead), while dramatically reducing the variance of trace elements (e.g. zinc). This step is essential for accurate classification.

Finally, for purposes of clustering and analysis, the element data are normalized. We compute

$$x_{i,e} = (c_{i,e} - \mu_e)/\sigma_e$$

where $c_{i,e}$ is the estimate of concentration of element $e$ at the $i$th pixel, and $\mu_e$ and $\sigma_e$ are the mean and standard deviation, respectively, of element $e$, over the entire scanned sample area. We will refer to the vector of all normalized elements at a pixel as $x_i = (x_{i,e_1}, ..., x_{i,e_n})$

**How many colors?**

We wish to classify the bands of the sample according to color (effectively segmenting the image of the sample), and ultimately to identify these colors. To do so, we apply a clustering technique. Most clustering schemes require the number of clusters to be specified *a priori*, so the first problem is to attempt to determine how many different colors (i.e. types of glass) are present. In many cases, this is not immediately obvious.

It is difficult to visualize clusters in high-dimensional spaces (six-dimensional, in this case); some form of dimensionality reduction is helpful. A simple but effective technique is to apply principal component analysis (PCA) [20] to the element data.[2] Figure 4.3 shows

[2]Since the data are Poisson-distributed, they should, in principle, be transformed to a normal distribution before PCA is applied. In practice, the counts are large enough that this makes no significant difference.

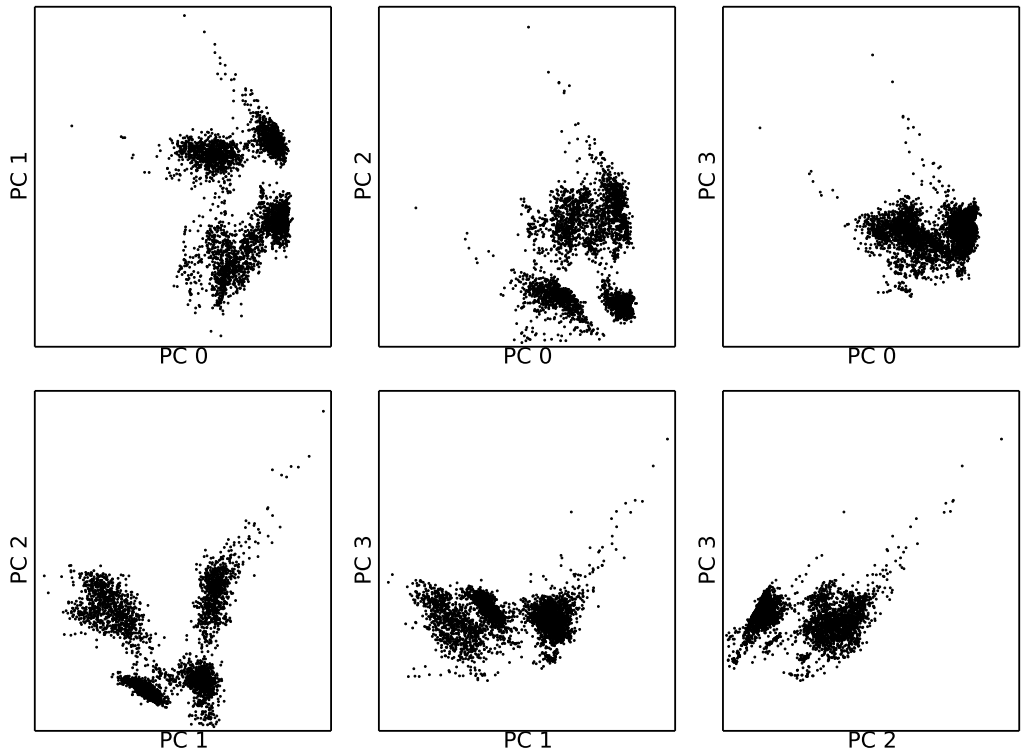


Figure 4.3: Principal components analysis of sample 6a data

scatter plots for the first three principal components. There appear to be four distinct clusters, so we proceed under this assumption (which we will later check). The clusters also appear to be linearly separable, which simplifies the analysis.

### 4.5.3 Clustering

In many cases, it may be possible to segment the images of the sample by hand, e.g., by hand-selecting the pixels associated with a particular decorative stripe. However, such a process is necessarily subjective; it is also time-consuming, if a large number of samples are to be analyzed. Thus, we seek a method to automatically use trace element concentrations to classify each pixel as belonging to a particular color.

One such technique is $k$-means clustering, which attempts to find the partition of the data into $k$ clusters such that each data point is closer to the mean of its own cluster than

to the mean of any other cluster [21]. We obtain slightly better results using a variant called fuzzy $c$-means: instead of a "hard" label, each point is assigned a *weight* $c_k \in [0, 1]$, $\Sigma c_k = 1$ (which could be interpreted as a probability) for being in the $k$th cluster. This allows for diffusion and mixing at color boundaries; it also provides a rudimentary estimate of clustering uncertainty. The algorithm is well covered in the literature [2, 11, 22], but we provide a summary here:

Select the number of clusters $c$. Let $u_{ij}$ be the weight of pixel $i$ in cluster $j$. Initialize $u_{ij}$ randomly. Select a fuzziness exponent $m > 1$; $m = 1$ is equivalent to "hard" k-means. Then repeat until convergence:

1. Calculate the cluster centers:
$$c_j \leftarrow \frac{\sum_i u_{ij}^m \cdot x_i}{\sum_i u_{ij}^m}$$

2. Update the weights:
$$u_{ij} \leftarrow \left[ \sum_l^c \left( \frac{\|x_i - c_j\|}{\|x_i - c_k\|} \right)^{\frac{2}{m-1}} \right]^{-1}$$
where $\|\cdot\|$ is the Euclidean distance.

This algorithm converges to a local minimum or saddle point of the objective function

$$J = \sum_{ij} u_{ij}^m \|x_i - c_i\|^2$$

Thus, it is typically restarted a number of times with different random initial weights; the best of these runs is selected.

Figure 4.4 shows the result of applying this algorithm, for four clusters (with $m = 2$)[3] to the sample 6a data. The four colors in the map have been chosen in hindsight; at this point, they can be regarded as arbitrary. Despite the fuzzy nature of the algorithm, the boundaries between stripes are fairly sharp. There is very little "noise" in the cluster assignments.

[3]The choice of $m$ is somewhat arbitrary, but $m = 2$ often gives good results [22], as was the case here.

Figure 4.4: Clustering results for sample 6a, using four clusters, depicted as turquoise, white, green, or yellow. Each pixel is assigned a color according to its nearest cluster center. The colors chosen are a arbitrary at this stage, but are chosen in light of the analysis below.

Note that this clustering was computed *using no spatial information;*[4] that is, each pixel was treated independently of its neighbors, using elemental composition alone. (Taking into account the colors of the neighborhood might be helpful in difficult cases, but it could also introduce bias and obscure boundaries and fine detail.) With this in mind, it is very encouraging that the stripes and body are clustered contiguously and consistently.

We return for a moment to the question of the number of distinct colors on the fragment. If we try to partition the data into too many clusters, areas which are actually homogeneous will be fractured – particularly because the curvature of the sample introduces a slight systematic drift in the XRF data from left to right. On the other hand, choosing too few clusters will result in different colored regions being incorrectly merged. This will be reflected in a larger minimum value of the objective function $J$.

Various validity metrics have been proposed to aid in correctly identifying the number of clusters. A particularly simple and effective [22] choice is the Xie-Beni (XB) index [45],

[4]Aside from the initial smoothing filter.

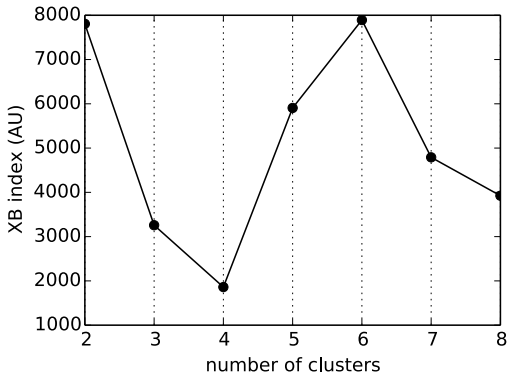


Figure 4.5: The XB index plot suggests that sample 6a has four distinct types of glass.

which is just the mean of the *within*-cluster scatter divided by the minimum *between* cluster distance:

$$S_{xb} = \frac{1}{N} \frac{\sum_{ij} u_{ij}^m \|x_i - c_i\|^2}{\min_{i \neq j} \{\|c_i - c_j\|^2\}} = \frac{1}{N} \frac{J}{\min_{i \neq j} \{\|c_i - c_j\|^2\}}$$

where $N$ is the number of data points. Figure 4.5 shows the XB index for the sample 6a data for various numbers of clusters. We see a sharp minimum at $c = 4$, supporting our hypothesis that this sample has four different colors.

Finally, Fig.a 4.6 shows the same PCA data as in figure 4.3, but labeled according to the colors in figure 4.4. The clusters are well separated in the space spanned by the first three principal components.

### Colors

It remains to associate the thus-far arbitrary cluster labels with the actual original glass colors. (To avoid confusion, we have already done so above, rather than picking arbitrary colors, but we will justify our choices here.) Ideally, we would compare the XRF spectra to ones from well-preserved specimens of various colors. Unfortunately, these are rare, and all of the fragments we examined were significantly faded. Some colored portions remain, however, and these furnished important clues. On 6a, for instance, there are faint yellow-green bands, red-brown bands and off-white bands. The body contains barely discernible spots of light

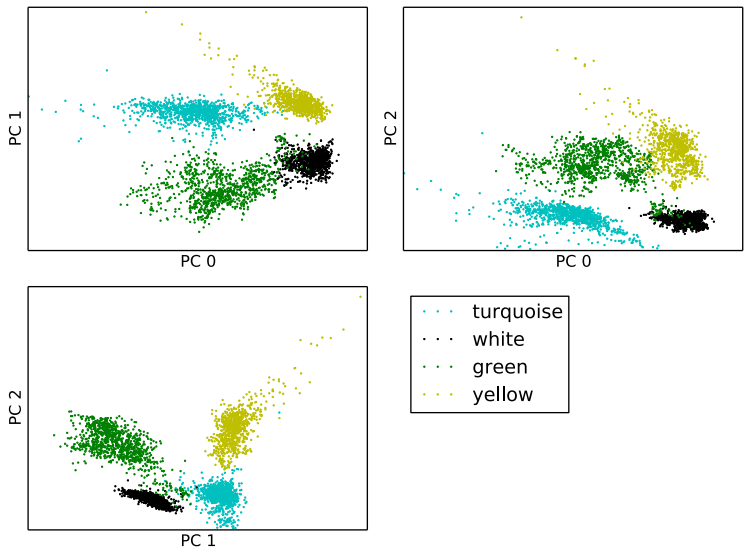


Figure 4.6: PCA clusters for sample 6a, labeled according to the colors in figure 4.4.

blue. Of course, it is not certain that these remnants of color bear any relation to the original hues, but if their composition is similar to that of known, well-preserved items, we may be reasonably confident in our identifications. Additionally, some of the thicker samples have relatively unaltered cores; these are all of blue glass, however.

Limited data on well-preserved glass from Nuzi exists; most of the items examined have been beads, and the majority of those have been blue. Much more data exists on colored glass from the Egyptian sites of Amarna and Malkata. Compositions differ, of course—for instance, Egyptian blue glass was often colored with cobalt, which has not been found in Nuzi glass—but artisans in both locations had a limited set of elements at their disposal. Furthermore, pieces from Mesopotamia and Egypt are sufficiently similar in style and composition that the provenance of pieces is often controversial, and researchers have searched for discriminants between the regions [34].

Figure 4.7 shows a histogram of the relative concentrations of the elements in the colors classified using the above analysis. The green and yellow areas are both high in lead, but the green contains a higher level of strontium (and, by proxy, calcium). The white bands are contain the most antimony (used as an opacifier). The turquoise body contains mostly

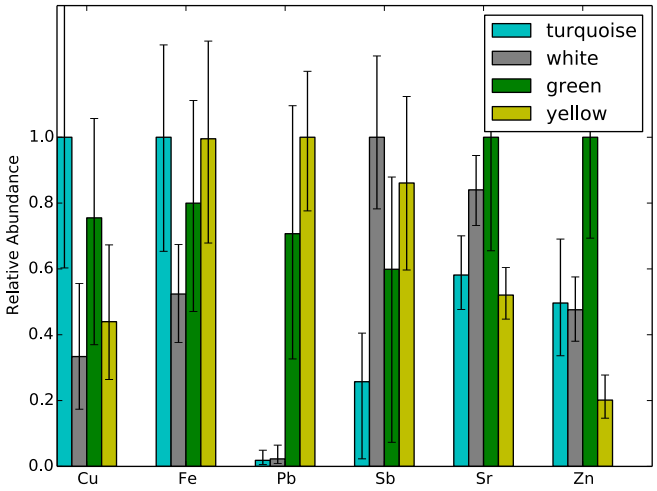


Figure 4.7: Elemental abundances by color in sample 6a, normalized to the maximum for each element. Error bars represent the 5th and 95th percentiles.

copper and iron. Curiously, the green bands contain a relatively high level of zinc. This is not, to our knowledge, used as a colorant, so it may have been introduced as an impurity in the source material.

For comparison, figure 4.8 shows a similar plot for the opaque glasses analyzed in ref. [32]. There is a large amount of scatter in these data, but the trends roughly correspond to those for sample 6a. Considering both the data from previous analyses of similar glass objects, and the remnants of color on these pieces, we can assign, with reasonable confidence, the colors shown in figure 4.10.

### 4.5.4 Classification

We distinguish between *clustering* and *classification*: Clustering, as described in the previous section, assigns labels to a set of points, with the labels chosen to minimize a given objective function. A clustering result generally has no predictive power (it cannot be applied to other data sets). In contrast, classification starts with a data set having *known* labels, and seeks a partition of the variable space which optimally separates the classes. This same partition

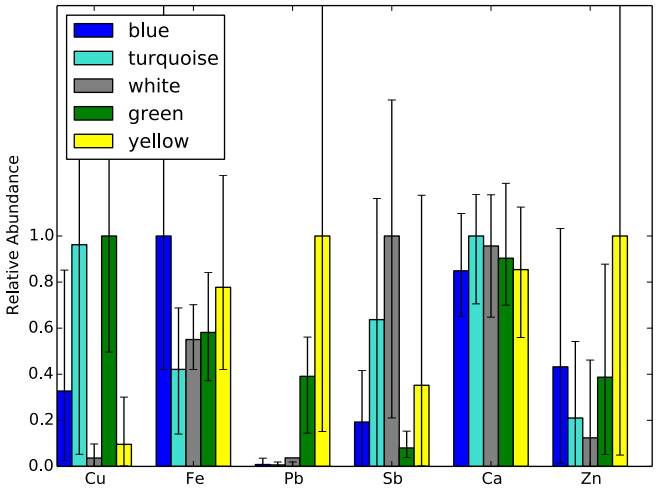


Figure 4.8: Elemental abundances by color in in the opaque glasses analyzed by Shortland and Eremin.

can then be used to predict the class labels of new data.

Since there are often multiple samples of a similar style, it is useful to be able to apply the results of analysis of one piece to the others. This also serves as a check on the consistency of the color segmentation. Sample 6 provides an ideal test case: the two large fragments 6a and 6b were adjacent to each other on the original vessel, so their compositions should be nearly identical. They were scanned separately, however, and none of the data from 6b were used in the above analysis of 6a. The idea, then, is to "train" a classifier on 6a, and apply it to 6b.

The fuzzy c-means algorithm used above to cluster the colors does not work well as a classifier. Although the cluster means can be transferred, the assignment of new observations to the clusters is far from optimal. Instead, we use a support vector machine (SVM), a popular recent technique in machine learning and data mining [9, 38, 43]. An SVM simply finds the hyperplane (possibly in a nonlinearly-transformed space) with the largest margin between two sets of data. SVMs are binary classifiers, so to classify data among $c$ classes, at least $c - 1$ SVMs must be trained.

Figure 4.9: Classification of colors in sample 6b according to the SVM trained on sample 6a.

We have trained a set of SVMs for four classes on the c-means clustered data from sample 6a, using only those pixels which have a cluster weight of at least 0.9 (i.e. those which are well clustered). The results of classifying the pixels of 6b are shown in figure 4.9. The classification is fairly consistent, although a few of the white pixels are misclassified (we note, however, that these areas are particularly heavily corroded).

## 4.6 Results

Figure 4.10 shows the reconstructed color maps for the fragments 6a and 6b, juxtaposed in their original positions relative to one another. For comparison, figure 4.11 shows an entire vase from the same time period. The vase is Egyptian, but likely similar in style. The table in Appendix 2 shows tentative color reconstructions of several more samples.

The boundaries between colors were well defined, except for the most severely eroded areas of a few samples. It was possible to distinguish even between bands which appear nearly identical upon visual inspection of the samples. The clustering and classification techniques were very successful in segmenting the XRFI maps into distinct regions, and in identifying regions of the same original glass.

It was somewhat more difficult to assign colors to the various regions. As mentioned above, we relied upon comparisons of the elemental abundances to those of samples of known color; and, where possible, remnant traces of the original color.

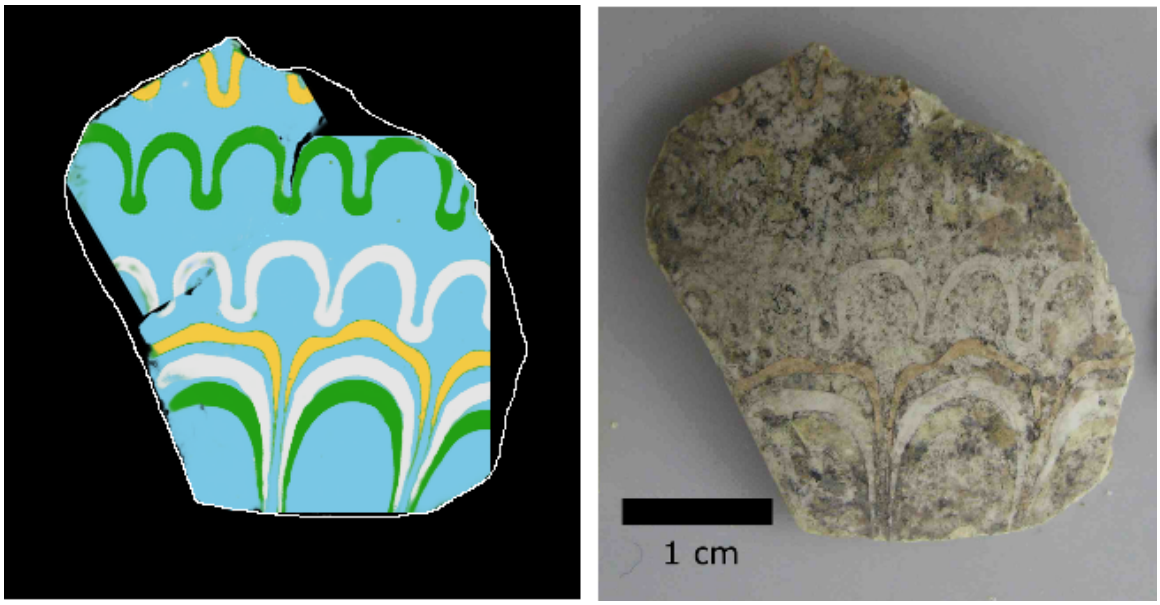


Figure 4.10: Left: Reconstructed color map of sample 6. The two fragments are aligned in their original positions; the white outline shows the borders of the original fragment. Right: photograph of the original fragment.

Figure 4.11: Core-formed vase in a similar style to sample 6 (Corning Museum of Glass).

## 4.7 Conclusions and Future Directions

We have presented effective methods of applying XRFI to recover the colors of faded ancient glass fragments. Although these items have been heavily altered, in many cases, enough of the colorant elements remain to roughly determine the original coloration and patterns.

However, color recovery depends on comparison to data from well-preserved fragments of known color. Unfortunately, the available data are so far fairly limited; furthermore, little is known about how the de-coloring alterations change the concentrations of colorant elements.

Progress could be made on two fronts: first, a systematic mapping of color (measured using colorimetry) *versus* composition for a large number of ancient glass fragments in various stages of alteration. Ideally, these would include some fragments from the same vessel, but faded to varying degrees. To date, analyses have included a few dozen fragments at most. The high speed of synchrotron-based XRF, along with the automation techniques described previously in this work, should make it possible to analyze hundreds or even thousands of fragments in a short time.

Synchrotron-based analysis also allows, with little additional effort, complementary techniques including X-ray absorption fine structure (XAFS), which provides information about the chemical environment of colorants; and X-ray diffraction (XRD), which can help identify the phases present in a sample.

A large database of ancient glass composition would facilitate the unambiguous identification of color in altered specimens, and it would also greatly enhance understanding of the construction, chemistry, alteration processes, and cultural and geographical variation of these artifacts.

We also suggest a second, experimental approach: synthesizing an array of glass samples from raw materials (silica, sodium, lime, etc.) with colorant compounds present in varying concentrations, in order to map out the color and opacity space spanned by these ingredients and firing conditions. Such a collection would help fill in the gaps left by insufficient numbers of well-preserved historical samples; furthermore, it would provide invaluable calibrations for

XRF spectra of glass objects.

These synthetic samples could also be subjected to artificial accelerated weathering and aging processes (e.g. exposure to alkaline solutions or ultraviolet light) to study the processes which lead to color fading and other alteration.

## Appendix 1: Sample Numbers

| Analysis Number | Museum Number |
|---|---|
| 2 | 1930.82.3 |
| 3 | 1930.82.4 |
| 4 | 1930.82.7 |
| 5 | 1930.82.13 |
| 6a,b | 1930.82.14 |
| 7 | 1930.82.15 |
| 8 | 1930.82.23 |
| 9 | 1930.82.51 |
| 10 | 1930.82.52 |
| 12 | 1930.82.65 |
| 13 | 1930.82.66 |
| 14 | 1930.82.67 |
| 15 | 1930.82.68 |
| 16 | 1930.82.69 |

Table 4.2: Harvard Semitic Museum catalog numbers of the samples used in this work.

## Appendix 2: Color Reconstructions

| Sample | Photo | Color Reconstruction |
|---|---|---|
| 2 | 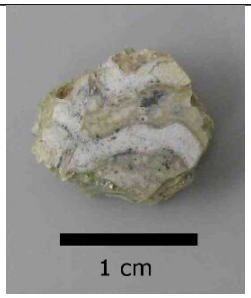  |  |
| 3 | 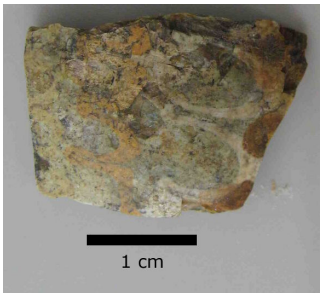  |  |
| 4 |   | 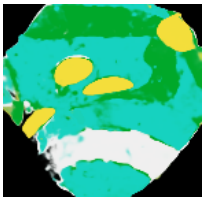 |
| 5 |   |  |
| 7 | 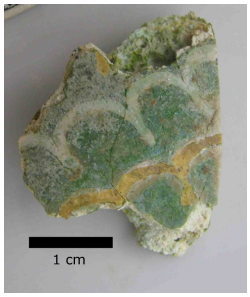  |  |

8


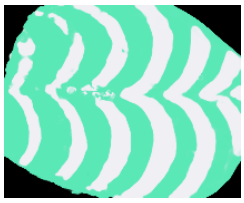

9


10


12


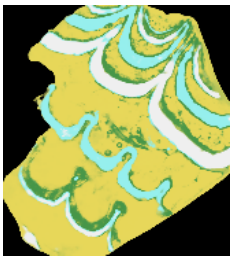

13

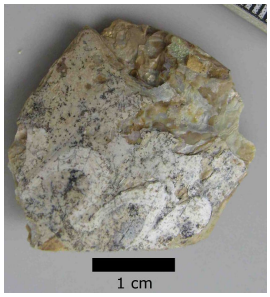


14

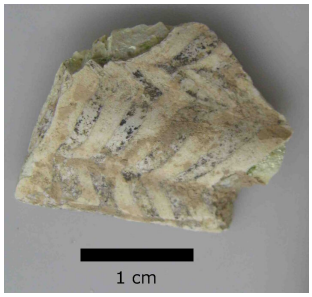


15


16


## Appendix 3: Element Data

| Sample | Feature | Ca | Cu | Fe | K | Mn | Pb | Sb | Sr |
|---|---|---|---|---|---|---|---|---|---|
| **2** | body | 36600 | 19500 | 42100 | 50000 | 2520 | 149 | 9410 | 1090 |
| | white | 52100 | 10700 | 26100 | 23700 | 2330 | 237 | 60100 | 972 |
| **3** | body | 37000 | 48300 | 34000 | 21900 | 2510 | 4410 | 14100 | 577 |
| | stripe 1 | 172000 | 24800 | 20700 | 23900 | 1520 | 81400 | 15100 | 472 |
| | stripe 2 | 64900 | 9810 | 29400 | 23700 | 3650 | 111000 | 31900 | 240 |
| | stripe 3 | 101000 | 7410 | 36400 | 12900 | 2670 | 552 | 21100 | 601 |
| **4** | stripe 1 | 568000 | 28000 | 5860 | 7700 | 445 | 4110 | 853 | 1570 |
| | stripe 2 | 659000 | 2340 | 8560 | 7000 | 693 | 540 | 11900 | 1410 |
| | stripe 3 | 618000 | 25500 | 12400 | 6970 | 465 | 6190 | 7010 | 1200 |
| | stripe 4 | 285000 | 8360 | 16200 | 13600 | 481 | 88800 | 10100 | 312 |
| **5** | body | 109000 | 386 | 51900 | 34300 | 4100 | 165 | 5500 | 1500 |
| | stripe 1 | 107000 | 559 | 28900 | 26500 | 1920 | 177 | 51600 | 1040 |
| **6** | body | 91600 | 42900 | 82900 | 54700 | 1940 | 1890 | 9180 | 1240 |
| | stripe 1 | 129000 | 25100 | 54900 | 43600 | 2720 | 88200 | 24200 | 1830 |
| | stripe 2 | 65000 | 10800 | 38200 | 46900 | 656 | 2290 | 39500 | 1840 |
| | stripe 3 | 86100 | 11400 | 59400 | 52000 | 952 | 121000 | 29900 | 1020 |
| **7** | body | 458000 | 541000 | 21600 | 16300 | 821 | 2110 | 5560 | 974 |
| | stripe 1 | 157000 | 437000 | 40900 | 19600 | 993 | 101000 | 28700 | 977 |
| | stripe 2 | 187000 | 508000 | 18100 | 14400 | 837 | 1260 | 54300 | 694 |
| **8** | body | 63200 | 23300 | 46900 | 55800 | 2250 | 191 | 6450 | 1340 |
| | stripe 1 | 123000 | 20700 | 33200 | 28300 | 2520 | 484 | 53900 | 1080 |
| **9** | body | 253000 | 1020 | 25300 | 13900 | 1870 | 208 | 468 | 1270 |
| | stripe 1 | 196000 | 530 | 49600 | 34500 | 17300 | 327 | 21900 | 1690 |
| **10** | body | 278000 | 47100 | 69500 | 18200 | 4400 | 3750 | 1280 | 794 |
| | stripe 1 | 77700 | 6760 | 25400 | 21700 | 1360 | 1770 | 60700 | 952 |
| | stripe 2 | 89000 | 25800 | 79700 | 32700 | 12800 | 53300 | 15600 | 839 |
| **12** | body | 50400 | 9710 | 48900 | 26900 | 223 | 3850 | 7970 | 972 |
| | stripe 1 | 59800 | 5100 | 32300 | 29800 | 278 | 3370 | 56600 | 1260 |
| | stripe 2 | 48400 | 22200 | 65800 | 36400 | 155 | 4760 | 12200 | 1260 |
| | stripe 3 | 51000 | 11600 | 29400 | 30400 | 299 | 3230 | 24900 | 1100 |
| **13** | body | 33000 | 91900 | 61400 | 22800 | 9370 | 357 | 12900 | 653 |
| | stripe 1 | 20700 | 18900 | 19700 | 14900 | 2690 | 398 | 26300 | 623 |
| **14** | stripe 1 | 236000 | 25700 | 37500 | 20600 | 988 | 372 | 44900 | 1220 |
| | stripe 2 | 124000 | 70700 | 63400 | 60700 | 4000 | 193 | 4420 | 1580 |
| **15** | body | 75300 | 31300 | 81000 | 27800 | 2970 | 3700 | 12500 | 681 |
| | stripe 1 | 58200 | 17500 | 87200 | 38300 | 2900 | 46800 | 27200 | 662 |
| | stripe 2 | 58400 | 14200 | 64300 | 41000 | 3910 | 112000 | 44200 | 767 |
| | stripe 3 | 62300 | 11000 | 29500 | 27600 | 1470 | 3130 | 63300 | 958 |
| **16** | body | 73900 | 616 | 73800 | 35800 | 6120 | 195 | 6400 | 778 |
| | white | 93100 | 658 | 36000 | 29100 | 2990 | 268 | 71100 | 953 |
| **mean** | | 143000 | 49900 | 46000 | 30800 | 3010 | 6260 | 16300 | 1080 |
| **std. dev.** | | 183000 | 119000 | 24200 | 18900 | 4500 | 19200 | 20400 | 411 |

Table 4.4: Mean element concentrations, in ppm, for distinct regions of the samples. Decorative stripes are numbered from bottom to top, left to right. "Body" refers to the base glass of the sample, in between applied stripes. In the cases where the color of a feature is unambiguous, it is named.

# Chapter 5

# Ceramics from the American Southwest

The following paper is reprinted with permission from the publisher.

Journal of Archaeological Science 40 (2013) 4780–4784

Contents lists available at SciVerse ScienceDirect

Journal of Archaeological Science

journal homepage: http://www.elsevier.com/locate/jas

Focus article

# Application of X-ray fluorescence imaging to ceramics from the American Southwest

Ethan C. Geil [a], Steven A. LeBlanc [b], Darren S. Dale [c], Robert E. Thorne [a,*]

[a] Physics Department, Cornell University, 529A Clark Hall, Ithaca, NY 14853, USA
[b] Peabody Museum of Archaeology and Ethnology, Harvard University, Cambridge, MA 02138, USA
[c] Cornell High-Energy Synchrotron Source, Cornell University, Ithaca, NY 14853, USA

ARTICLE INFO

*Article history:*
Received 19 January 2013
Received in revised form
10 May 2013
Accepted 17 May 2013

*Keywords:*
X-ray fluorescence
Imaging
Pottery
Ceramic
Pigment
Synchrotron

ABSTRACT

We have used synchrotron-based X-ray fluorescence imaging (XRFI) to examine sherds of painted ceramics from prehistoric cultures of the American Southwest. These sherds are very well suited to XRFI analysis. Paints can generally be detected and distinguished by the fluorescence intensities of their constituent elements. Spatial maps of element distributions yield the spatial distribution of pigments. Pigments can be distinguished that are (or have become) visually similar; layers that have been obscured by overpainting can be examined; and pigment residues can be distinguished from surface contaminants deposited after painting and firing. As a result, XRFI allows the painted motifs to be clarified and hidden features to be revealed. Furthermore, the very rapid scanning and high sensitivity elemental detection possible with synchrotron-based XRFI facilitate measurements on large collections of sherds, allowing an integrative rather than anecdotal analysis.



## 1. Introduction

A key problem in the study of ancient artifacts is that their surfaces have often been modified through weathering, erosion, fading, encrustation, overpainting, and other processes. In the case of ceramics, these processes can obscure or damage the original painted designs.

X-ray fluorescence (XRF) is widely used in art and archaeology for non-destructive evaluation of the composition of an object's surface layers (Mantler and Schreiner, 2000). When illuminated by high energy X-rays, an atom will emit fluorescent X-rays at specific energies determined by its atomic number. A sample's fluorescence spectrum can then provide information about elemental concentrations (Thompson et al., 2009). This can aid in understanding, among other things, how objects were constructed (Hahn et al., 2004; Sciau et al., 2011) and where they were constructed (i.e., their provenance) (Papachristodoulou et al., 2006), and thus can provide information about patterns of trade (Nazaroff et al., 2010).

In XRF imaging (XRFI), fluorescence is recorded as a small X-ray beam is scanned across an object. These data can then be used to generate two or even three-dimensional maps of the elemental composition of the object's surface layers (Adams et al., 1998; Kanngiesser et al., 2003; Vincze et al., 2004). X-rays can penetrate hundreds of micrometers or more (depending upon composition and X-ray energy) below the surface of an object, allowing materials to be imaged beneath layers of paint or dirt. XRFI has yielded valuable information about many types of artifacts (Scott, 2001; Trentelman et al., 2010), including drawings (Reiche et al., 2009), paintings (Dik et al., 2008; Woll et al., 2006), pigments (Cotte et al., 2007), and inscriptions on stone (Powers et al., 2005, 2009).

Here, we apply synchrotron-based XRFI to examine painted pottery from the southwestern United States. The paints on these objects typically have an elemental composition that differs from that of the substrate and from each other, allowing XRFI to map out pigment distributions. A variety of analytical techniques have previously been used to study paints, glazes, slips, and pastes on these artifacts (Mills, 2000; Glowacki and Neff, 2002). These include laser-ablation inductively-coupled-plasma mass spectrometry (LA-ICP-MS) (Habicht-Mauche et al., 2000; Duwe and Neff, 2007), instrumental neutron activation analysis (INAA) (Dahlin et al., 2007; Speakman et al., 2011), and electron microprobe (Huntley, 2006). While these techniques can yield precise element ratios, the first two are destructive, and all are limited to small pieces. XRF using conventional X-ray tube sources has previously been used to examine a few points or lines on ceramic samples from the Southwest (Speakman et al., 2011) and from Mesoamerica (Sánchez del Río et al., 2004; Nazaroff et al., 2010; Ruvalcaba Sil et al., 2010).

* Corresponding author. Tel.: +1 607 592 8812; fax: +1 607 697 0400.
*E-mail address:* ret6@cornell.edu (R.E. Thorne).

0305-4403/$ – see front matter © 2013 Elsevier Ltd. All rights reserved.
http://dx.doi.org/10.1016/j.jas.2013.05.014

## 2. Method and samples

### 2.1. Experimental setup

Conventional XRF analysis using tube X-ray sources suffers from relatively low count rates, so that relatively long times are required to acquire a single spectrum from a single point, particularly if trace elements are to be analyzed (Ruvalcaba Sil et al., 2010). Thus, scanning even small areas (e.g., 20 × 20 points) using tube sources can be prohibitively time consuming.

Synchrotron sources offer several advantages for XRF analysis. Synchrotron X-ray beams have spectral brightnesses $10^5$–$10^7$ times larger than tube sources. Beam energies can be tuned to 30 keV or more, and beams can be focused down to a micrometer or less (Adams et al., 1998). High beam intensities dramatically reduce the time required to acquire spectra, making it possible to analyze thousands or even millions of points per hour (Ryan et al., 2010), and thus to scan and image large areas. The Bremsstrahlung characteristic of tube sources is eliminated, greatly enhancing the signal-to-background ratio of spectra, allowing trace elements at very low concentrations to be detected and quantified (Saisho and Hashimoto, 1996). With suitable XYZ stages, samples of size 1 m and even larger can be examined. More than forty synchrotron sources are now available around the world, and most offer use of their beamlines – as well as technical support from their staff – at no cost to researchers.

The sherds in this study were examined at beamline F3 at the Cornell High Energy Synchrotron Source (CHESS), using the setup shown in Fig. 1. Samples up to 30 cm in size were mounted on a motorized XYZ table, and positioned with better than 10 μm accuracy. Samples were illuminated normal to their surface using a 16.5 keV X-ray beam with a flux of approximately $10^{11}$ photons/s/mm$^2$. Slits defined a rectangular beam of size 0.1 mm–0.25 mm, determined by the smallest sample features of interest. Fluorescence spectra were measured using a four-element Vortex-ME4 silicon drift detector (SII Nanotechnology). Spectra of photon counts versus energy were generated using a DXP-XMAP digital spectrometer (XIA LLC).

To generate XRF images, an XRF spectrum was recorded at each point in a grid of points by raster scanning the sample relative to the X-ray beam. Scan speeds were 1 mm/s and grid spacings were typically 0.1–0.25 mm. Graphical display of element maps and fundamental parameters estimates of elemental compositions (Solé et al., 2006) were performed in nearly real time using Praxes (Darren Dale, CHESS), Our setup and choice of X-ray energy allowed detection of fluorescent X-rays with energies from roughly 3 keV to 16 keV. A standard (Buffalo River Sediment, NBS SRM2704) was used for calibration. Additional experimental details are given in the Supplementary material.

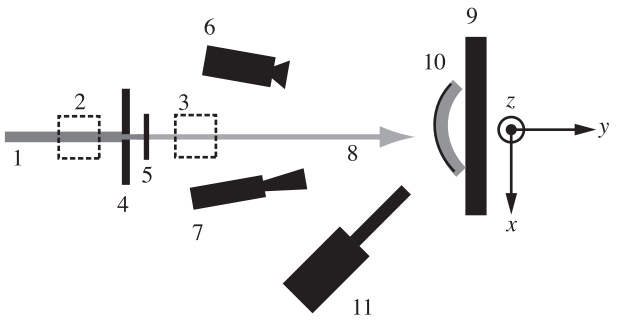


**Fig. 1.** Experimental setup. (1) Incident x-ray beam (2) first ion chamber (3) second ion chamber (4) beam size control slits (5) attenuator (6) wide field camera (7) zoom camera (8) attenuated, narrow X-ray beam (9) XYZ stage (10) sample and (11) four-element silicon drift detector.

Although XRF allows elemental mass fractions to be estimated, precise determinations are usually not possible. Both incident and fluorescent X-rays are absorbed by atoms in a sample, and so detected elemental fluorescence depends upon the detailed (and generally unknown) sample structure and composition. In our experiments, the pigment layers (of unknown thickness) were likely thinner than the fluorescence escape depth, so the XRF signal contained components in unknown and varying proportions from both the substrate and pigment. The matrices of both the paint and substrate were also unknown; analysis was performed assuming a matrix of kaolin, a common slip material for ceramics from this region (Shafer, 2003). Measured fluorescence is also perturbed by geometric effects associated with surface curvature and roughness (Bonizzoni et al., 2006; Trojek et al., 2010; Smilgies et al., 2012).

### 2.2. Samples

Much of the understanding of prehistoric pottery production in the American Southwest derives from the pioneering work of Anna O. Shepard (1968). The pottery sherds examined here were all from the collection of the Peabody Museum of Archaeology and Ethnology. Roughly 150 sherds from different sites and periods and having a variety of pigment colors and patterns were examined. We limit discussion here to four representative pieces to illustrate application of XRFI. For simplicity of reference, we use arbitrary sample letters rather than their accession numbers.

*Sherd* (*A*) (Fig. 2): A sherd of Sikyakti Polychrome. This sherd was made between AD1350–1600 in the area of the present day Hopi Reservation in northern Arizona. It was likely fired with coal. The almost white background is a self slip from a very fine residual clay. The black/brown, red and cream paints are all presumably from nodules of hematite or limonite or combinations of them, or clays that contain meaningful amounts of iron. They would have been mixed in some cases with vegetal substance as described for sherd (D).

*Sherd* (*B*) (Fig. 3): A sherd of Ramos Polychrome from the site of Casas Grandes (Paquime) in northern Chihuahua that dates to AD1200–1400. The cream background is a self slip from the clay body. The black and the red paints presumably derive from hematite and limonite mixed with a vegetal substance as described for sherd (D).

*Sherd* (*C*) (Fig. 4): This sherd is Mimbres Classic B/W made between AD1000 and 1130 in Southwestern New Mexico. The paint is an iron paint presumably made by grinding a piece of hematite and mixing it with a vegetal substance as described for sherd (D). The white background is a white firing clay slip, probably a kaolin clay.

*Sherd* (*D*) (Fig. 5): This sherd is typed as Flagstaff B/W and was probably made between 1100 and 1250 AD in northern Arizona. The painted designs are what Southwestern archaeologists term carbon paint. It is believed that a plant was boiled to produce a dense burnt carbon that was used as a paint. Historically, Pueblo peoples boiled Rocky Mountain Bee Weed to produce such a substance. Apparently, no iron was added to the paint. The white background is a white firing clay slip, probably a kaolin clay.

The “paints” on these objects include differentially firing clays, oxides of iron derived from nodules with other inclusions, and vegetal carbon. In the discussion that follows, we refer to these as “pigments” rather than “paint”; the latter term would be used by many Southwestern archaeologists, but the former appears more widely understood by non-Southwestern archaeologists.

## 3. Results

Figs. 2–5 depict these four sherds and selected XRFI-derived element maps. The pigments on the first three sherds are

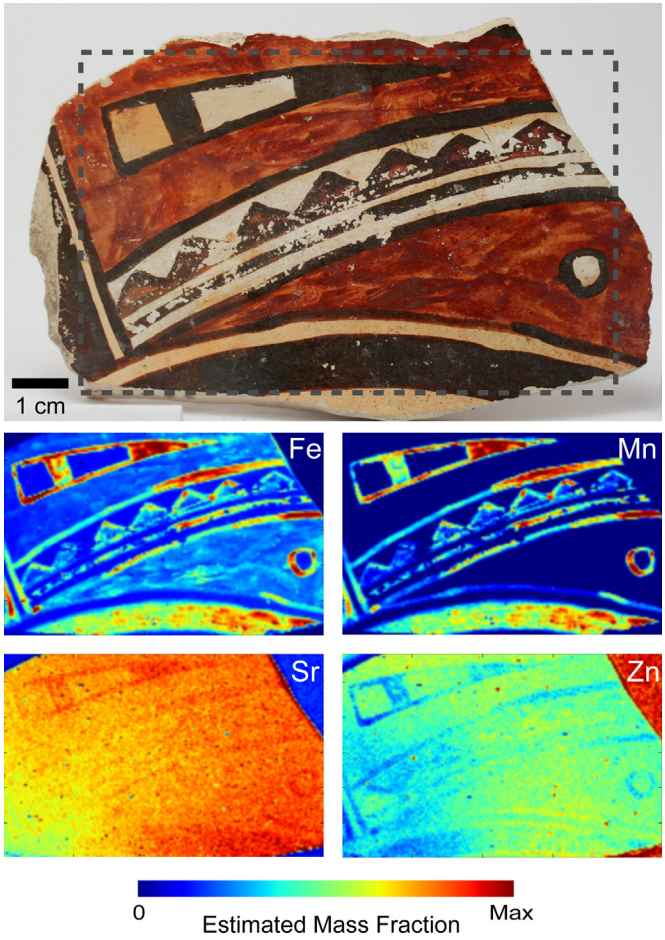


**Fig. 2.** Sherd A. Top: photograph with scan area outlined. Bottom: four element maps. Maximum estimated mass fractions: Fe, 0.55; Mn, 0.05; Sr, $3 \times 10^{-4}$; Zn, $6 \times 10^{-4}$. Dark brown areas in the photograph are rich in Mn and Fe, while red areas are rich in Fe. The background slip is richer in Zn and is shadowed by the paint. Sr is relatively uniform. (For interpretation of the references to color in this figure legend, the reader is referred to the web version of this article.)

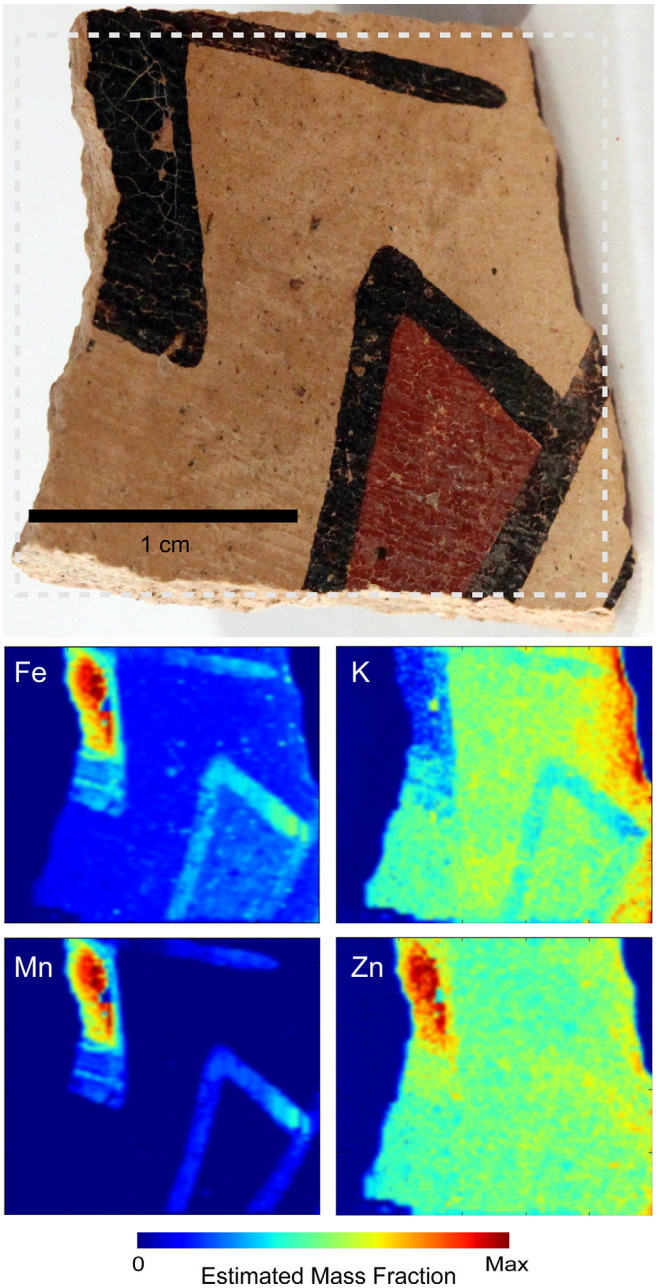


**Fig. 3.** Sherd B. Top: photograph with scan area outlined. Bottom: four element maps. Maximum estimated mass fractions: Fe, 0.04. K, 0.01; Mn, 0.04; Zn, $4 \times 10^{-5}$. Black pigment is high in Fe, Mn, and Zn; red in Fe. The background slip is high in K and is shadowed by the pigment. Note the hidden feature in the solid dark region at upper right, evident in the fluorescence maps; this may have been overpainted. (For interpretation of the references to color in this figure legend, the reader is referred to the web version of this article.)

believed to have been derived from mineral sources. On these sherds, as well as the vast majority of others we have examined, dark brown and black pigments are rich in iron and manganese, and often one or more of barium, calcium, lead, titanium, and zinc. Red pigments are typically rich in iron, but not in manganese or other heavy metallic elements.

### 3.1. Sherd (A)

This polychromatic sherd includes at least three different pigment colors: dark brown, red-orange, and white. The iron and manganese fluorescence maps correlate strongly with the painted decoration. The dark brown areas are rich in both iron and manganese, while the red-orange areas are rich in just iron. In the red-orange areas, thicker layers of paint correspond to higher iron signals. The background slip appears to contain higher concentrations of zinc than do the pigments, and absorption by the dark brown painted lines produces "shadows" on the zinc map. Strontium is fairly uniform across the sherd, with slight enhancement in the dark lines. The strontium map also shows the effect of the sherd curvature: the detector was located to the right of the image, so areas at left that curved away from it show a weaker signal. The white areas did not show appreciable correlation with any of the elements maps. The fine clay used in the white paint was likely similar in composition to the base slip.

### 3.2. Sherd (B)

This sherd features both red and black pigments. The dark lines, like those on Sherd A, are rich in iron and manganese but, unlike Sherd A, are also enriched in zinc. The red area is enriched in iron, but not manganese or zinc. The slip contains significant potassium; the dark painted lines appear to absorb the potassium fluorescence, resulting in shadows on the potassium map. Interestingly, the dark

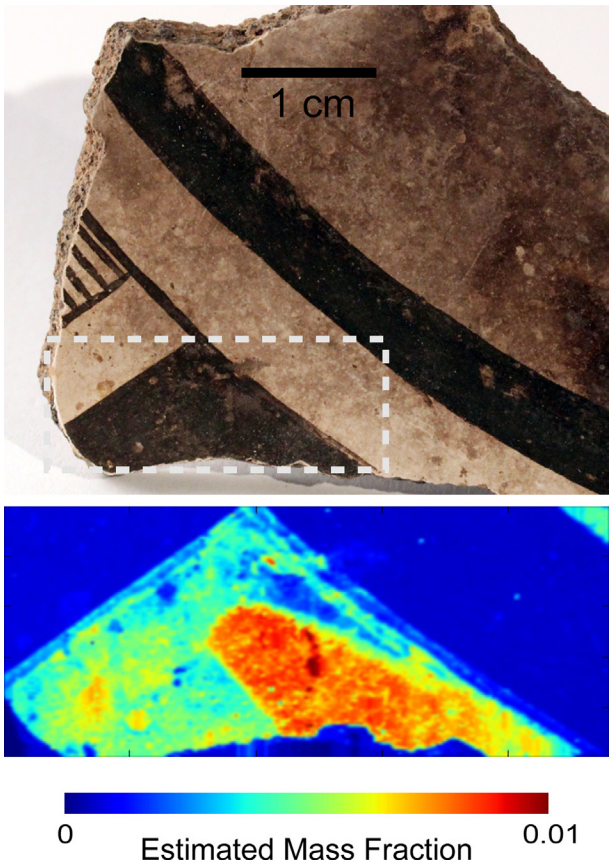


**Fig. 4.** Sherd C. Top: photograph with scan area outlined. Bottom: Fe fluorescence map. A rounded feature within the solid dark area is barely discernible in visible light, but it shows up clearly in the Fe fluorescence map. This may have been a feature which was overpainted.

area at the upper right contains an oval-shaped figure, which is not apparent on visual inspection, except perhaps in the pattern of cracks in the paint. This appears to be an area where the paint is especially thick, resulting in an increased fluorescence signal. The oval-shaped figure may have been painted first and then covered over with the larger linear figure.

### 3.3. Sherd (C)

Here is another example of a "hidden" feature. On visual inspection, the dark rounded figure is difficult to discern, and it is not clear whether it is a darkened area of paint or a deliberately painted feature. However, in the iron map this feature stands out. From the other element maps, this feature appears to have the same composition as the surrounding paint, but the paint within it is significantly thicker. It is possible that a figure was painted over, perhaps to revise the design. Note that the iron map also clearly shows the outlining of the angular region.

### 3.4. Sherd (D)

Unlike the other sherds, this one is believed to have been decorated with an organic (not mineral) pigment. Our experimental setup is not sensitive to carbon fluorescence. However, the paint contains significant quantities of copper, potassium, and manganese (presumably from plant sources), and these provide high contrast in the corresponding maps. The paint is also thick enough to shadow the iron in the slip and substrate.

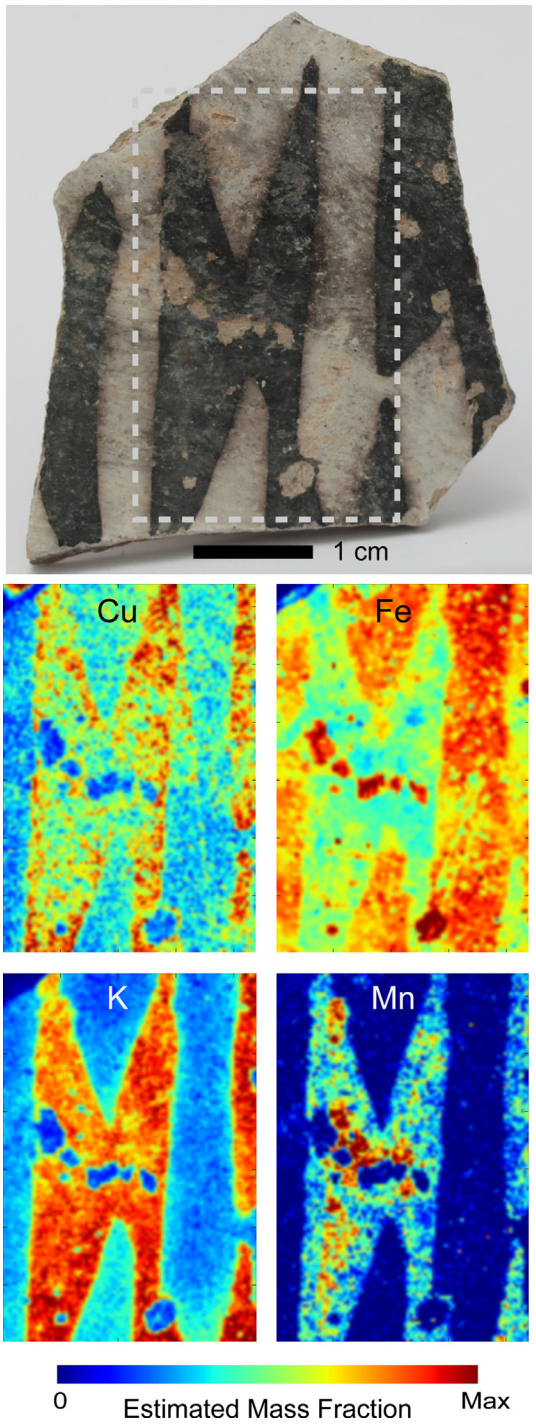


**Fig. 5.** Sherd D. Top: photograph with scan area outlined. Bottom: four element maps. Maximum estimated mass fractions: Cu, $3 \times 10^{-4}$; Fe, 0.1; K, 0.25; Mn, $2 \times 10^{-3}$. Black areas are rich in K, Cu, and Mn, but are poorer in Fe than the bare slip. The pigment is believed to be vegetal, with no added mineral pigment.

## 4. Discussion and conclusions

Most paints used on these sherds appear to employ metal-containing compounds to produce color. Each color on a sherd fluoresced with a different set of elements, so it is possible to map out the distribution of the colors across the sherd, even where colors overlap. However, similar colors on different sherds often contained different trace elements. For instance, some

black slips included measurable quantities of lead, while others did not. This suggests that a variety of mineral sources were used to make the pigments. It may be possible, through careful mapping, to use the elemental compositions of slips to determine the provenance of some sherds and of the pigments used on them.

Not all pigments were easily visible in the XRFI maps. Orange and white figures showed weak or even undetectable fluorescence signals, and on a few samples even dark brown lines did not show contrast with the surrounding slip. Extending the present measurements to lower and higher energies and more detailed trace element analysis might allow these paints to be distinguished from the slip.

XRFI often revealed features (e.g., on Sherds B and C) that were difficult or impossible to see by eye. On sherds with damaged surfaces, XRFI allowed paint remains to be distinguished from, e.g., surface contamination, facilitating reconstruction of the original motif. The thousands of grid points sampled in synchrotron-based XRFI provide far more information than a collection of single-point XRF spectra, and facilitate detailed understanding of the painted designs necessary for epigraphy and iconography, among other studies.

Analytical work focused on interpretation and recovery of painted motifs on Southwestern ceramics has so far been limited. As indicated by the above images, these ceramics are extremely well suited to synchrotron-based XRFI. The objects are compact, and the characteristic size of painted lines is on the order of 1 mm, so relatively few pixels are required to form a complete image. The sherds generally have smooth surfaces, simplifying interpretation of fluorescence intensities. An improved data acquisition setup should allow sample throughput to be increased from roughly forty to several hundred sherds per week of synchrotron beam time, allowing study of, e.g., large collections of pieces from multiple sites. This will facilitate large-scale synthesis of information about motifs, pigment compositions, and patterns of trade, and allow more detailed understanding of these objects, their manufacture, and their creators.

## Acknowledgments

We would like to thank the Peabody Museum of Archaeology and Ethnology, Harvard University, and especially Dr. Viva Fisher, for making sherds available to us. This work was supported by a grant from the Kress Foundation. It is based upon research conducted at the Cornell High Energy Synchrotron Source (CHESS) which is supported by the National Science Foundation and the National Institutes of Health/National Institute of General Medical Sciences under NSF award DMR-0936384.

## Appendix A. Supplementary data

Supplementary data related to this article can be found at http://dx.doi.org/10.1016/j.jas.2013.05.014.

## References

Adams, F., Janssens, K., Snigirev, A., 1998. Microscopic X-ray fluorescence analysis and related methods with laboratory and synchrotron radiation sources. J. Anal. At. Spectrom. 13, 319–331.
Bonizzoni, L., Maloni, A., Milazzo, M., 2006. Evaluation of effects of irregular shape on quantitative XRF analysis of metal objects. X-ray Spectrom. 35, 390–399.
Cotte, M., Welcomme, E., Solé, V.A., et al., 2007. Synchrotron-based x-ray spectromicroscopy used for the study of an atypical micrometric pigment in 16th century paintings. Anal. Chem. 79, 6988–6994.
Dahlin, E.S., Carlson, D.L., James, W.D., Shafer, H.J., 2007. Distribution patterns of Mimbres ceramics using INAA and multivariate statistical methods. J. Radioanal. Nucl. Chem. 271, 461–466.
Dik, J., Janssens, K., Van Der Snickt, G., et al., 2008. Visualization of a lost painting by Vincent van Gogh using synchrotron radiation based x-ray fluorescence elemental mapping. Anal. Chem. 80 (16), 6436–6442.
Duwe, S., Neff, H., 2007. Glaze and slip pigment analysis of Pueblo IV period ceramics from east-central Arizona using time of flight-laser ablation-inductively coupled plasma-mas spectrometry (TOF-LA-ICP-MS). J. Archeol. Sci. 34, 403–414.
Glowacki, D.M., Neff, H., 2002. Ceramic Production and Circulation in the Greater Southwest: Source Determination by INAA and Complementary Mineralogical Investigations. Cotzen Institute of Archaeology Press.
Habicht-Mauche, J.A., Glenn, S.T., Milford, H., Flegal, A.R., 2000. Isotopic tracing of prehistoric Rio Grande Glaze-paint production and trade. J. Archeol. Sci. 27, 709–713.
Hahn, O., Malzer, W., Kanngiesser, B., Beckhoff, B., 2004. Characterization of iron-gall inks in historical manuscripts and music compositions using X-ray fluorescence spectrometry. X-ray Spectrom. 33, 234–239.
Huntley, D.L., 2006. From recipe to identity. In: Habiche-Mauche, J.A., Eckert, S.L., Huntley, D.L. (Eds.), The Social Life of Pots: Glaze Wares and Cultural Dynamics in the Southwest. University of Arizona Press.
Kanngiesser, B., Malzer, W., Reiche, I., 2003. A new 3D micro X-ray fluorescence analysis set-up – first archaeometric applications. Nucl. Inst. Meth. B 211, 259–264.
Mantler, M., Schreiner, M., 2000. X-ray fluorescence spectrometry in art and archaeology. X-ray Spectrom. 29, 3–17.
Mills, Barbara J., 2000. Ceramic Production in the American Southwest. U. of Arizona Press.
Nazaroff, A.J., Prufer, K.M., Drake, B.L., 2010. Assessing the applicability of portable X-ray fluorescence spectrometry for obsidian provenance research in the Maya lowlands. J. Archeol. Sci. 37, 885–895.
Papachristodoulou, C., Oikonomou, A., Ioannides, K., Gravani, K., 2006. A study of ancient pottery by means of X-ray fluorescence spectroscopy, multivariate statistics and mineralogical analysis. Anal. Chim. Acta 573–574, 347–353.
Powers, J., Dimitrova, N., Huang, R., et al., 2005. X-ray fluorescence imaging recovers writing from ancient inscriptions. Z. Papyrologie Epigraphik 152, 221–227.
Powers, J., Smilgies, D.-M., Geil, E., et al., 2009. X-ray fluorescence imaging analysis of inscription provenance. J. Archeol. Sci. 36 (2), 343–350.
Reiche, I., Radtke, M., Berger, A., et al., 2009. Spatially resolved synchrotron-induced X-ray fluorescence analyses of metal point drawings and their mysterious inscriptions. Spectrochim. Acta B 59, 1657–1662.
Ruvalcaba Sil, J.L., Ramírez Miranda, D., Aguilar Melo, V., Picazo, F., 2010. SANDRA: a portable XRF system for the study of Mexican cultural heritage. X-ray Spectrom. 39, 338–345.
Ryan, C.G., Kirkham, R., Hough, R.M., et al., 2010. Elemental imaging using the Maia detector array: the benefits and challenges of large solid-angle. Nucl. Instrum. Meth. A 619, 37–43.
Saisho, H., Hashimoto, H., 1996. X-ray fluorescence analysis. In: Saisho, H., Gohshi, Y. (Eds.), Applications of Synchrotron Radiation to Materials Analysis. Elsevier, Amsterdam.
Sánchez del Río, M., Martinetto, P., Somogyi, A., et al., 2004. Microanalysis of archaeological mural samples containing Maya blue pigment. Spectrochim. Acta B 59, 1619–1625.
Sciau, P., Leon, Y., Goudeau, P., Fakra, S., Webb, S., Mehta, A., 2011. Reverse engineering the ancient ceramic technology based on X-ray fluorescence spectromicroscopy. J. Anal. Atom. Spectrom. 26, 969–976.
Scott, D.A., 2001. The application of scanning X-ray fluorescence microanalysis in the examination of cultural materials. Archaeometry 43, 475–482.
Shafer, H.J., 2003. Mimbres: Archaeology at the NAN Ranch Ruin. University of New Mexico Press, Albuquerque.
Shepard, A.O., 1968. Ceramics for the Archaeologist. Carnegie Institution of Washington. Publication 609, Washington, D.C.
Smilgies, D.M., Powers, J.A., Bilderback, D.H., Thorne, R.E., 2012. Dual detector X-ray fluorescence imaging of ancient artifacts with surface relief. J. Synch. Rad. 19, 547–550.
Solé, V.A., Papillon, E., Cotte, M., et al., 2006. A multiplatform code for the analysis of energy-dispersive X-ray fluorescence spectra. Spectrochim. Acta B 62 (1), 63–68.
Speakman, R.J., Little, N.C., Creel, D., et al., 2011. Sourcing ceramics with portable XRF spectrometers? A comparison with INAA using Mimbres pottery from the American Southwest. J. Archeol. Sci. 38, 3483–3496.
Thompson, A., et al., 2009. X-ray Data Booklet. Lawrence Berkeley National Laboratory, Berkeley.
Trentelman, K., Bouchard, M., Ganio, M., et al., 2010. The examination of works of art using in situ XRF line and area scans. X-ray Spectrom. 39, 159–166.
Trojek, T., Cechák, T., Musílek, L., 2010. Monte Carlo simulations of disturbing effects in quantitative in-situ X-ray fluorescence analysis and microanalysis. Nucl. Instrum. Meth. A 619, 266–269.
Vincze, L., Vekemans, B., Brenker, F.E., Falkenberg, B., Rickers, K., Somogyi, A., Kersten, M., Adams, F., 2004. Three-dimensional trace element analysis by confocal X-ray microfluorescence imaging. Anal. Chem. 76, 6786–6791.
Woll, A.R., Mass, J., Bisulca, C., et al., 2006. Development of confocal X-ray fluorescence (XRF) microscopy at the Cornell high energy synchrotron source. Appl. Phys. A Mater. 83 (2), 235–238.

# Chapter 6

# Appendix 1: Determining Provenance

The following paper is reprinted with permission from the publisher.

Journal of Archaeological Science 36 (2009) 343–350

Contents lists available at ScienceDirect

Journal of Archaeological Science

journal homepage: http://www.elsevier.com/locate/jas

# X-ray fluorescence imaging analysis of inscription provenance

J. Powers [a], D.-M. Smilgies [b], E.C. Geil [a], K. Clinton [c], N. Dimitrova [c], M. Peachin [d], R.E. Thorne [a,*]

[a] Department of Physics, Cornell University, Ithaca, NY 14853, USA
[b] Cornell High-Energy Synchrotron Source, Ithaca, NY 14853, USA
[c] Department of Classics, Cornell University, Ithaca, NY 14853, USA
[d] Department of Classics, New York University, NY 10012, USA

ARTICLE INFO

*Article history:*
Received 20 August 2007
Received in revised form 9 September 2008
Accepted 10 September 2008

*Keywords:*
Inscriptions
Epigraphy
X-ray fluorescence

ABSTRACT

A stone tablet from New York University considered to be a copy of an inscription from Teanum Sidicinum is examined with X-ray fluorescence (XRF) and XRF imaging. Fluorescence spectra show many of the same elements seen in ancient Roman inscriptions, but the fluorescence intensity from calcium is much weaker and that from many other elements is much stronger. The weak calcium fluorescence cannot be due to X-ray absorption by other elements present, and so the tablet is unlikely to be of marble. This conclusion is supported by X-ray diffraction and electron microprobe measurements. Unlike for other examined inscriptions, XRF imaging indicates little or no correlation between the variation of trace element concentrations across the tablet surface and the presence of characters. These results confirm that the inscription is a copy and demonstrate how XRF imaging can assist in evaluating inscription provenance.



## 1. Introduction

A number of tools have been used to study ancient Greek and Roman inscriptions, including rubbings, squeezes, raking light imaging, and laser transmission (Chambers, 1992). We have shown that by using the ultra-intense X-ray beams produced by synchrotron X-ray sources, trace element concentrations in an inscription's surface layers at the glyph scale can easily be measured in seconds (Powers et al., 2005). By raster scanning the inscription relative to the X-ray beam, chemical analysis can be performed at an array of points across the inscribed surface. This data can be combined to create images showing the concentration variations of single elements. Some elements, including iron and lead, are present in larger concentrations in inscribed glyphs, and likely arose from tool wear during inscription and from subsequent painting. Lead can be detected in layers well below the original inscribed surface of the glyphs, opening the possibility of using XRF imaging to recover ancient text from worn and abraded inscriptions.

Here we describe an application of synchrotron-based XRF to examine an inscription of uncertain provenance. We perform XRF chemical analysis at single points and XRF imaging to correlate composition and the presence of inscribed letters, and show how this combination can provide useful insight into the possible origins of an inscription.

According to published records, NY.NY.NYU.L20 (U.S. Epigraphy no.) "appears to be an exact copy of the fragmentary consular *fasti* from Teanum Sidicinum in central Italy, of which the original is preserved at the American Academy in Rome" (Bodel and Tracy, 1997). The original tablet (General Meeting of the Archaeological Institute of America, 1905) is now on loan to the town of Teano in Italy (John Bodel, personal communication, July 29, 2006). No analysis beyond comparison of photographs has been performed on these tablets prior to our investigations.

The surface of the NYU tablet is slightly warped along the direction of the lines of text, such that its lettered side is on the outside of an arc. There is no obvious visual difference between the uninscribed surface of the tablet and the inscribed letters. There is no evidence of paint, pigment, dirt or debris within the inscribed letters. The only information we have about the Teano inscription is a photograph (Fig. 1a), which can be compared with a photograph of the NYU inscription (Fig. 1b). The tablets have the same shape, and both have a crack running from the bottom edge of the lower-right quadrant and slanting upward and to the left into the lower-left quadrant. The lettering on the two tablets appears identical, and any differences between the two photographs can be attributed to differences in lighting and perspective. However, the surfaces of the two tablets are noticeably different. The surface of the NYU tablet has many small, round raised formations (visible at the original resolution of the photograph, and one of which is visible inside the "D" in Fig. 3). It has a chip along its top edge, and is darkened in a large area in the lower right. The surface of the Teano tablet shows none of these features. It appears to be much smoother overall, and exhibits pitting on its right

* Corresponding author. Tel.: +1 607 255 6487; fax: +1 607 697 0400.
*E-mail address:* ret6@cornell.edu (R.E. Thorne).

0305-4403/$ – see front matter © 2008 Elsevier Ltd. All rights reserved.
doi:10.1016/j.jas.2008.09.030


**Fig. 1.** (a) Inscription from Teanum Sidicinum and (b) examined tablet from NYU. The similarity in shape of these fragmentary tablets and the imperfect rendering in (b) of the crack in the lower right of the Teanum Sidicinum inscription in (a) suggest that the NYU tablet is a modern copy.

side that is not present in the NYU tablet. These differences suggest that the tablets have had different histories, are made of different materials, and/or were prepared using different methods.

In antiquity it was not unusual for more than one copy of the same document to be inscribed on stone, but it is extremely unlikely that both copies were broken up in the passage of time to yield identically shaped and cracked fragments with identical text. The crack in the Teano tablet appears to be real, tapering to a hair-line, whereas the crack in the NYU tablet ends abruptly. This visual evidence suggests that the NYU tablet may be a relatively recent copy.

### 1.1. Method

The NYU tablet was examined at the Cornell High-Energy Synchrotron Source (CHESS). A 30 keV X-ray beam with a bandwidth of 0.5% was produced using a 15 Å W:$B_4C$ multilayer monochromator. The beam was trimmed using mechanical slits to a 0.50 × 0.50 mm spot size at the sample. The tablet was oriented with its surface perpendicular to the X-ray beam, and translated in the plane perpendicular to the beam using a motorized *xyz* stage with a resolution of better than 2 μm. Fluorescent and scattered X-ray photons were detected by an energy-dispersive X-ray detector placed at a 150° angle from the incident beam, and then processed using a multichannel analyzer to yield spectra of photon count versus photon energy. Hardware control and data collection were automated using SPEC (Certified Scientific Software). Data analysis was performed using MCASPEC (Huang, Argonne National Lab), MATLAB, and Octave. Some inscriptions used in comparisons with the NYU tablet were examined with a 17 keV beam produced using a 30 Å Mo:$B_4C$ multilayer having a 1.5% bandwidth.

To complement these XRF measurements, electron microprobe analysis of tablet chemical composition was performed using a JEOL JXA-9800R system with a solid-state electron dispersive spectrometer. Nearly microscopic grains were pulled off the tablet surface using carbon tape, and then placed in the microprobe chamber. The microprobe's electron beam is only micrometers in size, and can be used to examine individual mineral phases within a single grain. X-ray diffraction patterns were acquired using a general area detector diffraction system (GADDS) manufactured by Bruker AXS. Diffraction patterns were acquired using a 1.5 mm diameter X-ray beam from several points on the tablet surface, and compared with a powder diffraction database for several thousand minerals.

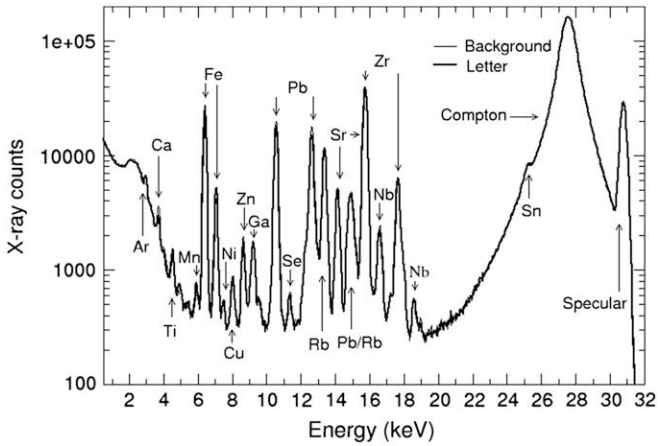


**Fig. 2.** X-ray fluorescence spectra acquired from two points on the NYU tablet, one on ("letter") and one beside ("background") the letter "D" in Fig. 3. Two of the observed peaks are produced by overlapping fluorescence from Pb and Rb and from Sr and Zr, respectively.

## 2. Results

### 2.1. X-ray fluorescence spectra

Our X-ray fluorescence spectra from ancient Roman inscriptions on marble typically show a strong Ca peak, weaker but pronounced Fe, Zn and Pb peaks, and detectable peaks of a number of other trace elements. These elements are present both within the inscribed letters and in the uninscribed regions of the stone's surface. Spatial variations in fluorescence intensity from these elements often correlate with the presence of inscribed lines that form the written text of the inscription (Powers et al., 2005).

XRF spectra from the NYU tablet such as those shown in Fig. 2 indicate the presence of Ca, Fe, Zn, Pb, Ti, Mn, Ni, Cu, Ga, Se, Rb, Sr and Nb, both within the inscribed letters and in the uninscribed background. Of these, Ca, Ti, Mn and Ni have peak heights roughly

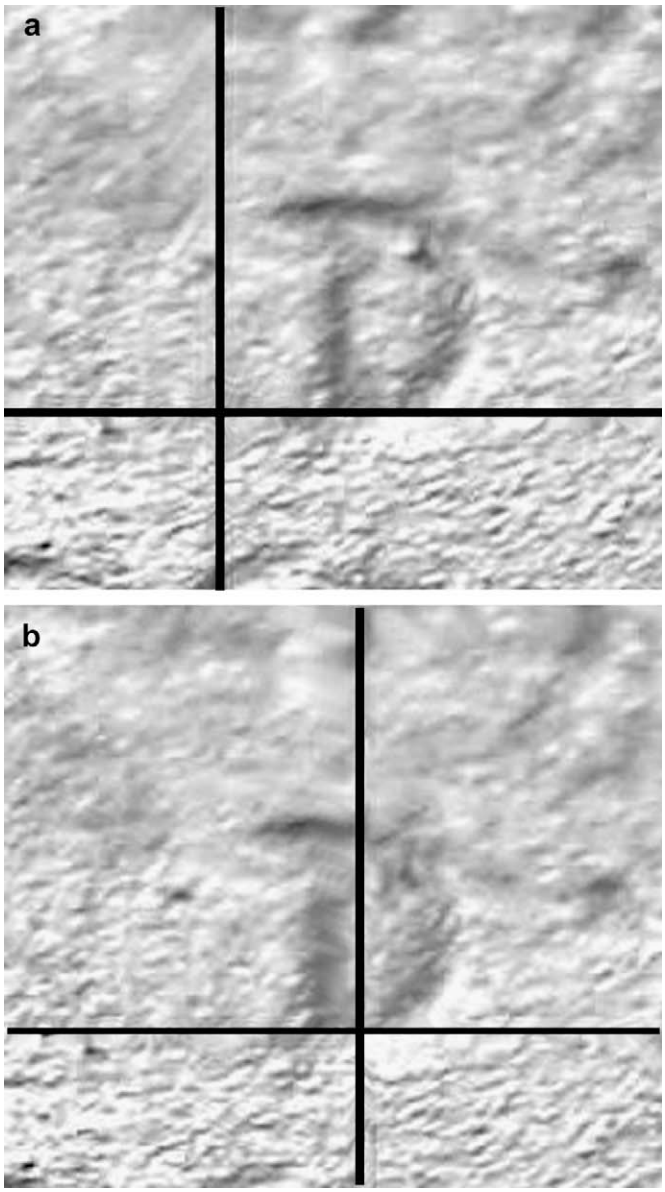


**Fig. 3.** Incident X-ray beam positions (intersection of the black lines) used in collecting (a) the "background" and (b) the "letter" fluorescence spectra in Fig. 2.

twice the detector noise level, and the other elements have peak heights at least five times the detector noise level. The spectra also show peaks for Ar, Zr and Sn, but reference spectra collected from a silicon block indicate that the Ar peak comes from air and that the Zr and Sn peaks come from components of the detector itself.

Spectra were acquired from a chipped area near the edge of the tablet's lettered face and from a point on the reverse face of the tablet. Comparisons of such spectra can provide information about surface treatments (e.g., painting or sealing) applied during or immediately after inscription and before chipping, and about the effects of weathering on surface chemical composition. For previously examined inscriptions, some chips appear similar to the rest of the surface while others expose fresh, unweathered marble. In the present case, the chip's surface coloration and grain structure are not noticeably different from the rest of the tablet's surface. This may indicate that the tablet has not weathered significantly since the chip was made, that the chip was made before significant weathering occurred, or that weathering beyond a certain point does not produce further qualitative changes in the surface. Fig. 4

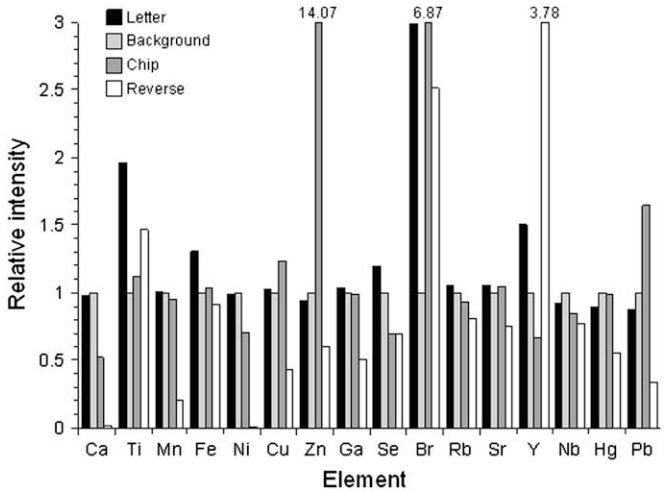


**Fig. 4.** X-ray fluorescence intensities from selected regions of the NYU tablet, normalized by the intensity from the off-letter background.

shows the fluorescence intensities for several elements obtained from different regions on the tablet surface, normalized by the intensities from the off-letter background of the lettered face. When compared with the background of the lettered surface, the spectrum from the chip has more Ga, Pb, Se, Cu and Zn, and the spectrum from the tablet's reverse face has less Cu, Zn, Ga, Se and Pb. Since the XRF data were acquired at a finite number of points, some of these differences may be due to inhomogeneous composition within each region rather than from region to region.

The amount of a trace element within the tablet's surface layers that are probed by the X-rays can be estimated from the measured fluorescence intensities using the photoelectric cross section, fluorescent yield and air scattering cross section for that element and for the other elements present in the matrix, taking into account absorption of incident and fluorescent X-rays by the other elements (MUCAL). We cannot determine the full composition of the tablet from our fluorescence data alone, since many light (e.g., C, N, O, Na, Mg, Al, Si, P and S) and heavy elements do not fluoresce in the 3–30 keV energy range in which our apparatus is sensitive. Due to the weak Ca fluorescence signal, we cannot reasonably assume that the tablet's primary constituent is calcium carbonate. Without knowledge of the tablet's primary constituents, we cannot accurately estimate trace element concentrations. We can, however, estimate the thickness of a solid surface layer of each trace element that would produce the observed fluorescence intensity. These estimates, given in Table 1, include absorption of the fluorescent X-rays by the fluorescing element and air, but

**Table 1**
Approximate thickness of a trace element layer necessary to produce the fluorescence of that element observed from the off-letter background of the NYU tablet.

| Element | Thickness (nm) |
|---|---|
| Ca | 400 |
| Fe | 37 |
| Rb | 17 |
| Ti | 10 |
| Pb | 9.8 |
| Zn | 1 |
| Ga | 1 |
| Mn | 0.9 |
| Cu | 0.5 |
| Nb | 0.3 |
| Ni | 0.2 |
| Se | 0.07 |
| Br | 0.02 |

neglect absorption by other elements. This approximation underestimates the layer thickness for Ca, whose X-rays are more readily absorbed by trace elements, and for elements that are uniformly distributed within the tablet and so are more strongly absorbed relative to those concentrated near its surface. These qualifications notwithstanding, the calculated Ca thickness of 400 nm is much smaller than the roughly 25 μm (comparable to the extinction length for Ca fluorescence) obtained from XRF measurements on clean marble.

### 2.2. Comparison to other XRF spectra

Several authentic inscriptions were examined along with the NYU tablet, using the same incident energy, detector and geometry. Examined inscriptions included *CIL* VI 12139, a titular Roman grave inscription; JHU 1059, an opisthographic graffito inscription from 2nd-century Rome; JHU 1156, a titular inscription; JHU 1166, a crudely made inscription; MD.Balt.JHU.L.134, a Christian epitaph from 4th to 5th century Rome; and JHU 96, a Roman libation bowl.

To compare XRF spectra between inscriptions, we normalize by the strength of the elastic X-ray scattering peak, as this is nearly proportional to the incident X-ray intensity. Following this normalization, the spectra in the low-energy region below Ca and the background between Ca and the Compton scattering tail agree, as expected. Tables 2 and 3 give the normalized fluorescence intensity from Ca and several trace elements obtained from single points on a letter (foreground) and on the surface surrounding the letters (background).

The most prominent difference between the NYU tablet's spectrum and those of the indicated inscriptions (as well as more than 10 other authentic Roman inscriptions examined) is its low Ca fluorescence. Considering the other six inscriptions examined here as a group, the intensities of the metallic trace elements – Fe, Zn, Cu and Pb – vary by roughly an order of magnitude between inscriptions and the intensities of Sr and Ca vary by about a factor of three. The NYU tablet has average levels of Zn and Cu, and somewhat more Fe and somewhat less Sr than any other inscription. The Pb intensity is seven times larger than in any other inscription and 15 times larger than the average. The Ca intensity is nine times smaller than in any other inscription and 13 times smaller than the average. The NYU tablet contains four other elements – Ga, Se, Rb and Nb – whose fluorescence is at least an order of magnitude stronger than in any other inscription. If we normalize the spectra not by the elastic scattering intensity but by the fluorescence intensity of Pb, one of the more common trace elements, then the fluorescence of these four elements from the NYU tablet is no longer anomalous. This could indicate that Pb, Ga, Se, Rb and Nb all derive from the same source (e.g., a particular mineral or surface contaminant) and that it is the concentration of this source within the NYU tablet that is anomalous.

**Table 2**
Calcium and common trace element fluorescence intensities, normalized by elastic scattering intensity, for the NYU tablet and six ancient Roman inscriptions.

| Inscription | Spectrum | Ca | Fe | Zn | Cu | Pb | Sr |
|---|---|---|---|---|---|---|---|
| NYU | Foreground | 0.10 | 0.87 | 0.060 | 0.028 | 0.583 | 0.167 |
| | Background | 0.12 | 0.70 | 0.063 | 0.028 | 0.650 | 0.167 |
| JHU 1059a | Foreground | 1.34 | 0.44 | 0.030 | 0.006 | 0.037 | 0.244 |
| | Background | 1.46 | 0.10 | 0.018 | 0.009 | 0.018 | 0.268 |
| JHU 1059b | Foreground | 1.35 | 0.18 | 0.018 | 0006 | 0.082 | 0.294 |
| | Background | 1.35 | 0.12 | 0.018 | 0.006 | 0.024 | 0.647 |
| JHU 1156 | Foreground | 0.93 | 0.58 | 0.075 | 0.013 | 0.055 | 0.275 |
| | Background | 1.50 | 0.13 | 0.025 | 0.005 | 0.023 | 0.250 |
| JHU 1166 | Foreground | 1.60 | 0.27 | 0.045 | 0.009 | 0.024 | 0.700 |
| | Background | 1.60 | 0.11 | 0.025 | 0.007 | 0.020 | 0.700 |
| JHU 96 | Background | 0.87 | 0.38 | 0.077 | 0.014 | 0.058 | 0.308 |
| JHU.L.134 | Foreground | 1.09 | 0.82 | 0.100 | 0.073 | 0.073 | 0.436 |
| | Background | 1.09 | 0.36 | 0.073 | 0.018 | 0.064 | 0.436 |
| CIL VI 12139 | Foreground | 2.59 | 0.10 | 0.250 | 0.009 | 0.049 | 0.328 |
| | Background | 2.76 | 0.04 | 0.172 | 0.008 | 0.026 | 0.293 |

**Table 3**
Less common trace element fluorescence intensities, normalized by elastic scattering intensity, for the NYU tablet and six ancient Roman inscriptions.

| Inscription | Spectrum | Ga | Se | Rb | Nb |
|---|---|---|---|---|---|
| NYU | Foreground | 0.050 | 0.010 | 0.350 | 0.060 |
| | Background | 0.050 | 0.010 | 0.350 | 0.070 |
| JHU 1059a | Foreground | 0.005 | 0 | 0.015 | 0.006 |
| | Background | 0.004 | 0 | 0 | 0 |
| JHU 1059b | Foreground | 0.003 | 0 | 0 | 0 |
| | Background | 0.003 | 0 | 0 | 0 |
| JHU 1156 | Foreground | 0.004 | 0 | 0.003 | 0 |
| | Background | 0.004 | 0 | 0.010 | 0 |
| JHU 1166 | Foreground | 0.003 | 0 | 0.005 | 0 |
| | Background | 0.003 | 0 | 0 | 0 |
| JHU 96 | Background | 0.010 | 0.010 | 0.010 | 00 |
| JHU.L.134 | Foreground | 0.004 | 0 | 0.018 | 0 |
| | Background | 0.004 | 0 | 0.011 | 0 |
| CIL VI 12139 | Foreground | 0.003 | 0.001 | 0 | 0 |
| | Background | 0.003 | 0.001 | 0 | 0 |

### 2.3. Calcium fluorescence masking by trace elements

The NYU tablet's weak XRF calcium signal could result if the excited Ca fluorescence is absorbed by trace elements near the surface of the tablet. Clear evidence for such masking is seen within the letters of other inscriptions, where trace element fluorescence is higher and Ca fluorescence is modestly lower. By comparing the NYU tablet's calcium fluorescence with that of clean marble (whose trace element concentrations are too small to produce significant masking), we can estimate the amount of masking elements required to produce the small observed Ca intensity. We focus on masking by Fe and Pb, the most abundant trace elements.

We assume a model in which Fe and Pb are present in a thin layer on top of a slab of $CaCO_3$ (as a homogeneous mixture of either the pure metals or of iron oxide ($Fe_2O_3$) and lead oxide ($Pb_3O_4$)) in a concentration ratio given by their measured XRF peak intensities. With this model, matching the observed Ca fluorescence intensity requires absorption by 12 μm of metal or 22 μm of oxides, but such thick layers should be evident from a visual inspection of the surface, and would produce about 150 times more Fe and Pb fluorescence than is observed. The observed Fe and Pb intensities would require fluorescent emission from 37 nm of Fe and 10 nm of Pb, far too little to appreciably mask Ca fluorescence. Assuming that the tablet surface consists of a homogeneous mixture of Ca, Fe and Pb does not appreciably change these results. Another possibility is that the Ca fluorescence is being masked by a material composed of elements with lower atomic numbers than Ca (20), which could not be detected in our XRF experiment. The required thicknesses of O, Al, Mg or Si-rich mineral layers are, for typical mineral densities, roughly 50–100 μm. This is comparable to the X-ray extinction length, so that these minerals, not calcite would then likely be the dominant constituents.

These results suggest that the principal constituent of the NYU tablet is not calcite ($CaCO_3$) or any other calcium-based mineral. Instead, it may be comprised of Si, Mg, and/or Al-based minerals whose X-ray fluorescence lines have energies too low to be detected in our current setup.

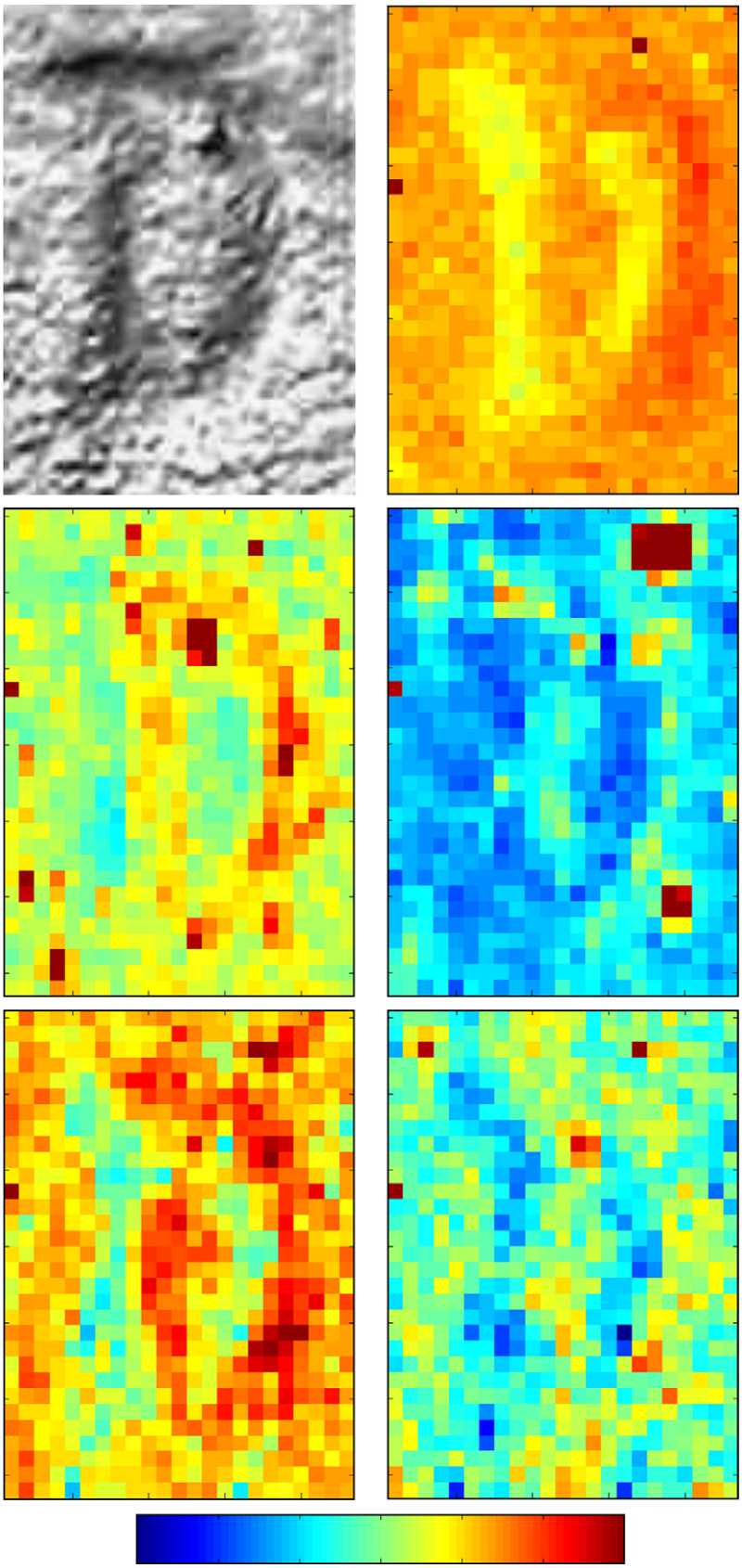

**Fig. 5.** Images of a letter "D" on the NYU inscription. Clockwise from top left: a photographic image, a coherent X-ray scattering image, and single-element X-ray fluorescence images for Fe, Pb, Rb and Sr, respectively. X-ray intensity increases from blue to red. The incident X-ray beam and detector lie in the horizontal plane. The observed spatial variations in fluorescence intensity are consistent with shadowing due to surface topography. No variation in trace element concentration between letter and background, typically seen in ancient Roman inscriptions, is evident.

### 2.4. X-ray fluorescence imaging

Fig. 5 shows how XRF imaging was used to examine correlations between the distribution of trace elements and the presence of letters. Measurements at many points are required to create a two-dimensional image, and so the data acquisition time per point is shorter than in the preceding measurements. Because of the larger statistical uncertainties, imaging was only possible using Fe, Pb, Sr, Rb, Zn and Ga. Neither the Zn nor Ga XRF intensities showed any correlation with the presence or absence of letters. Other elements only showed intensity variations consistent with "shadowing" due to surface topography, not with actual variations in elemental concentration between letter and background. Because the detector is roughly 30° from the surface normal, the measured fluorescence intensity is decreased on the detector side and increased on the opposite side of an inscribed line that runs perpendicular to plane of the incident beam and detector.

The absence of any appreciable on-letter to off-letter concentration variations within the NYU tablet is confirmed by a principal components analysis (PCA) of the XRF spectra using singular value decomposition (Powers et al., in preparation). The only component correlated to the inscribed letters is 0.47% as significant as the most-significant principal component.

This lack of correlation contrasts with results for authentic Roman inscriptions that are not heavily worn (e.g., JHU 1166, shown in Fig. 6). These typically show much larger concentrations of trace elements in the inscribed letters, presumably due to tool wear and remnants of the original paint layer. The PCA component most strongly correlated to the inscribed letters ranges from 1.5% to 10.7% as significant as the most-significant principal component.

### 2.5. Comparison with electron microprobe and X-ray diffraction analysis

As a check on our XRF results, we performed electron microprobe analysis on grains that were removed from the surface of the NYU tablet using carbon tape. We also measured X-ray diffraction patterns from several points on the tablet's surface. Fig. 7 (a–c) shows representative electron microprobe spectra obtained from three different grains. These and similar spectra suggest the presence of several minerals including quartz, silicates, salts and barium sulfate. None of the grains appears to contain calcite. Most interestingly, some grains appear to be calcium sulfate, the binder in plaster of Paris. Fig. 7(d) shows a typical X-ray diffraction pattern from the NYU tablet's surface. These patterns appear to be a superposition of patterns from several minerals. The solid vertical lines indicate the expected peak positions for pure calcite. The poor match between these lines and the measured peak positions confirms that calcite is not a major constituent of the tablet.

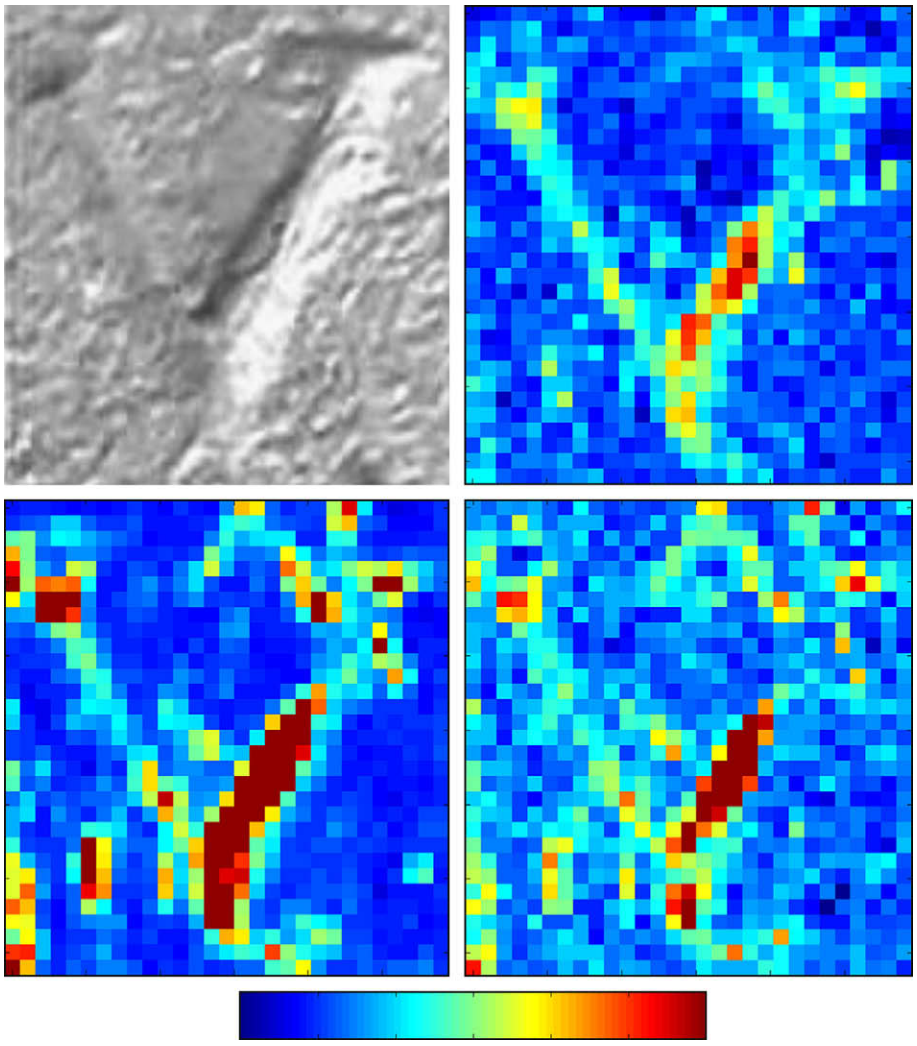

**Fig. 6.** Single-element XRF images of a letter "V" on JHU 1166. Intensity increases from blue to red. Clockwise from top left: a photographic image, and single-element X-ray fluorescence images for Zn, Fe and Pb, respectively. These images show spatial variations in trace element concentrations typical for ancient Roman inscriptions.

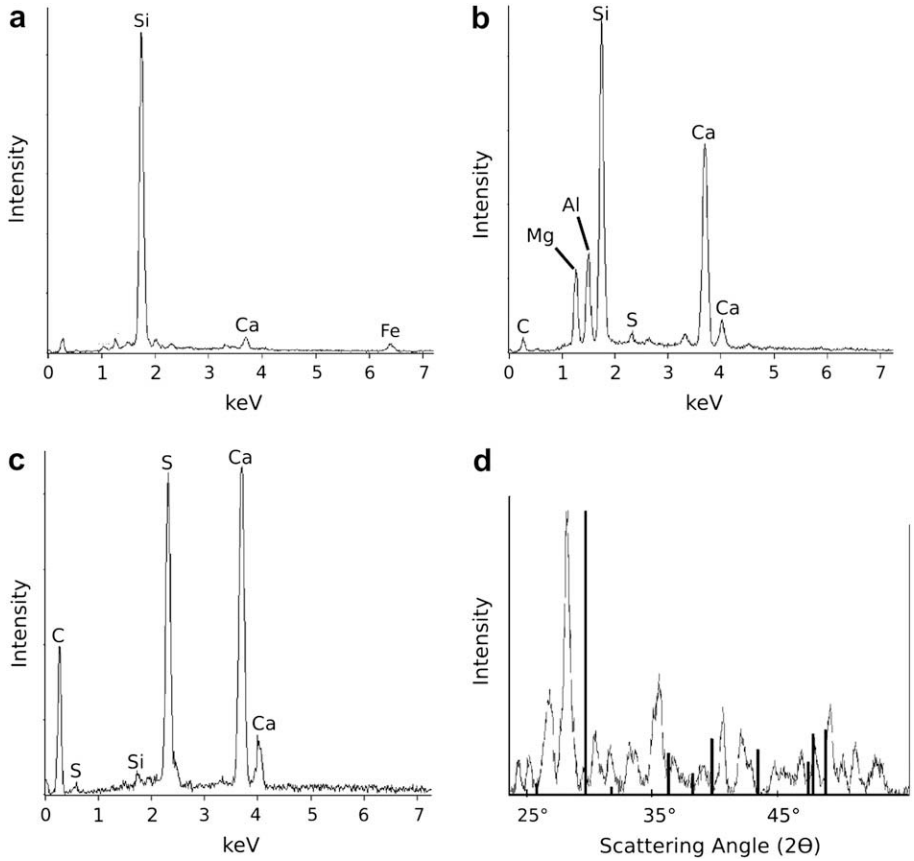


**Fig. 7.** (a)–(c) Representative electron microprobe spectra from individual grains removed from the surface of the NYU tablet. The spectra suggest that the grain is (a) primarily silica, (b) possibly a silicate containing Al, Ca and Mg, and (c) possibly calcium sulfate, the binder in plaster of Paris. (d) X-ray diffraction intensity versus scattering angle from a typical point on the NYU tablet. The vertical lines indicate the relative intensities and angles of the diffraction peaks from pure calcite.

## 3. Discussion

Based upon the XRF measurements, the NYU tablet's most striking differences from the authentic Roman inscriptions we have examined are its very low Ca fluorescence and its high trace element fluorescence, especially from the less common trace elements Ga, Se, Nb and Rb. The Ca fluorescence could be masked by other elements present in the surface of the tablet, but our analysis shows that such masking cannot be due to any of the elements that we could detect in our experiment. The U.S. Epigraphy database lists 913 stone inscriptions, of which 885 are marble, 18 limestone, 5 travertine (another form of $CaCO_3$). Only five are on other types of stone (jasper, basalt, granite, and unknown). The NYU tablet's low Ca fluorescence thus makes it highly suspect.

The NYU tablet also shows no appreciable variation in XRF-determined trace element concentrations between the letters and the tablet background. This has not been observed for any authentic Roman inscription that shows so little evidence of weathering or wear. This could arise if different tools or a different method were used to produce the letters on the NYU tablet and if the letters were not painted with metal oxide containing pigments. Alternatively, the surface may have been exposed to an unusual kind of weathering or to a chemical treatment that removed trace element residues from carving and painting. However, the surface and its grain texture show no evidence of harsh treatment or any position-to-position variations that such a treatment might be expected to produce. A third possibility is that the original inscribed surface has been coated or encased in a material that is thick enough and comprised of sufficiently strongly absorbing elements to mask fluorescence from the original inscribed surface. Again, visual inspection provides no evidence for such treatment, and surface coatings common in Roman times were primarily organic and thus would not produce adequate absorption.

## 4. Conclusions

Combining these XRF results with the results of electron microprobe and X-ray diffraction measurements, we conclude that the NYU tablet is not an authentic Roman inscription. It appears to be a composite of many minerals that may have been crushed and mixed with a small amount of plaster of Paris and perhaps other binders. This composite mixture was not inscribed or painted, but was likely cast in a mold of the original inscription. The "crack" visible in Fig. 1(b) was likely excavated after casting.

Synchrotron-based XRF analysis has several attractive features compared with other analysis methods. It is completely non-destructive, and can be used on tablets of area 1 $m^2$ or larger. Synchrotron X-ray beams are extremely intense (up to $10^7$ times more intense than those of laboratory or portable X-ray sources), allowing very rapid XRF measurements of major and trace element constituents with very high sensitivity. XRF imaging of the spatial distribution of elements within the surface can be performed in minutes to hours, and these images can provide information about tools, pigments and weathering that are much more difficult to obtain via electron-based methods. X-ray beam size can be reduced with focusing optics from the 0.5 mm used here to 20 μm or less, smaller than the grain size of marble and limestone. With minor modifications to the experimental setup, X-ray diffraction data can be collected concurrently with XRF data, allowing identification of minerals. Using the procedures we have outlined here,

synchrotron-based XRF analysis can thus be a powerful complement to existing tools for evaluating inscription provenance.

## Acknowledgements

The authors would like to acknowledge the support of the Samuel H. Kress Foundation and the contributions of Eunice Maguire and Johns Hopkins University and of New York University. X-ray diffraction and electron microprobe measurements were performed with the assistance of John Hunt and Maura Weathers of the Cornell Center for Materials Research, which is supported by the National Science Foundation under award DMR-0520404. The large *xyz* stage used was provided by Arthur Woll. This work is based upon research conducted at the Cornell High-Energy Synchrotron Source (CHESS) which is supported by the National Science Foundation under award DMR-0225180.

## References

Bodel, John, Tracy, Stephen, 1997. Greek and Latin Inscriptions in the U.S.A.: a Checklist, 202–205. American Academy in Rome.

Chambers, M., 1992. Photographic enhancement and a Greek inscription. The Classical Journal 88, 25–31.

General Meeting of the Archaeological Institute of America, December 28–30, 1904. American Journal of Archaeology 9 (1), Jan–Mar, 1905, 67–68.

MUCAL. Center for Synchrotron Radiation Research and Instrumentation, Illinois Institute of Technology. Available from: http://www.csrri.iit.edu/periodic-table.html.

Powers, J., Dimitrova, N., Huang, R., Smilgies, D.-M., Bilderback, D.H., Clinton, K., Thorne, R.E., 2005. X-ray fluorescence recovers writing from ancient inscriptions. Zeitschrift für Papyrologie und Epigraphik 152, 221–227.

# Bibliography


[1] A. Adriaens. Elemental composition and microstructure of early bronze age and medieval tin slags. *Microchim. Acta*, 124:89–98, 1996.

[2] J.C. Bezdek, R. Ehrlich, and W. Full. FCM: The fuzzy $c$-means clustering algorithm. *Computers and Geosciences*, 10(2):191–203, 1984.

[3] L. Bonizzoni, A. Maloni, and M. Milazzo. Evaluation of effects of irregular shape on quantitative XRF analysis of metal objects. *X-Ray Spectrometry*, 35:390–399, 2006.

[4] D. Brems, M. Ganio, K. Latruwe, L. Balcaen, M. Carremans, D. Gimeno, A. Silvestri, F. Vanhaeke, P. Muches, and P. Degryse. Isotopes on the beach, part 1: strontium isotope ratios as a provenance indicator for lime raw materials used in Roman glassmaking. *Archaeometry*, 55(2):214–234, 2012.

[5] R. H. Brill. The scientific investigation of ancient glasses. In *Proc. Eighth Internat. Congress on Glass*. Society of Glass Technology, Sheffield, 1969.

[6] R. H. Brill. *Chemical Analysis of Early Glasses*, volume 1. Corning Museum of Glass, Corning, NY, 1999.

[7] R. H. Brill. *Chemical Analysis of Early Glasses*, volume 2. Corning Museum of Glass, Corning, NY, 1999.

[8] A. Brunetti, M. Sanchez del Rio, B. Golosio, A. Simionovici, and A. Somogyi. A library for X-ray–matter interaction cross sections for X-ray fluorescence applications. *Spectrochim. Acta B: Atom. Spectros.*, 59(10):1725–1731, 2004.

[9] C.J.C. Burges. A tutorial on support vector machines for pattern recognition. *Data Mining and Knowledge Discovery*, 2:121–167, 1998.

[10] T. Calligaro, J.-C. Dran, J. Salomon, and Ph. Walter. Review of accelerator gadgets for art and archaeology. *Nuc. Instrum. Meth. in Phys. Res. B.*, 226:29–37, 2004.

[11] R. L. Cannon, J. V. Dave, and J.C. Bezdek. Efficient implementation of the fuzzy $c$-means clustering algorithms. *IEEE Trans. Pattern Anal. and Machine Intelligence*, PAMI-8(2):248–255, 1986.

[12] D. A. Cremers, F. Y. Yueh, J. P. Singh, and H. Zhang. *LaserInduced Breakdown Spectroscopy, Elemental Analysis*. John Wiley & Sons, Ltd., 2006.

[13] W. Devos, M. Senn-Luder, C. Moor, and C. Salter. Laser ablation inductively coupled plasma mass spectrometry (LA-ICP-MS) for spatially resolved trace analysis of early-medieval archaeological iron finds. *Fresenius' J. Anal. Chem.*, 366(8):873–880, 2000.

[14] S. Duwe and H. Neff. Glaze and slip pigment analysis of Pueblo IV period ceramics from east-central Arizona using time of flight-laser ablation-inductively coupled plasma-mass spectrometry (tof-la-icp-ms). *J. Archeol. Sci.*, 34(403-414), 2007.

[15] T. G. Dzubay, B. V. Jarrett, and J. M. Jaklevic. Background reduction in x-ray fluorescence spectra using polarization. *Nuc. Instrum. Meth.*, 115:297–299, 1974.

[16] R. Falcone, G. Sommariva, and M. Verita. WDXRF, EPMA, and SEM/EDX quantitative chemical analyses of small glass samples. *Microchim. Acta*, 155:137–140, 2006.

[17] A. Giakoumaki, K. Melessanaki, and D. Anglos. Laser-induced breakdown spectroscopy (LIBS) in archaeological science–applications and prospects. *Anal. Bioanal. Chem.*, 387:749–760, 2007.

[18] B. Giussani, D. Monticelli, and L. Rampazzi. Role of laser ablation-inductively coupled plasma-mass spectrometry in cultural heritage research: A review. *Anal. Chim. Acta*, 635:6–21, 2009.

[19] M.D. Glasscock. Overview of neutron activation analysis. `http://archaeometry.missouri.edu/naa_overview.html`, 2013.

[20] H. Hotelling. Analysis of a complex of statistical variables into principal components. *J. Educ. Psych.*, 24:417–441, 1933.

[21] J. MacQueen. Some methods for classification and analysis of multivariate observations. In *Proc. Fifth Berkeley Symp. on Math. Statist. and Prob.*, volume 1. Univ. of Calif. Press, Berkeley, 1967.

[22] N. R. Pal and J. C. Bezdek. On cluster validity for the fuzzy $c$-means model. *IEEE Trans. Fuzzy Syst.*, 3(3):370–379, 1995.

[23] J. Powers, N. Dimitrova, R. Huang, D.-M. Smilgies, D. H. Bilderback, and R. E. Thorne. X-ray fluorescence recovers writing from ancient inscriptions. *Z. Papyrologie Epigraphik*, 152:221–227, 2005.

[24] J. Powers, D-M. Smilgies, E. C. Geil, K. Clinton, M. Peachin, and R. E. Thorne. X-ray fluorescence imaging analysis of inscription provenance. *J. Archaeol. Sci.*, 36:343–350, 2009.

[25] I. Reiche, A. Berger, A. Duval, W. Görner, H. Guicharnaud, H. Merchel, M. Radke, J. Riederer, and H. Riesemeier. Non-destructive investigation of Dürer's silver point drawings by PIXE and SR-XRF. *Non-Destructive Testing and Micro-Analysis for the Diagnostic and Conservation of the Cultural and Environmental Heritage, Proc. Art*, 2002.

[26] M. Resano and F. García-Ruiz, E.and Vanhaecke. Laser ablation-inductively coupled plasma mass spectrometry in archaeometric research. *Mass spectrom. rev.*, 29(1):55–78, 2010.

[27] M Resano, MP Marzo, R Alloza, C. Saénz, L. Vanhaecke, F.and Yang, S. Willie, and R.E. Sturgeon. Laser ablation single-collector inductively coupled plasma mass spectrometry for lead isotopic analysis to investigate evolution of the *Bilbilis* mint. *Anal. Chim. Acta*, 677(1):55–63, 2010.

[28] M Resano, P Marzo, J. Pérez-Arantegui, M. Aramendia, C. Cloquet, and F. Vanhaecke. Laser ablation-inductively coupled plasma-dynamic reaction cell-mass spectrometry for the determination of lead isotope ratios in ancient glazed ceramics for discriminating purposes. *J. Anal. Atom. Spectrom.*, 23(9):1182–1191, 2008.

[29] C. G. Ryan, D. P. Siddons, R. Kirkham, P. A. Dunn, A. Kuczewski, G. Moorhead, G. De Geronimo, D. J. Paterson, M. D. de Jonge, R. M. Hough, M. J. Lintern, D. L. Howard, P. Kappen, and J. Cleverley. The new Maia detector system: Methods for high definition trace element imaging of natural material. *AIP Conference Proceedings*, 1221(1), 2010.

[30] T. Schoonjans, A. Brunetti, B. Golosio, M. Sanchez del Rio, V.A. Solé, C. Ferrero, and V. Laszlo. The xraylib library for X-ray-matter interactions. recent developments. *Spectrochim. Acta B: Atom. Spectros.*, 66(11):776–784, 2011.

[31] V. Scot, J. E. Fermandez, L. Vincze, and K. Janssens. 3D extention of the Monte Carlo code MCSHAPE for photon-matter interactions in hterogeneous media. *Nuc. Instrum. Meth. in Phys. Res. B.*, 263:204–208, 2007.

[32] A. Shortland and K. Eremin. The analysis of second millenium glass from Egypt and Mesopotamia, part 1: new WDS analyses. *Archaeometry*, 4:581–603, 2006.

[33] A. Shortland, N. Rogers, and K. Eremin. Trace element discriminants between Egyptian and Mesopotamian Late Bronze Age glasses. *J. Archaeol. Sci.*, 34:781–789, 2007.

[34] A. J. Shortland. The use and origin of antimonate colorants in early Egyptian glass. *Archaeometry*, 4:517–530, 2002.

[35] D-M. Smilgies, J. A. Powers, D. H. Bilderback, and R. E. Thorne. Dual-detector X-ray fluorescence imaging of ancient artifacts with surface relief. *J. Synchrotron Rad.*, 19:547–550, 2012.

[36] V.A. Solé, E. Papillon, M. Cotte, Ph. Walter, and J. Susini. A multiplatform code for the analysis of energy-dispersive X-ray fluorescence spectra. *Spectrochim. Acta Part B: Atom. Spect.*, 62(1):63–68, 2007.

[37] G. Spotto and G. Grasso. Spatially resolved mass spectrometry in the study of art and archaeological objects. *Trends in Anal. Chem.*, 30:856–863, 2011.

[38] J.A.K. Suykens and J. Vadewalle. Least squares support vector machine classifiers. *Neural processing lett.*, 9(3):293–300, 1999.

[39] T. Trojek. Reconstruction of the relief of an investigated object with scanning x-ray fluorescence microanalysis and monte carlo simulations of surface effects. *Appl. Radiation and Isotopes*, 70:1206–1209, 2012.

[40] T. Trojek, T. Čecàk, and L. Musílek. Monte Carlo simulations of disturbing effects in quantitative in-situ x-ray fluorescence analysis and microanalysis. *Nuc. Instrum. Meth. in Phys. Res. A.*, 619:266–269, 2010.

[41] T. Trojek and D. Wegrzynek. X-ray fluorescence $k_\alpha/k_\beta$ ratios for a layered specimen: Comparison of measurements and Monte Carlo code calculations with the MCNPX code. *Nuc. Instrum. Meth. in Phys. Res. A.*, 619:311–315, 2010.

[42] H. P. Urbach and P. K. de Bokx. Grazing emission x-ray fluorescence from multilayers. *Phys. Rev. B*, 63:085408, 2001.

[43] V. N. Vapnik. *The Nature of Statistical Learning Theory.* Springer-Verlag, New York, 1995.

[44] P. Williams. Secondary ion mass spectrometry. *Ann. Rev. Mater. Sci.*, 15:517–548, 1985.

[45] X.L. Xie and G. Beni. A validity measure for fuzzy clustering. *IEEE Trans. Pattern Anal. and Machine Intelligence*, 13(8):841–847, 1991.

[46] K. Yamamoto, D.A. Cremers, M.J. Ferries, and L.E. Foster. Detection of metals in the environment using a portable laser-induced breakdown spectroscopy instrument. *Appl. Spectrosc.*, 50:222–233, 1996.